

Manufacturing and irradiation of thin transition metal nitride films

Dissertation  
Zur Erlangung des Doktorgrades  
der Mathematisch-Naturwissenschaftlichen Fakultäten  
der Georg-August-Universität zu Göttingen

vorgelegt von  
Leena Rissanen  
aus Nivala, Finnland

Göttingen 1999

D 7

Referent: Prof. Dr. K.P. Lieb  
Korreferent: Prof. Dr. K. Winzer  
Tag der mündlichen Prüfung: 1. November 1999

<b>1</b>	<b>INTRODUCTION: PRODUCTION OF TRANSITION METAL NITRIDES AND ION BEAM IRRADIATION OF NITRIDE/SEMICONDUCTOR BILAYERS .....</b>	<b>2</b>
<b>2</b>	<b>EXPERIMENTAL METHODS.....</b>	<b>4</b>
2.1	SAMPLE PREPARATION .....	4
2.2	ANALYZING METHODS .....	6
2.2.1	<i>Rutherford Backscattering Spectrometry.....</i>	6
2.2.2	<i>Time Of Light Elastic Recoil Detection and Analysis.....</i>	10
2.2.3	<i>Resonant Nuclear Reaction Analysis.....</i>	13
2.2.4	<i>Mössbauer Spectroscopy.....</i>	17
2.2.5	<i>X-Ray Diffraction .....</i>	24
2.2.6	<i>Transmission Electron Microscopy.....</i>	26
2.2.7	<i>Atomic Force Microscopy.....</i>	27
<b>3</b>	<b>PRODUCTION OF MAGNETRON SPUTTERED FeN AND Ni<sub>3</sub>N THIN FILMS.....</b>	<b>30</b>
3.1	Fe-N AND Ni-N PHASE DIAGRAMS .....	30
3.2	GAS MIXTURE AND PRESSURE .....	32
3.3	SUBSTRATE TEMPERATURE .....	35
3.4	SUBSTRATE BIAS VOLTAGE .....	41
3.5	RF POWER.....	44
3.6	STABILITY AGAINST ANNEALING.....	46
3.7	DISCUSSION, SUMMARY AND OUTLOOK OF CHARACTERIZATION .....	53
<b>4</b>	<b>ION-BEAM IRRADIATION OF Ni<sub>3</sub>N/Si BILAYERS.....</b>	<b>55</b>
4.1	IRRADIATION INDUCED SURFACE EFFECTS .....	55
4.2	ION BEAM MIXING .....	56
4.2.1	<i>Mixing due to ballistic effect.....</i>	57
4.2.2	<i>Mixing due to thermal spikes and thermochemical properties .....</i>	58
4.3	LOW ENERGY IRRADIATION EFFECTS.....	60
4.4	ION-BEAM MIXING AND PHASE FORMATION .....	66
4.4.1	<i>450 keV irradiations at 80 K.....</i>	66
4.4.2	<i>700 keV irradiations at 80 K; the effect of irradiation energy.....</i>	70
4.4.3	<i>450 keV irradiations at room temperature; the effect of irradiation temperature.....</i>	74
4.5	DISCUSSION AND INTERPRETATIONS .....	76
4.6	SUMMARY.....	80
<b>5</b>	<b>REFERENCES.....</b>	<b>82</b>

# 1 Introduction: production of transition metal nitrides and ion beam irradiation of nitride/semiconductor bilayers

Metal nitrides, especially those of transition metals, have received increasing attention in recent years because of their outstanding mechanical, optical, electrical and magnetic properties [1-4]. These materials can be used for corrosion resistant and optical coatings, electrical contacts and diffusion barriers. Thin nitride layers can be produced by various techniques, by chemical vapor deposition, by reactive sputtering, by plasma assisted deposition, by implanting nitrogen ions, by laser assisted deposition, etc. Magnetron sputtering is a technology that has been extensively utilized by both industrial and scientific research groups in producing thin elemental or compound films [5,6]. The popularity of sputtering comes from the versatility of the technique, and from the flexibility for alternation and customization. As an extreme example we mention the large area ( $> 50 \text{ m}^2$ ) deposition of a mirror surface for the world's largest telescope [7]. Control and understanding of the deposition method is a critical factor in determining the properties of the nitride film. Reactive sputtering is a nonlinear process, which usually exhibits effects causing instabilities. It is therefore not straightforward to predict the behavior of the system such as the deposition rate, uniformity, composition and texture effects.

Magnetron sputtering is an excellent method for producing transition metal nitrides over a wide range of concentrations and has enabled the extension of the Fe-N phase diagram to the nitrogen rich region. The discovery of new FeN phases,  $\gamma''$ - and  $\gamma''$ -FeN, has inspired several research groups to investigate their structure and properties in this part of the phase diagram [6,8-11]. But the production of pure phases is not easy. Impurity elements and defect structures disturb the results and therefore the analyzing has to be carried out carefully. In many cases only a combination of various analyzing methods accomplishes the correct outcome. The aim of the first part of this study was to produce as pure single-phase FeN films as possible by reactive magnetron sputtering. The influence of all the deposition parameters on the thin film properties was investigated in great detail. The stability of FeN phase was observed as function of the deposition temperature as well as by annealing in different atmospheres.

The second part of the present work was the effects induced by the irradiation of  $\text{Ni}_3\text{N}/\text{Si}$  bilayers with heavy Xe ions. The bonding properties of nitrides to metals and semiconductors, for instance via ion irradiation, are of great importance. A large number of studies on ion-beam induced effects in metal/metal, metal/ceramic and metal/semiconductor bilayers [12-14] have been carried out in order to produce stable and metastable alloys, improve the adhesion of the film, understand the transport mechanisms and phase formation processes, and optimize the process mechanisms. In bilayer experiments the presence of the chemical potential gradient at the interface has an influence on the mixing process. Depending on the bilayer materials, the amount of mixing can be enhanced or suppressed relative to a purely ballistic mixing. The effect of the thermochemical properties has been known to exist for heavy bilayer systems ( $Z_{\text{ave}} > 20$ ), where the atomic transport process is

dominated by diffusion within thermal spikes. In the case of thermochemically mixing metals the chemical potential gradient at the interface generally enhances the mixing process. In some systems, e.g. in Ag/Fe bilayers, the amount of mixing was suppressed [15]. In bilayers with  $Z_{\text{ave}} < 20$  the initiation of thermal spikes should not be possible, and the mixing process should have a ballistic nature. The effect of chemical driving forces on such a system has previously been assumed, but not yet demonstrated [16]. Ni<sub>3</sub>N/Si system ( $Z_{\text{ave}} = 18.4$ ) is a possible candidate to investigate the validity of this assumption. Milosavljevic et al. [17] irradiated Ni<sub>3</sub>N/Al bilayers with Xe ions at 80 K and found that the athermal mixing rate was higher than the one predicted by the ballistic model, but lower than the thermal spike model would give. However, neither the role of nitrogen nor the ion-induced surface roughening or the formation of phases at the bilayer interface has been investigated. In the present work, along with the atomic transport processes at the interface also the compositional and structural changes in the near-surface region after low energy irradiation were studied combining ion beam analytical methods with surface microscopy and X-Ray Diffraction analysis.

## 2 Experimental methods

The following chapters describe the experimental details of sample preparation, sample treatment and analyzing methods via ion beam techniques, Mössbauer Spectroscopy, X-Ray Diffraction, Transmission Electron and Atomic Force Microscopy.

### 2.1 Sample preparation

In the present work the thin nitride films were produced by reactive magnetron sputtering. In general the working principle of a magnetron can be described as follows. The magnetron sputtering transfers material from a target onto a substrate. This is accomplished by generating a plasma in the low pressure chamber in front of the target. Applying a negative voltage of several 100 V on the target, as an inert gas (such as argon) is introduced into the vacuum, generates the plasma. This leads to a plasma discharge where positively charged argon ions are accelerated towards the target. The target material is eroded and, in turn, deposited on the substrate. The magnetron chamber is schematically presented in Figure 2.1. In reactive sputtering systems, oxygen, nitrogen or other gases are inserted to the chamber along with the inert gas in order to form compound films. Working with target distances of several centimeters, a strong magnet field creates a dense plasma (magnetron) to increase the process efficiency. The design of the plasma system, the partial pressures of the gases, the substrate temperature, the RF power, the possible bias voltage added between the substrate holder and the chamber, determine the sputter rate as well as the uniformity, stoichiometry, crystalline structure and other properties of the deposited film. The reactive sputtering is a complex process and the preparing of a pure phase structure requires a good knowledge of the effects of these parameters.

Working with ferromagnetic sputter targets (for example iron and nickel) causes particular problems. The target as a cathode develops a magnetic short circuit, which decreases or even removes the magnetic field in front of the target [9]. As a result the plasma is delocalized. The sputtering chamber walls get heated and impurities condensed on them vaporize into the plasma.

In this work a permanent-magnet planar-type RF magnetron from Iontech Ltd was used for sputtering thin iron and nickel nitride films. The system employed a 500 W RF-generator. The base pressure of the vacuum chamber was lower than  $10^{-4}$  Pa, the working pressure about 0.5 Pa. High-purity iron (99.999 % Fe) and nickel (99.999 % Ni) discs with diameter of 76 mm and thickness of 6 mm were used as sputtering targets. The distance between the target and the substrates was 8 cm. The substrate temperature was controlled and varied between 283 and 823 K. At room temperature depositions the substrate holder was water-cooled. All substrates were cleaned with acetone before mounting on the holder. In the case of nickel nitride deposition the substrates were etched in fluoric acid followed by rinsing in deionized water. The pure argon (99.998 % Ar) and nitrogen (99.9999 % N<sub>2</sub>) gas flows, controlled by two independent mass-flow controllers, could be varied between 0 and 30 sccm (standard cubic centimeter), within an accuracy of 0.3 sccm.

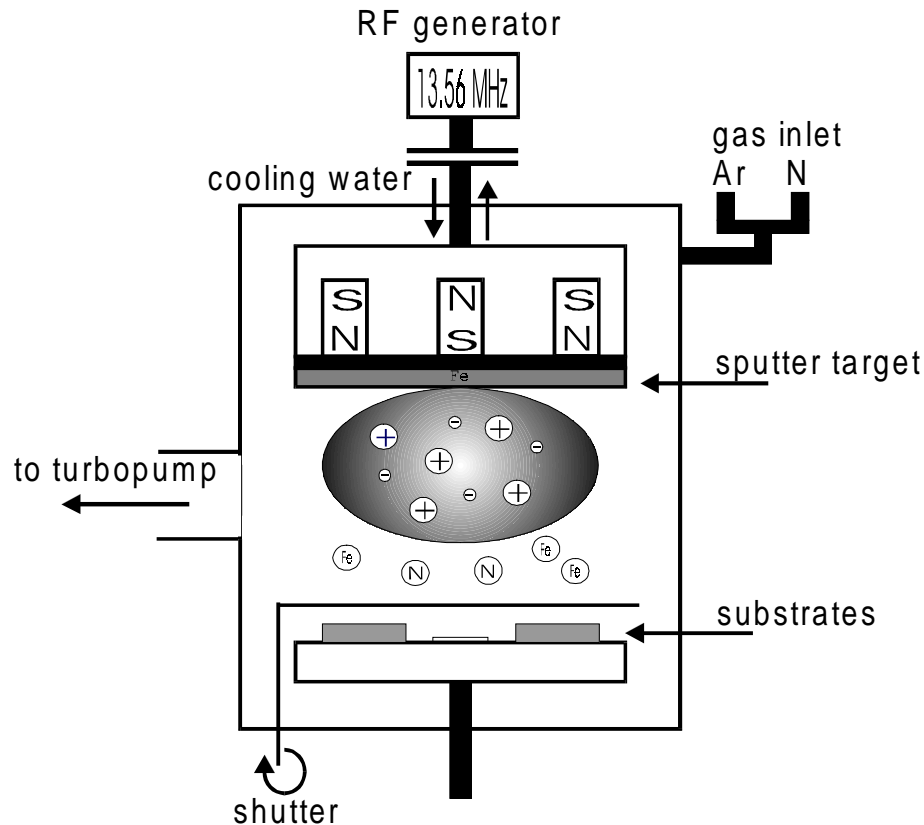


Figure 2.1: Schematic diagram of the reactive magnetron sputtering apparatus.

In part of the experiments the substrate holder was connected to an additional DC bias voltage. Immediately before deposition, the target was presputtered for at least 30 min with the shutter closed. The deposition rate varied between 0.3-1.2 nm/min, depending on the RF power and the gas flow rates. The thickness was monitored using a microbalance quartz and also independently determined by RBS. In each run several samples were deposited under identical conditions.

### Annealing treatment

Annealing of the deposited films in vacuum was done in an oven from Ströhlein Instruments (type MTF 12/25B). The vacuum during heating was about  $5 \cdot 10^{-4}$  Pa. A similar oven was used for heating in  $H_2$ -flow. Additionally, samples were sealed in a glass tube filled with  $NH_3$  at 0.1 MPa after evacuation and then heated in the oven.

### Ion implantations

The ion beam irradiations at 80 and  $\sim 300$  K were carried out using the Göttingen heavy ion implanter IONAS [18]. The  $^{132}Xe^+$  ions were directed at normal incidence on the samples. The irradiation induced effects in the near-surface region were studied with ions of 100 keV energy, and the energies of 450 and 700 keV were used to observe the ion-beam mixing at the interface of a bilayer system. The irradiation fluences ranged between  $0.5 \cdot 10^{15}$  and  $6 \cdot 10^{16}$  ions/cm<sup>2</sup>. Typical beam current measured at the target was about 1  $\mu A$  over a  $1 \times 1$  cm<sup>2</sup> surface area. Homogeneous irradiation was achieved by means of an electrostatic X-Y sweeping system. The projected ranges as well as the energy densities deposited at the interface in the bilayer were calculated with the TRIM code [19].

## 2.2 Analyzing methods

For the present work ion beam analyses, such as Rutherford Backscattering spectrometry (RBS), Time-Of-Flight Elastic Recoil Detection and Analysis (TOF-ERDA) and Resonant Nuclear Reaction Analysis (RNRA) were employed, as well as phase analysis via X-Ray Diffraction (XRD), Conversion Electron Mössbauer Spectroscopy (CEMS), and Transmission Electron Microscopy (TEM). The surface topography, especially the roughness, was measured by means of Atomic Force Microscopy (AFM). In the following sections the above mentioned methods will be presented in greater detail.

### 2.2.1 Rutherford backscattering spectrometry

The film thickness, homogeneity and stoichiometry of the samples were measured by Rutherford Backscattering spectrometry (RBS). RBS is based on the electrostatic repulsion of the nucleus, which causes the beam particles to backscatter after an elastic collision. The RBS spectrum is altered by energy loss of particles emerging from below the target's surface. The intensity of backscattered particles reflects the concentration of target atoms. The RBS spectrum contains information about the atomic masses and the distribution of target elements as a function of depth. RBS is an ideal analyzing method for heavy-mass thin films on low-mass substrate materials. Light elements are more difficult to measure due to the low signal-to-background ratio. Two elements of similar mass cannot be distinguished when they appear together in a sample. The mass resolution depends on the kinetic energy transfer from the elastically scattered particles. RBS yield depends on the number of target atoms encountered by the penetrating particles along their path. For single-crystalline materials, the incoming beam direction can be aligned with one of the major crystallographic axes of the substrate. At such conditions, called channeling, the Backscattering yield reduces. Surface nonuniformities, for example increased roughness caused by ion implantation, can drastically modify the spectrum.

The principle of RBS is sketched in Figure 2.2. The final energy  $E_f$  of an  $\alpha$ -particle of mass  $M_1$  elastically scattered from a nucleus of mass  $M_2$  at the sample surface ( $z = 0$ ) is simply calculated using the conservation of momentum and energy

$$E_f = K(M_2, \theta)E_i = \left[ \frac{(M_2^2 - M_1^2 \sin^2 \theta)^{1/2} + M_1 \cos \theta}{M_1 + M_2} \right]^2 \cdot E_i \quad (2.1)$$

where  $E_i$  is the initial energy and  $\theta$  the scattering angle in the laboratory system.  $K$  denotes the kinematic factor for the elastic scattering process.

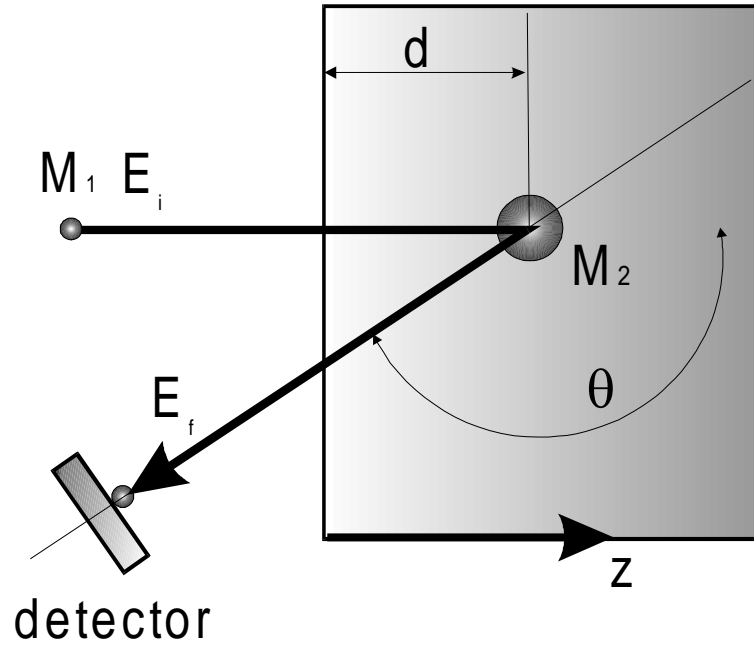


Figure 2.2: Schematic presentation of RBS method.

For any combination of projectile and target mass, the kinematic factor has its lowest value at  $\theta=180^\circ$ . For fixed  $\theta$ , the energy separation,  $\Delta E_1$ , for beam particles scattered by target particles of mass difference  $\Delta M_2$  is

$$\Delta E_1 = E_i \left( \frac{dK}{dM_2} \right) \Delta M_2. \quad (2.2)$$

If  $\Delta E_1$  is set equal to  $\delta E$ , the minimum energy separation that can be experimentally resolved, then  $\delta M_2$ , the mass resolution of the system is

$$\delta M_2 = \frac{\delta E}{E_0 \left( \frac{dK}{dM_2} \right)}. \quad (2.3)$$

The mass resolution at the sample surface is usually determined primarily by the detector resolution, while deeper in the layer the straggling dominates.

The yield of backscattered particles, i.e. the probability for backscattering, is determined by the cross-section of the scattering process. The intensity  $I$  of  $\alpha$ -particles reaching the detector with a solid angle  $d\Omega$  depends on the area  $A$ , the incident intensity  $I_0$  and the atomic density  $N$  as follows

$$\frac{dI}{d\Omega} = \frac{I_0 N}{A} \frac{d\sigma}{d\Omega} \quad (2.4)$$

If the force between the beam particle and the target nucleus is assumed to be the Coulomb force, the differential cross-section  $d\sigma/d\Omega$  results in the expression of the Rutherford cross-section in the laboratory system

$$\frac{d\sigma}{d\Omega} = \left( \frac{Z_1 Z_2 e^2}{4E} \right)^2 \frac{4}{\sin^2 \theta} \frac{\left[ 1 - \left( (M_1 / M_2) \sin \theta \right)^2 \right]^{1/2} + \cos \theta}{\left[ 1 - \left( (M_1 / M_2) \sin \theta \right)^2 \right]^{1/2}} \quad (2.5)$$

$d\sigma/d\Omega$  is proportional to  $Z_2^2$  which means that for any given projectile, heavy atoms are much more efficient scatterers than light ones. The proportionality to  $1/E^2$  rises the scattering yield with decreasing bombarding energy.

The  $\alpha$  particle backscattering from the deeper parts of the sample undergoes inelastic scattering with the electron cloud of the target atoms and loses energy smoothly on its way into and out of the material. The final energy of the emerging  $\alpha$ -particle becomes

$$E_f = K(E_i - \Delta E_{in}) - \Delta E_{out} \quad (2.6)$$

The calculation of the energy loss involves the integration of the stopping power

$$E_f = K \cdot \left( E_i - \int_0^d \frac{dE}{dz}(z) dz \right) - \int_0^d \frac{dE}{dz}(z) \frac{dz}{\cos \theta}. \quad (2.7)$$

The radii of atomic nuclei are so small compared with atomic dimensions that nuclear scattering is rare compared to interactions with electrons. When the projectile velocity  $v$  is much greater than that of an orbital electron, the influence of the incident particle on an atom may be regarded as a sudden, small external perturbation. The increasing velocity decreases the stopping cross-section.

The nuclear stopping power, i.e. elastic collisions, becomes important only at low ion energies. In the low energy regime,  $v < v_0 \cdot \sqrt{Z_t}$  ( $Z_t$  is the target charge number and  $v_0$  the Bohr velocity), the stopping power is proportional to the velocity. Then the contribution of the electronic stopping diminishes due to electronic screening described by Coulomb potential.

The stopping power of a material is defined as the energy loss per distance traveled in the material,  $dE/dz$ , and it depends on the ion and the material as well as on the energy of the ion. The Bragg rule is used to calculate stopping powers of compound targets. This approximation assumes that each target atom acts independently in the energy loss process.

$$\frac{dE}{dz} = N \sum c_i \varepsilon_i \quad (2.8)$$

where  $N$  is the atomic target density,  $c_i$  and  $\varepsilon_i$  are the concentration and stopping cross section for element  $i$ , respectively. The Bragg rule intends that the interactions between the incident ion and target atoms do not depend on the environment; phase effects and chemical bonds are disregarded.

Energy loss is a statistical process. Both the electronic and nuclear energy loss contributes to the straggling. Lindhard and Scharff [20] gave an extended estimate of the straggling, so called LS-straggling

$$\Delta E_{LS}^2 = \frac{\Delta E_{Bohr}^2 L(\chi)}{2} \quad (2.9)$$

with

$$L(\chi) = 1.36\chi^{1/2} - 0.016\chi^{3/2} \quad (2.10)$$

and

$$\chi = \frac{v^2}{Z_2 v_0^2} \quad (2.11)$$

The energy straggling according to Bohr [21] in the target depends only on the atomic numbers and increases with the penetrated depth

$$\Delta E_{Bohr}^2 = 4\pi Z_1^2 Z_2 e^4 z \quad (2.12)$$

Equation (2.12) offers a good approximation of the straggling and has a gaussian form at large depths. It is important to note that Bohr straggling does not depend on ion velocity.

The depth resolution  $\Delta z$  depends on the stopping power  $dE/dz$ , the detector resolution  $\Delta E_{det}$  (=12-15 keV) and the beam energy spread  $\Delta E_{beam}$  of the incident particles

$$\Delta z \frac{dE}{dz} = \sqrt{\Delta E_{beam}^2 + \Delta E_{LS}^2 + \Delta E_{det}^2} \quad (2.13)$$

Usually the beam spread  $\Delta E_{beam}$  ( $\sim 79$  eV for 900 keV  $\text{He}^{2+}$  at IONAS) can be neglected, since it is much smaller than the energy resolution of Si surface-barrier detectors. The detector resolution can be experimentally determined from the high-energy edge of a heavy element (i.e. Au, Ti, Fe, ...) peak.

In Figure 2.3 a typical RBS spectrum of a  $\text{Ni}_3\text{N}$  film on a silicon substrate irradiated by 100 keV Xe ions is presented. At higher energies the peak of the implanted Xe is visible and at lower energy starts the Ni signal. The dip in the nickel signal is due to the implanted Xe distribution and, indeed, illustrates the fact that the Xe ions have not reached the  $\text{Ni}_3\text{N}/\text{Si}$  interface. The irradiation has increased the surface roughness, which is indicated by the increased broadening of the interface  $\text{Ni}_3\text{N}/\text{Si}$  when it is compared to the as deposited sample (not shown here). Due to energy lost of the ions travelling through the top nitride layer the silicon edge has moved towards the lower energies.

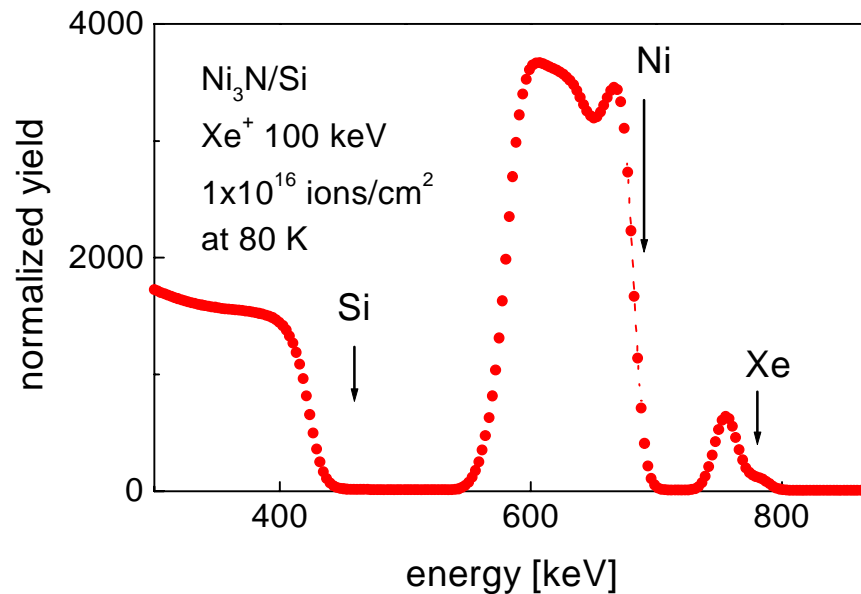


Figure 2.3: RBS spectrum of a 100 keV Xe-ion irradiated  $\text{Ni}_3\text{N}/\text{Si}$  sample.

The information about the ion-beam induced atomic transport processes is obtained from the RBS data by comparing the spectra before and after the sample irradiation. The atomic distribution at the interface of a bilayer system can be given by an error-function like profile. The distance between the 16 and 84 % of the maximum concentration of the RBS peak of a certain element (see Figure 2.4) determines the interface variance  $\sigma_{\text{int}}$ , describing the broadening of the interface region.

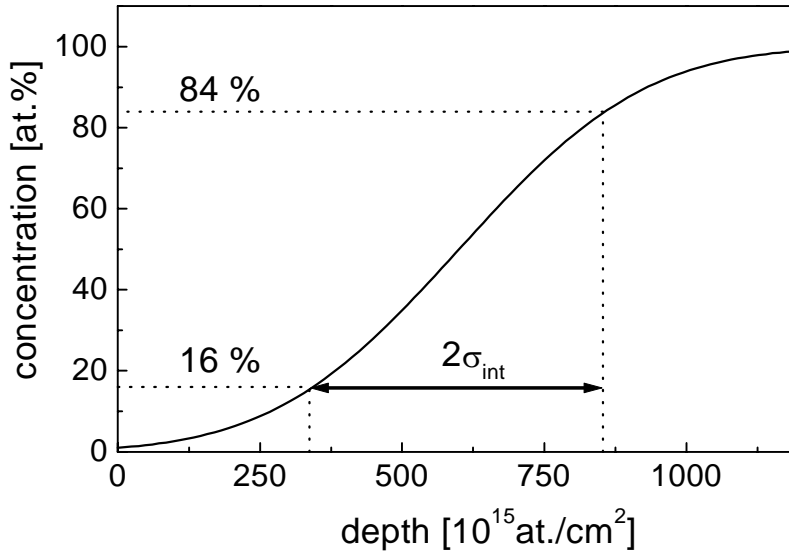


Figure 2.4: The determination of the interface variance.

As mentioned above, both the surface and the interface roughness broaden the RBS signal. Therefore, in order to measure the mixing purely due to processes taking place at the interface the surface roughness has to be subtracted from the interface variance. If both parameters are statistically distributed

$$\Delta\sigma_{\text{interface}}^2 = \Delta\sigma_{\text{RBS}}^2 - \Delta\sigma_{\text{surface}}^2 \quad (2.14)$$

The RBS spectra were measured using 900 keV  $\alpha$ -particles at the Göttingen ion implanter IONAS [18]. The beam diameter was about 2 mm, and the current was set to 15 nA. The backscattered  $\alpha$ -particles were registered at an angle of  $165^\circ$  relative to the beam by means of two Si surface detectors. The spectra were analyzed employing the RUMP code [22]. The nickel and iron concentrations were determined by RBS with an accuracy of about 2-3 at.%.

### 2.2.2 Time of flight elastic recoil detection and analysis

TOF-ERDA is an ion beam analysis technique for quantitative analysis of light elements in near-surface solid layers [23,24]. The sample which has to be analyzed is irradiated with a heavy ion beam (I, Au or Ag ions) of several MeV energy. Light elements (H, D, O, C, etc.) from the sample are scattered in forward directions and can be detected with a Si detector. In addition to energy measurement, time-of-flight over a known flight distance is measured for each atom by means of two thin (some  $\mu\text{g}/\text{cm}^2$ ) carbon foils. When passing through the foil the recoiled atom causes the emission of secondary electrons, which are accelerated by electric fields to microchannel plates

where passage time signals are generated. The elastic collision between the beam particle with mass  $M_1$  and the target atom of mass  $M_2$  in the laboratory frame is presented in Figure 2.5.

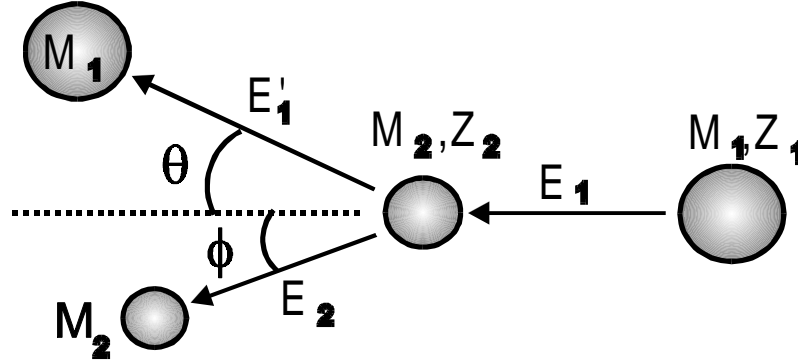


Figure 2.5: Elastic scattering between the target,  $M_2$ , and beam particle,  $M_1$ , in the laboratory frame.

The conservation of energy and momentum give the energy of the recoiled atom

$$E_2 = E_1 \frac{4M_1M_2}{(M_1 + M_2)^2} \cos^2 \phi \quad (2.15)$$

and the energy of the incident ion after the elastic collision

$$E_1' = E_1 \left( \frac{\sqrt{M_2^2 - M_1^2 \sin^2 \phi} + M_1 \cos \phi}{M_1 + M_2} \right)^2 \quad (2.16)$$

The  $E_1$  is the energy of the incident ion and  $\phi$  is the angle between the incident beam and the recoiled atom direction.

The spectrum obtained in TOF-ERDA measurements consists of the time-of-flight and energy information. In order to identify of the different elements, the TOF-E-spectrum is transformed into the mass-TOF-form with the help of the classical formula of the kinetic energy

$$E_2^{TOF} = \frac{M_2 v_2^2}{2} = \frac{M_2 L^2}{2t^2} \quad (2.17)$$

where  $v_2$  is the velocity of the recoiled atom,  $L$  the path length between the timing detectors and  $t$  the time-of-flight. The more accurate time-of-flight signal gives a better energy resolution than the signal from the energy detector. Every energy channel corresponds to a certain depth  $z$  in the sample. When the stopping power of the incident ion and the recoiled atom in the sample material are known, the depth at which the elastic collision took place can be calculated.

For low ion energies ( $< 0.3$  MeV/amu) the scattering cross section can be calculated assuming Rutherford scattering which in the laboratory reference frame is

$$\frac{d\sigma}{d\Omega} = \frac{[Z_1 Z_2 e^2 (M_1 + M_2)]^2}{(2M_2 E_1)^2 \cos^3 \phi} \quad (2.18)$$

where  $Z_1$  and  $Z_2$  are the charge numbers of the incident ion and the recoiled atom, respectively, and  $e$  is the electric charge. Since the beam energies used in TOF-ERDA are quite large ( $E > 10$  MeV) the electronic stopping dominates over nuclear stopping.

The mass resolution of the TOF-ERDA method is good enough to differentiate the light masses ( $A < 30$ ) totally. The main source of systematic errors in the analysis of TOF-ERDA data is the uncertainty of the stopping power values used. When considering the depth resolution the effect of the finite solid angle of the spectrometer system and the time resolution of the TOF measurement are the main factors near the surface. Deeper in the sample the effect of multiple scattering of the beam and recoiling particles becomes dominant.

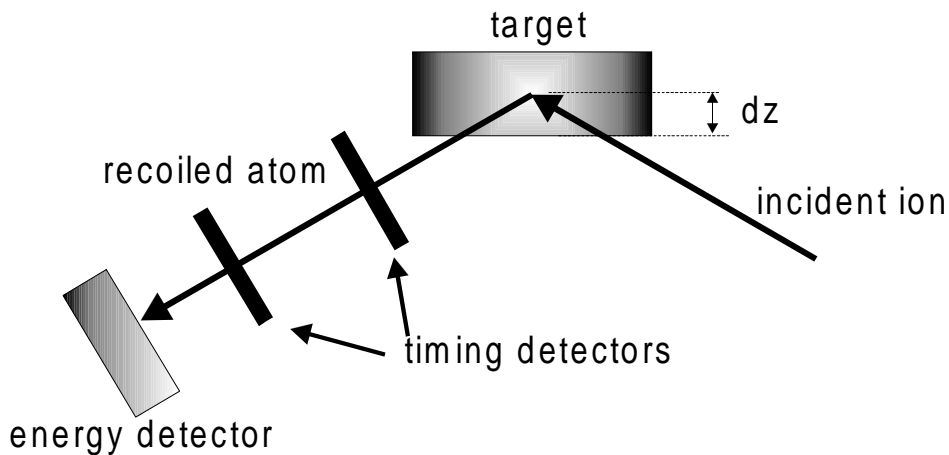


Figure 2.6: A schematic picture of the TOF-ERDA measurement set-up.

The TOF-ERDA experimental setup used at the University of Helsinki is schematically represented in Figure 2.6. A high-energy ion beam,  $^{197}\text{Au}^{7+}$ ,  $^{107}\text{Ag}^{6+}$  or  $^{127}\text{I}^{7+}$  ions at 37 MeV, from the 5 MV tandem accelerator EGP-10-II was directed on the sample so that the angle between the normal of the sample surface and the incident beam as well as the recoiled atoms was  $70^\circ$ ; then  $\phi = 40^\circ$ . The distance between the time detectors is 68.4 cm and the ion-implanted silicon detector for the energy measurement was located after the second timing detector at a distance of 124.3 cm from the sample.

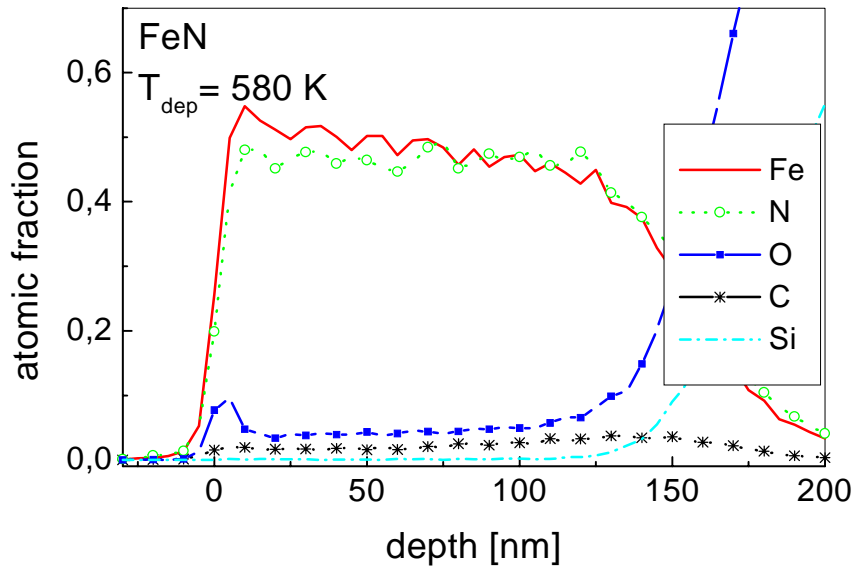


Figure 2.7: A TOF-ERDA spectrum of a FeN sample deposited on silicon at 580 K.

Concentration profiles of a magnetron sputtered iron nitride sample as a function of depth are illustrated in Figure 2.7. TOF-ERDA revealed that the FeN film has more or less the correct ratio 1:1 of Fe to N. The iron concentration decreases slightly with the increasing depth. The nitride film contains some atomic percents of light impurity elements (C and O).

### 2.2.3 Resonant nuclear reaction analysis (RNRA)

The power and also the limitation of the Resonant Nuclear Reaction Analysis lies on the fact that it is sensitive to specific isotopes. Other ion-beam methods, like RBS, ERDA and PIXE, provide a simple and systematic way to detect elements in an unknown sample. In RNRA every resonant reaction has its own characteristics, the resonance energy,  $E_R$ , the energy of the out-coming gamma ray,  $E_\gamma$ , (in most of the reactions), the cross-section, etc. On the other hand, when these quantities are known, RNRA provides an efficient and non-destructive way to obtain accurate depth profiles of certain isotopes.

In the resonant reaction, the incoming particle forms a nuclear compound state before the outgoing particle is ejected, and in many reactions a  $\gamma$ -ray emitted. Figure 2.8 shows a typical RNRA measurement set-up. Narrow resonance reactions are favored in low-mass elements ( $Z < 30$ ) due to weak Coulomb barriers. The incident energies needed for the light ion beam particles are in the range of few hundred keV, the cross-sections large and the widths of the resonances small. The nuclear reaction of  $^{15}\text{N}(p,\alpha\gamma)^{16}\text{O}$  at  $E_{\text{res}}=429.6$  keV is particularly interesting for the present purpose. It has a very small line width,  $\Gamma=120$  eV, high cross-section  $\sigma=300$  mb, and the resonance has no interference with other reactions. The natural abundance of  $^{15}\text{N}$  is 0.37 %.

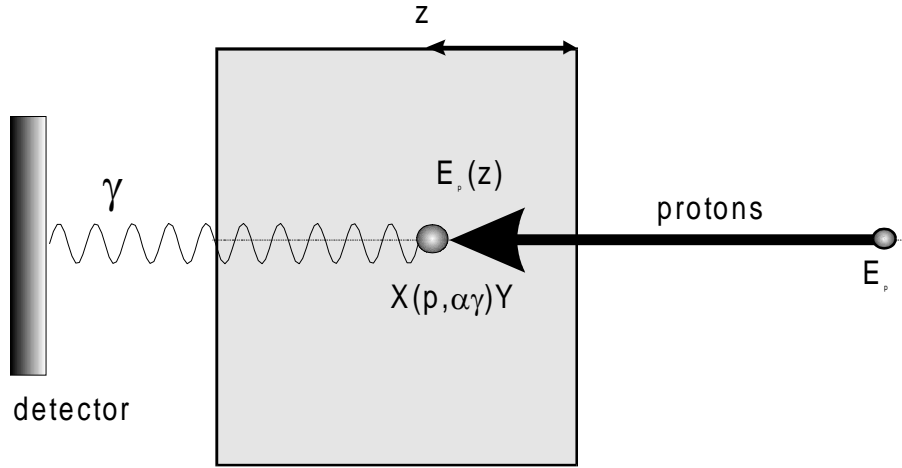


Figure 2.8: Schematical presentation of the RNRA method using a  $(p, \alpha\gamma)$  reaction.

The depth profiling of the nitrogen content is performed by directing the analyzing proton beam onto the sample and the 4.439 MeV  $\gamma$ -ray yield is measured as a function of the incident beam energy  $E_0$ . For  $E_0 = E_{res}$  the nuclear reaction takes place at the surface. The protons entering the sample are slowed down. For higher incident energies, the reaction will be induced at a depth  $z(E_0)$ , at which the beam particles have slowed down to the resonance energy. The depth  $z(E_0)$  is given by

$$z(E_0) = \int_{E_{res}}^{E_0} \left(\frac{dE}{dz}\right)^{-1} dE \quad (2.19)$$

Bragg's rule is used to estimate the proton stopping power of compound samples.

The depth is determined by the energy of the proton beam, the depth resolution by the resonance width and the energy straggling of the protons. It becomes below the sample surface

$$\Delta z = \frac{\Delta E_{tot}}{dE/dz} \quad (2.20)$$

with

$$\Delta E_{tot} = \sqrt{\sigma_{res}^2 + \sigma_{beam}^2 + \sigma_{dopp}^2 + \sigma_{stragg}^2} \quad (2.21)$$

The thermal motion of the target atoms induces a spread by the Doppler effect  $\sigma_{dopp}^2$ .  $\sigma_{stragg}$  is calculated by using the LS straggling approximation. At the surface the depth resolution is less than 1 nm, while below the sample surface it increases approximately proportional to  $\sqrt{z}$ .

The measured  $\gamma$ -yield as a function of the incident proton energy is given by

$$Y(E_0) = \varepsilon_{det} \Omega N_p \int_0^\infty \int_0^\infty \int_0^\infty c(z) g(E_0, E) f(E_0, E', z) \sigma(E') dE' dE dz \quad (2.22)$$

where  $\varepsilon_{det}$  is the efficiency of the detector with a solid angle  $\Omega$  and  $N_p$  is the number of incident protons. The cross-section has the Breit-Wigner form

$$\sigma(E) = \sigma_0 \frac{\Gamma_{in} \Gamma_{out}}{(E - E_0)^2 + (\Gamma/2)^2} \quad (2.23)$$

$\Gamma_{in}$  and  $\Gamma_{out}$  are free particle widths of the resonance.  $\sigma_0$  is the cross-section at the resonant energy 429.6 keV,  $\sigma_0=300$  mb,  $\Gamma=120$  eV is the resonance width.  $C(z)$  is the isotope concentration at depth  $z$ ,  $g(E_0,E)$  is the distribution of the initial beam energy of the proton beam

$$g(E_0, E) = \frac{1}{\sigma_{beam} \sqrt{2\pi}} \exp\left(-\frac{(E_0 - E)^2}{2\sigma_{beam}^2}\right) \quad (2.24)$$

The energy spread of a beam of singly charged particles at the IONAS accelerator [25] is given by the following equation

$$\sigma_{beam}(eV) = 2.09 \cdot 10^{-4} (E_0 - 30keV)^2 + 2.55 \quad (2.25)$$

For protons at the energy of 430 keV  $\sigma_{beam}$  is 36 eV, while the Doppler broadening at 80 K is approximately 40 eV.  $F(E,E',z)$  is the probability of a proton with the incident energy to possess as energy of  $E'$  at the depth of  $z$ .

In order to obtain accurate N-concentration profiles the background and possible interfering resonances have to be subtracted. The background is mainly due to natural background radiation, competing reactions, reactions in slits collimating the beam and noise in the electronics. A typical  $\gamma$ -ray spectrum of the  $^{15}\text{N}(p,\alpha\gamma)^{16}\text{O}$  reaction taken with a NaI-detector is shown in Figure 2.9. The reaction is indicated by the 4.439 MeV photopeak and the corresponding escape peaks. The yield curve was obtained by integrating over the range of  $E_1$  to  $E_2$  including the escape peaks. A background subtracted  $\gamma$ -yield curve vs. incident proton energy is displayed in Figure 2.10a. The background correction was performed by off-resonance measurements. The nitrogen concentration profiles were obtained using a deconvolution program [26,27], dividing the sample into appropriate layers with a constant nitrogen content and calculating the energy loss and energy straggling of the incident proton beam. Such a transformed nitrogen depth profile is displayed in Figure 2.10b.

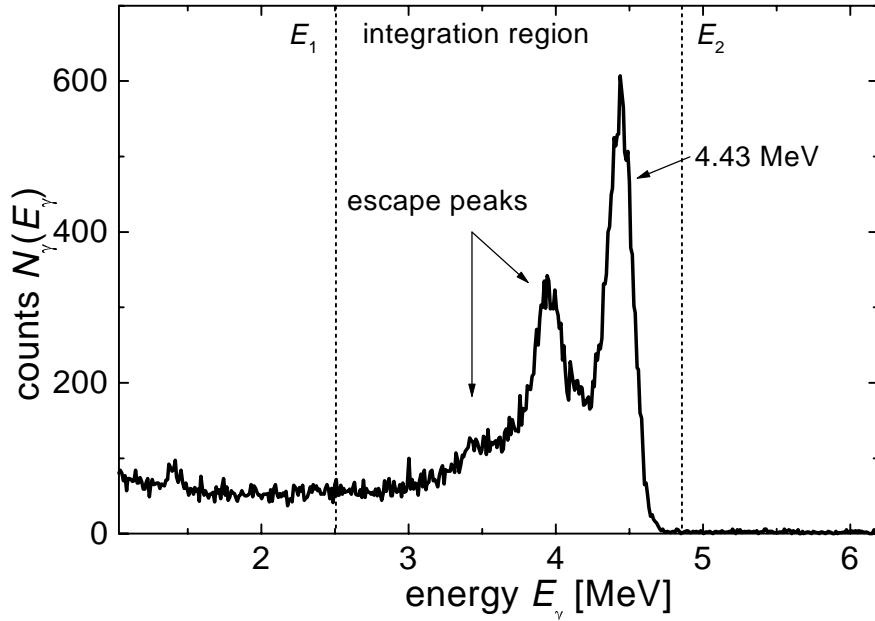


Figure 2.9: Measured gamma-ray spectrum for a CrN calibration sample using a NaI detector.

The measured  $\gamma$ -ray yield of an element B from a sample  $A_aB_b$  ( $a+b=1$ ) can be converted into the concentration by

$$C_B(z) = 100 \cdot \frac{f_{st} Y_{A_aB_b}(z) \varepsilon_B}{Y_{st} \varepsilon_{st} + f_{st} Y_{A_aB_b}(z) (\varepsilon_B - \varepsilon_A)} \text{ at. \%} \quad (2.26)$$

where  $Y_{st}$  is the  $\gamma$ -yield measured for a standard sample, in this case CrN prepared by magnetron sputtering, with a known atomic fraction  $f$  of the element B.  $\varepsilon$ 's are the corresponding stopping cross-sections.

A simple approximation can be obtained for calculating the depths corresponding to incident proton energies increasing from  $E_{i-1}$  to  $E_i$

$$z(E_i) = z(E_{i-1}) + \frac{2(E_i - E_{i-1})}{\varepsilon(E_i) + \varepsilon(E_{i-1})} \quad (2.27)$$

where  $\varepsilon(E_i)$  is the stopping power of the sample at the energy  $E_i$ .

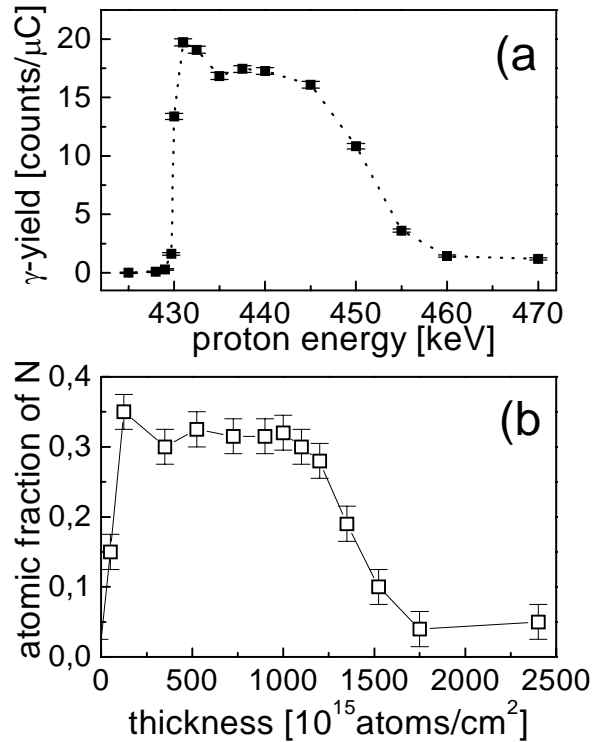


Figure 2.10: a) Normalized  $\gamma$ -yield for a magnetron sputtered Fe film obtained by RNRA. b) Nitrogen concentration profile obtained by the deconvoluting program.

In this work, the nitrogen depth profiles were obtained using the reaction  $^{15}\text{N}(p,\alpha\gamma)^{12}\text{C}$  at 429.6 keV resonant energy. A well-defined proton beam was directed on the samples, having a diameter of 3 mm, from the IONAS accelerator. During all the measurements the samples were cooled to 80 K in order to avoid changes due to diffusion or annealing effects induced by the 2  $\mu\text{A}$  analyzing proton beam. The thickness and composition calibrations were performed using a CrN reference sample with known nitrogen concentration. The 4.43 MeV  $\gamma$ -radiation was measured in a 12 cm long NaI detector with a 16 cm diameter.

#### 2.2.4 Mössbauer spectroscopy

The gamma radiation can be emitted and absorbed resonantly and recoilless from nuclei in solids [28,29]. This so-called Mössbauer effect results in an extremely well defined energy of the gamma radiation and makes it possible to study the hyperfine interactions between the nucleus and its surroundings. For solids containing suitable Mössbauer nuclei one gains information on the magnetic, chemical and crystallographic properties of the solid. In particular, the Mössbauer method can be used for a non-destructive analysis of samples containing more than one phase. This resonant absorption is observed best in isotopes having long-lived, low-lying excited nuclear energy states. Among all the elements, the largest recoil-free resonant cross-section occurs for the isotope  $^{57}\text{Fe}$ . Figure 2.11 shows the decay of  $^{57}\text{Fe}$  from its parent  $^{57}\text{Co}$ . The excited state of  $^{57}\text{Fe}$  emits a 14.4 keV gamma ray via a magnetic dipole transition from the metastable  $I = 3/2$  state to the  $I = 1/2$  ground state. The linewidth (FWHM) of the emitted radiation is  $\Gamma = 124$  eV. EC denotes to the electron capture.

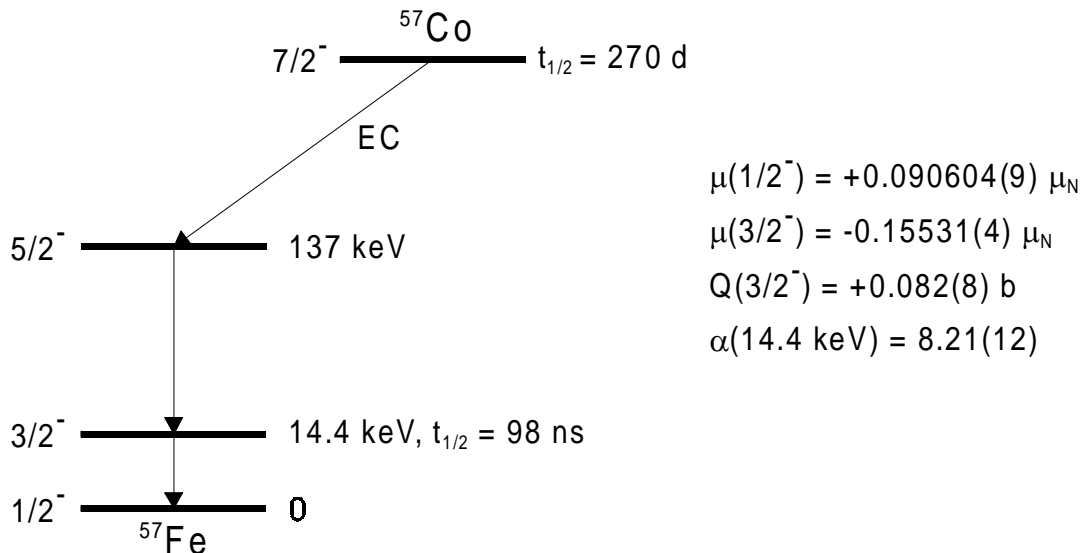


Figure 2.11: The decay scheme of <sup>57</sup>Co.

Conventionally in Mössbauer measurements, the  $\gamma$ -source is mounted on a driving unit and moved oscillatory with a small velocity in order to modulate the  $\gamma$ -ray energy. Due to the motion the energy of the emission line is shifted by the Doppler effect. When the source is moved at the velocity  $v$ , the change in the energy of the  $\gamma$ -ray  $\Delta E_D$  emitted toward the direction of the movement is given by

$$\Delta E_D = \left( \frac{v}{c} \right) E_\gamma \quad (2.28)$$

where  $c$  is the velocity of light in vacuum. In the case of <sup>57</sup>Fe-source the velocity of 1 mm/s varies the 14.4 keV  $\gamma$ -ray energy by  $\Delta E_D = 4.79 \times 10^{-8} \text{ eV}$ . The value is small compared to the  $\gamma$ -ray energy and therefore enables the observation of changes in the hyperfine structure. When the energy of the emitted  $\gamma$ -ray coincides with a transition in the sample, some of the gamma quanta are absorbed resonantly. The probability of the Mössbauer process to take place is expressed with the recoilless fraction  $f$  written as follows

$$f = \exp \left[ - \frac{3E_R}{2k_B \theta_D} \left( 1 + 4 \left( \frac{T}{\theta_D} \right)^2 \int_0^{\theta_D/T} \frac{udu}{e^u - 1} \right) \right] \quad (2.29)$$

where  $k_B$  is the Boltzmann constant,  $T$  temperature,  $\theta_D$  Debye temperature,  $E_R$  recoil energy and  $u$  is a stationary state of the solid. The equation shows that the lower the temperature and the  $\gamma$ -ray energy the better the Mössbauer effect is observed. The recoil-free fraction of <sup>57</sup>Fe is so large that the measurements can be carried out at room temperature.

### Conversion Electron Mössbauer Spectroscopy (CEMS)

An alternative to the detection of  $\gamma$ -rays is to register the internal conversion electrons that are re-emitted during the decay of the excited absorber nuclei. This method is called Conversion Electron Mössbauer Spectroscopy. The plot of the conversion electron yield as a function of the source velocity produces a spectrum similar to that from conventional Mössbauer spectroscopy. Of all the excited <sup>57</sup>Fe nuclei, about 10 % will emit a 14.4 keV gamma ray. The various processes which occur when the gamma ray is absorbed by the <sup>57</sup>Fe nucleus, and their probabilities are

represented in Figure 2.12 [30]. The energy of the emitted electrons (few keV) dictates that only those from up to the depth of 0.5  $\mu\text{m}$  can escape to be detected.

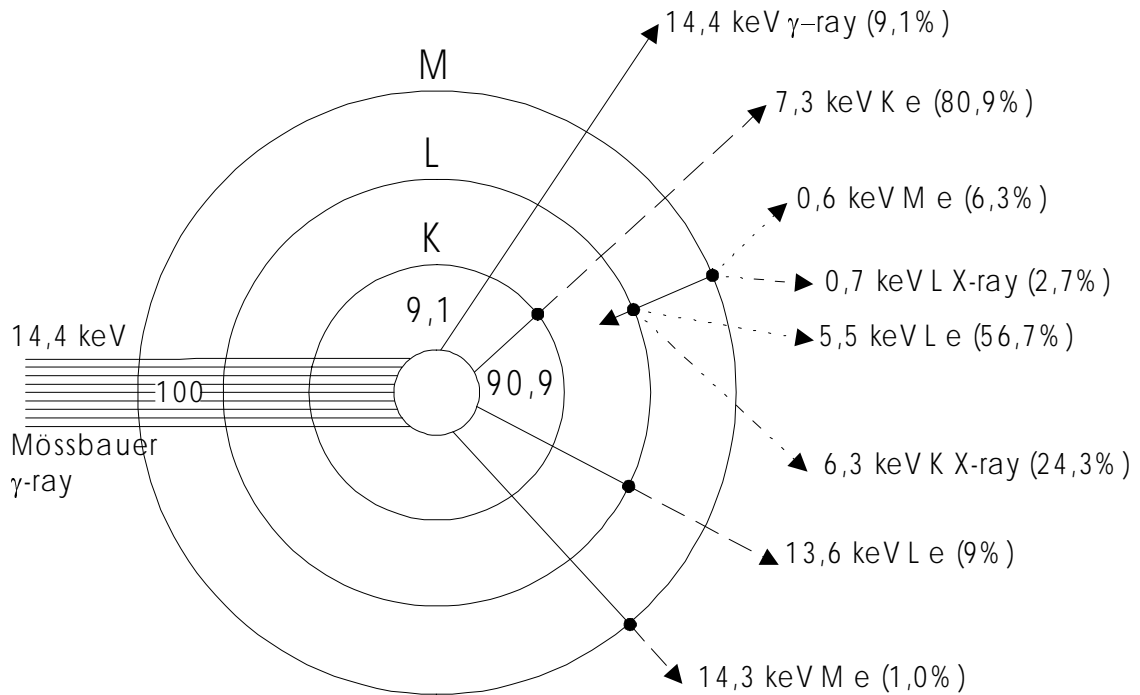


Figure 2.12: Internal conversion

### Hyperfine interactions

The energy levels in the nucleus of the absorbing atom are affected by all electrons (especially by s-electrons), which have nonzero wavefunctions at the position of the nucleus. The excited  $^{57}\text{Fe}$  nucleus has a slightly smaller radius than the ground state, which causes the Mössbauer transition energy to depend on the energy density at the nucleus and produces the so-called **isomer shift** of the Mössbauer spectrum. If the source and the absorber (sample) nuclei are in the same electronic state, the energies of emitted and absorbed  $\gamma$ -ray are the same and thus the Mössbauer line is observed at the zero velocity. In general nuclei in the source and absorber are in different chemical states and have therefore different s-electron densities at the nucleus. The center of the resonance moves away from the zero velocity. The energy level scheme of this shift is illustrated in top part of Figure 2.13 and may be written as

$$\delta = \frac{2}{5} \pi Z e^2 \left[ |\Psi_A(0)|^2 - |\Psi_S(0)|^2 \right] \left[ R_e^2 - R_g^2 \right] \quad (2.30)$$

$R$  is the nuclear rms radius (the excited = e and the ground = g state),  $e|\Psi(0)|^2$  the electron density ( $S$  = the source and  $A$  = the absorber) at the nucleus and  $Z$  is the charge value. The more d electrons are present, the more the nucleus is shielded from s electrons. This forces the s cloud to expand, reducing the density at the nucleus.

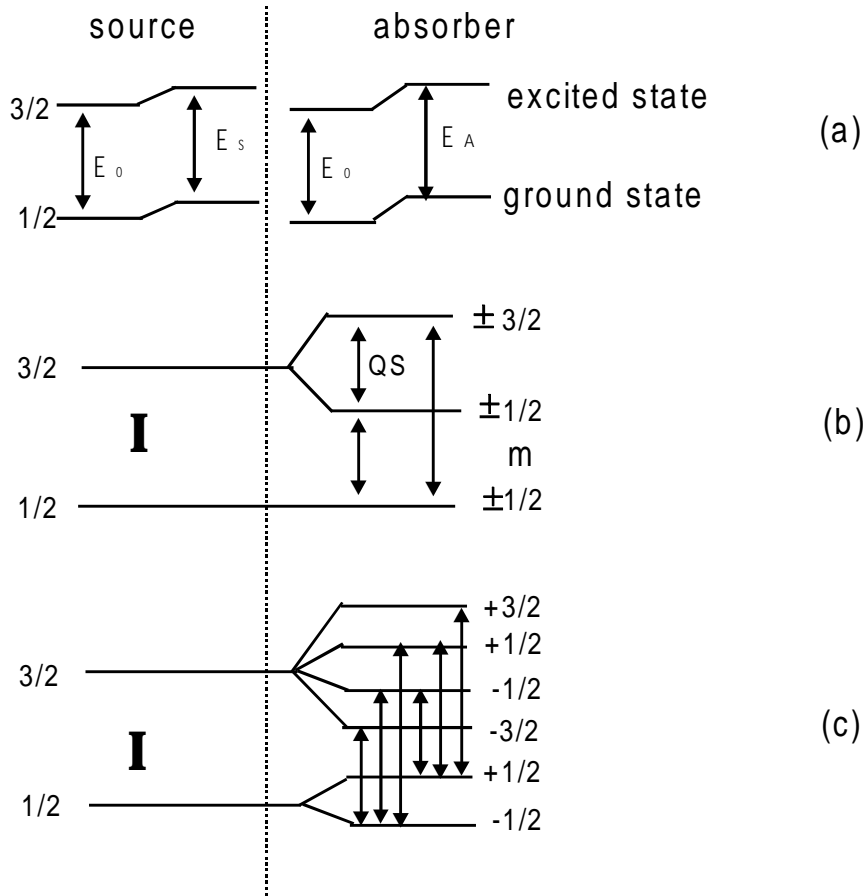


Figure 2.13: Schematic drawing of energy levels of  $^{57}\text{Fe}$  in a) isomer shift, b) quadrupole splitting and c) magnetic hyperfine interaction.

When the nuclear spin  $I \geq 1$  the charge distribution of the nucleus is distorted from spherical symmetry, and the nucleus has a non-zero quadrupole moment. The excited ( $I = 3/2$ ) state of the  $^{57}\text{Fe}$  nucleus possesses an **electric quadrupole moment**, and the presence of an asymmetric electric field gradient (EFG) will orient the nuclear spin. The interaction has the form

$$QS = \frac{eQV_{zz}}{4I(2I-1)} \left[ 3m_l^2 - I(I+1) \right] \sqrt{1 + \frac{1}{3}\eta^2} \quad (2.31)$$

where  $Q$  is the nuclear quadrupole moment,  $\eta$  the asymmetry parameter of the EFG and  $V_{zz}$  the EFG tensor. The elements of the efg tensor are

$$V_{ij} = \frac{\partial^2}{\partial r_i \partial r_j} V \quad (2.32)$$

$i, j = x, y, z$

where  $V$  is the electrostatic potential due all the charges outside the nucleus. By convention,  $x$ ,  $y$ , and  $z$  are chosen so that  $|V_{zz}| \geq |V_{yy}| \geq |V_{xx}|$ , which forces the asymmetry parameter,  $\eta = (V_{xx} - V_{yy})/V_{zz}$ , to be in the range of  $0 \leq \eta \leq 1$ .

Reversal of the sign of the nuclear spin will not change the nuclear charge distribution; therefore the efg will not completely lift the fourfold degeneracy of the  $I=3/2$  states (Figure 2.13b). The quartet will be split into two doublets, while  $I=1/2$  states will remain degenerate. Since two transition energies are now possible, two absorption peaks will appear in the Mössbauer spectrum.

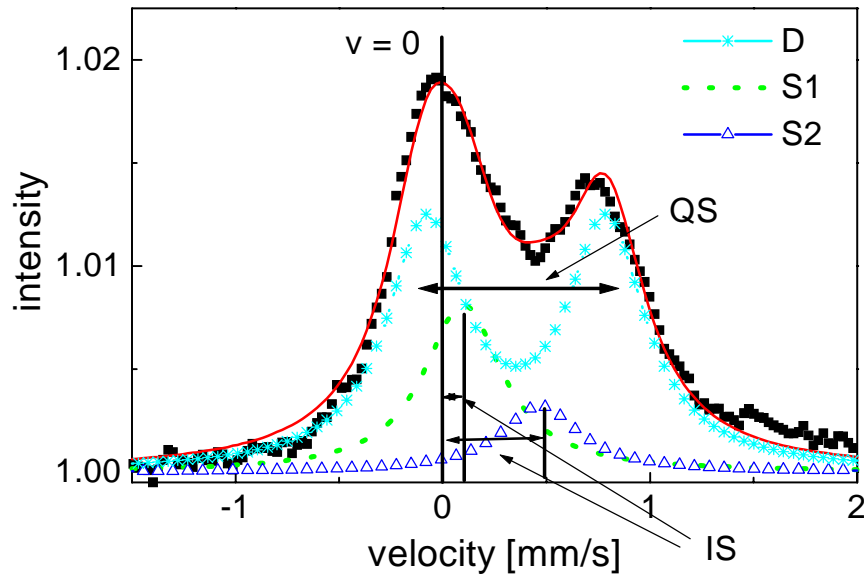


Figure 2.14: CEM spectrum of FeN thin film deposited on silicon by magnetron sputtering.

The thin ( $\sim 100$ - $200$  nm) iron nitride films produced in this study were measured by CEMS. The method is useful especially in analyzing thin films. In Figure 2.14 a CEMS spectrum of FeN sample clearly reveals the different phases present in the sample. The spectrum is deconvoluted into two single lines (S1 and S2) and a quadrupole doublet (QS). The isomer shifts of the two singlets, e.g. the distance from the zero velocity, have been indicated by IS and the quadrupole splitting by QS. The hyperfine parameters of the subspectra are summarized in Table 1.

Table 1. Hyperfine parameters of FeN.

Subspectra	$\delta$ [mm/s]	QS [mm/s]
S1	0.09(3)	
S2	0.48(5)	
D	0.32(2)	0.77(11)

The CEMS spectrum exhibits a quadrupole doublet QS which is due to the electrically asymmetric environment of the Fe atoms in the FeN lattice. The difference in energy of the two peaks for  $^{57}\text{Fe}$  can be given as

$$QS = \frac{Q}{2} V_{zz} \left(1 + \frac{\eta^2}{3}\right)^{1/2} \quad (2.33)$$

The sign of QS can not be determined from the spectrum, nor can the individual vector of  $V_{zz}$  and  $\eta$ .

In analogy to the electric quadrupole interaction, the **magnetic hyperfine interaction** can be used to determine values of the nuclear magnetic dipole moment or the magnetic field  $H$  acting in the nucleus. The magnetic field is contributed from the interaction between the nucleus and (a) the s-electrons which is called the fermi contact interaction, (b) the orbital magnetic moment which is due to the orbital current of electrons, and (c) the spin moment of outer electrons of parent atom which is called dipole interaction. The magnetic field at the nucleus is mainly created via Fermi contact,  $H_F$ , which is written as

$$H_F = -\frac{16\pi}{3}\mu_B \sum (S_\uparrow - S_\downarrow) \quad (2.34)$$

where  $S_\uparrow$  and  $S_\downarrow$  correspond to the magnetic field created by s-electrons antiparallel or parallel to the magnetic moment of d-shell, respectively. In the presence of a magnetic field  $H$  the energy levels are obtained from

$$E_M(m_I) = -g\mu_N H m_I \quad (2.35)$$

( $m_I = I, I-1, \dots, -I$ )

where  $\mu_N$  is the nuclear magneton and  $g$  is the gyromagnetic ratio.  $2I+1$  magnetic sublevels are equally spaced having a separation of  $g\mu_N H$  between the sublevels. The  $^{57}\text{Fe}$  nucleus experiences this interaction in both its excited and ground states. The small energy differences between the magnetic substates  $m_i$  and  $m_j$  at the ground state are

$$\Delta E_{m_{ij}}(g) = g\mu_N H(m_i - m_j) \quad (2.36)$$

and at the excited state

$$\Delta E_{m_{ij}}(e) = \frac{\delta}{c} E_0 - g\mu_N H(m_j - \frac{g^*}{g} m_i^*) \quad (2.37)$$

where  $\delta$  is the induced isomer shift and  $g^*/g$  the ratio of the gyromagnetic moments of the excited and ground levels, respectively. Only the transitions with  $\Delta m_I = \pm 1$  are allowed which results six lines in the spectrum. Figure 2.13c shows the magnetically split energy levels of  $^{57}\text{Fe}$ . Figure 2.15 presents a typical magnetic spectrum of  $\alpha$ -Fe foil that is used as the calibration sample. The magnitude of the field determines the energy splitting for the  $\alpha$ -Fe 330 kOE.  $\Delta E_m(g)$  and  $\Delta E_m(e)$  refer to the energy differences between the magnetic substates of the ground and the excited state, respectively. In addition, by applying an external magnetic field to a magnetic substance and measuring the change in the hyperfine magnetic field as a function of the applied field, the magnetism of the substance can be classified.

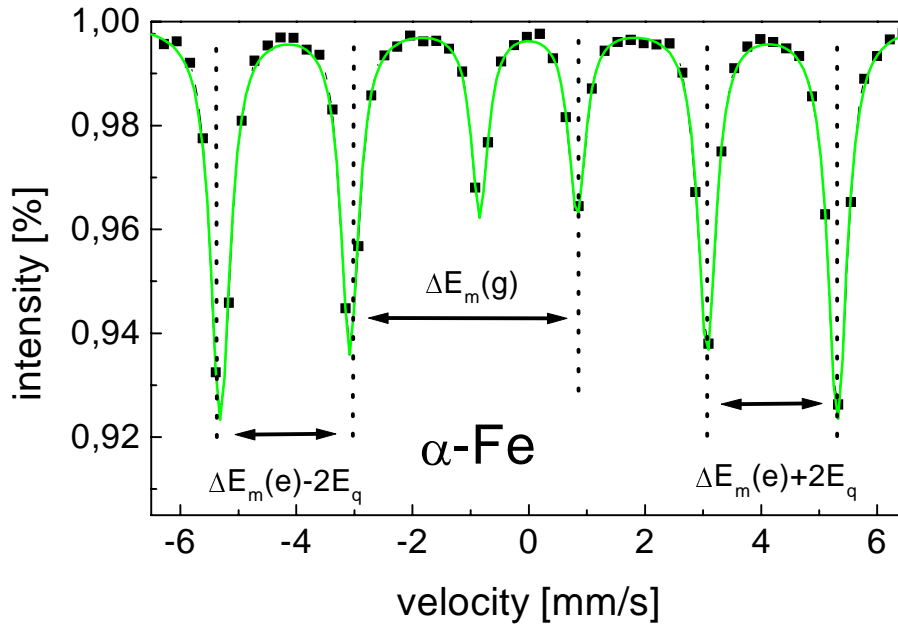


Figure 2.15: Magnetic six line splitting of  $\alpha$ -Fe.

### Calculating the nitrogen concentration

When the relative fractions of different subspectra (i.e. singlet, quadrupole doublet, sextet) and the phase composition are known, the nitrogen content of the sample can be obtained. However, that requires the information about the crystalline structure, the coordination of Fe atoms in the lattice. To which lattice sites do the subspectra correspond? The FeN phase (see Figure 2.14) is a mixture of two cubic structures, NaCl- and ZnS-type, respectively. The single line S1 belongs to the ZnS-structure, where the iron atom is surrounded by 4 nearest neighboring nitrogen atoms [11]. Since the CEM spectrum exhibits only one subspectrum, the singlet, corresponding to ZnS-type FeN, the nitrogen content of this phase is 50 at.%, i.e. all the nitrogen sites are occupied. The single line S2 and the quadrupole doublet are related to NaCl-type FeN. The S2 singlet is due to iron atoms with fully occupied nitrogen nearest neighboring sites. The quadrupole doublet is assumed to result from vacancies at nitrogen sites. In the NaCl-structure the iron atom is associated with six nearest neighboring sites. The binomial distribution can be used in calculating the probability  $p_n(x)$  for an iron atom to have  $n$  of those sites occupied by a nitrogen atom

$$p_n(x) = \binom{6}{n} \cdot (x)^n \cdot (1-x)^{6-n} \quad (2.38)$$

for  $n = 0 - 6$

The probability corresponds to the relative areas of the subspectra in CEM spectrum

$$p_n(x) = \frac{A(S1)}{A(S2) + A(D)} \quad (2.39)$$

where  $A(S1)$ ,  $A(S2)$  and  $A(D)$  are the relative areas of the subspectra, respectively, so that  $A(S1) + A(S2) + A(D) = 100\%$ . Thus the nitrogen concentration in NaCl-type  $\text{FeN}_{1-x}$  is given by

$$c_N(\text{NaCl}) = \frac{1-x}{2-x} \quad (2.40)$$

with

$$x = 1 - \sqrt[6]{\frac{A(S2)}{A(S2) + A(D)}} \quad (2.41)$$

The total nitrogen concentration in both NaCl- and ZnS-type FeN is calculated by

$$C_N^{total} = \frac{A(S1)}{100} \cdot c_N(ZnS) + \frac{(1 - A(S1))}{100} \cdot c_N(NaCl) \quad (2.42)$$

### CEMS measurement setup

The Mössbauer setup used in the present work is schematically illustrated in Figure 2.16. The measurement system consists of a constant acceleration spectrometer operating in connection with a multi-channel scaler with 1024 channels. The  $^{57}\text{Co/Rh}$  source with an activity of about 500 MBq was kept at room temperature. The conversion electrons (energies given in Figure 2.12) were detected by means of a He/CH<sub>4</sub> gas flow proportional counter. The velocity and the isomer shift were calibrated relative to a 25 μm thick α-Fe foil. The CEMS spectra were analyzed by a least-square fitting routine by superimposing Lorentzian lines [31,32]. The analyzing program accomplished the calculation of the hyperfine parameters (isomer shift, quadrupole splitting, magnetic hyperfine field, line width, intensity of lines as well as relative line intensities of magnetic split spectrum) and the relative areas of the subspectra.

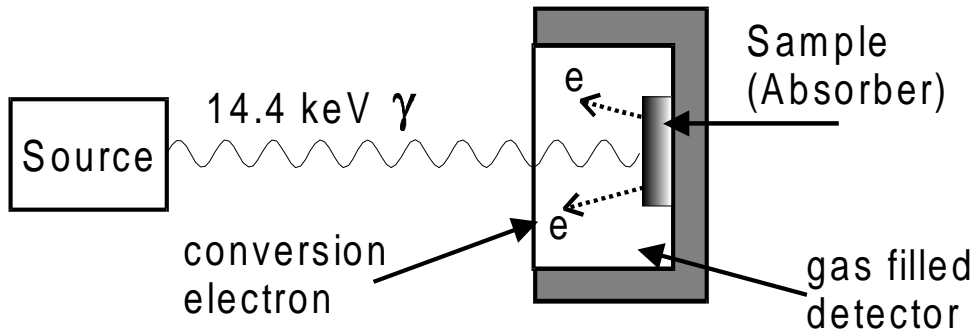


Figure 2.16: CEMS measurement setup.

### 2.2.5 X-Ray Diffraction

In order to characterize the crystalline phases, lattice constants and the possible texture in the films, they were analyzed by the X-Ray Diffraction (XRD). For a known structure, the diffraction pattern can be calculated exactly. The sharpness and shape of the diffraction peaks determine the perfection of crystal. For crystals containing defects, the peaks are broadened. Diffraction occurs as waves interact with a regular structure whose repeat distance is about the same as the wavelength. The theory of X-Ray Diffraction is explained comprehensively in the literature [33]. The Bragg's law

$$n\lambda = 2d \sin \theta \quad (2.43)$$

where n is an integer n=1,2,3,... (n=1 in calculations made in this work), gives the relationship between the wavelength λ, the interatomic spacing d and the diffraction angle θ.

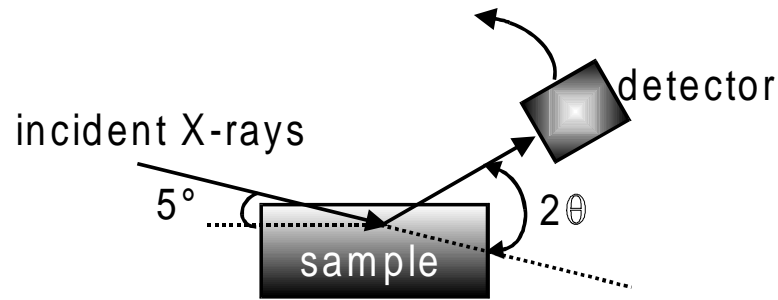


Figure 2.17: X-ray diffraction measurement arrangement.

For the measurements in the present work a diffractometer type D8 Advance from Bruker AXS using the  $\text{Cu-K}\alpha$  radiation was utilized. The XRD setup is presented in Figure 2.17. The wavelength of the X-rays is 1.5406 Å and the energy 8.33 keV. A Si(Li) semiconductor detector with high energy resolution was used to detect the radiation. The diffraction patterns of the X-ray intensity were recorded as a function of 2-theta angle keeping the incident angle of the X-rays fixed at 5 degree. The diffractometer system is equipped with a diagnosis program, which provides the position of the diffraction peaks and a wide reference database.

Figure 2.18 displays a typical diffraction pattern of a 100 nm thick  $\text{Ni}_3\text{N}$  film on a silicon substrate.  $\text{Ni}_3\text{N}$  has a hexagonal crystal structure where the interstitial lattice sites are partially occupied by nitrogen atoms. From the identification of the reflection peaks the lattice constants can be determined using the following equation for the d-value in a hexagonal structure

$$d_{hkl} = \frac{a}{\sqrt{\frac{4}{3}(h^2 + hk + k^2) + \left(\frac{la}{c}\right)^2}} \quad (2.44)$$

where  $a$  and  $c$  are the lattice constants, and  $h$ ,  $k$  and  $l$  the Miller indexes. Using equation (2.44) the lattice constants in  $\text{Ni}_3\text{N}$  structure become  $a = 0.268(5)$  nm and  $c = 0.427(5)$  nm, respectively. The values agree very well with the ones found in literature,  $a = 0.266$  nm and  $c = 0.428$  nm [34]. The thin nickel nitride film has a preferred orientation along the  $\text{Ni}_3\text{N}(101)$ -plane.

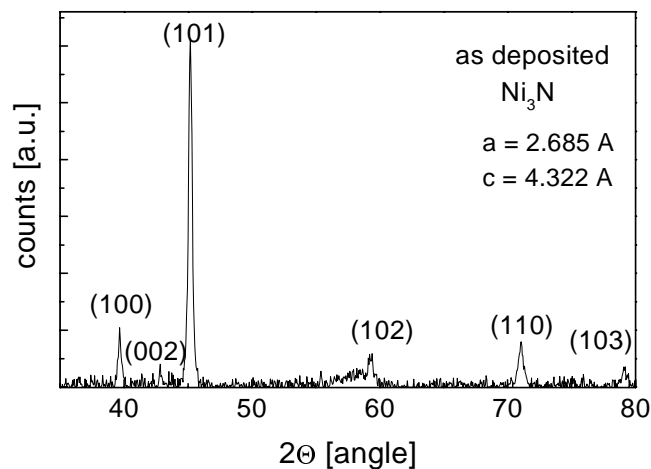


Figure 2.18: X-ray diffraction pattern of magnetron sputtered  $\text{Ni}_3\text{N}$  thin film.

### 2.2.6 Transmission electron microscopy

Transmission electron microscopy (TEM) provides access to the microstructure down to molecular dimensions. A variety of different signals can be used for image formation, among these transmitted and diffracted electrons as well as characteristic X-rays, allowing for a unique information combination concerning shape, distribution, crystallography and chemistry of microstructural detail. TEM applications deal essentially with two domains of microstructure, namely with the statics and dynamics of crystal defects (dislocations, stacking faults, intercrystalline boundaries) and with the constitution of alloys (small particles of precipitated phases, phase stability/instability). In TEM a beam of highly focused electrons is directed toward a thinned sample and depending on the positioning of the aperture slits the TEM imaging is divided in three categories. In the bright-field image the diffracted electron beam is blocked by the aperture and only the incident beam is let through on the photoplate. On the contrary, in the dark-field image the incident beam is deflected so that the diffracted electrons hit the photoplate. In the both cases a purely amplitude contrast image is obtained. Electron diffraction for phase evaluation utilizes the incident beam along with some of the diffracted electrons. By means of the excellent resolution ( $\approx 0.2$  nm) the electron diffraction enables the detection of much smaller crystallites than XRD. The strong interaction of electrons with the nuclei increases the intensity of the reflections. On the other hand the penetration depth of the electrons in the sample is limited and therefore only relatively thin ( $< 30$  nm) samples can be analyzed. The films are either deposited on special substrates or thick samples are thinned, e.g. by mechanically polishing or by ion milling.

The electrons with small wavelengths ( $\lambda=3.3489$  pm at 120 kV) accelerated with tens of kV are diffracted to small angles. With the following approximation for the small angles

$$\tan \theta \cong \frac{R \cdot L}{2} \cong \sin \theta \quad (2.45)$$

the equation for the electron diffraction from the Bragg's law becomes

$$\lambda L = R d \quad (2.46)$$

where  $\theta$  is the angle between the incident electron beam and the reflection plane,  $R$  is the distance between the incident beam direction to the diffracted beam to the photoplate,  $\lambda$  is the electron wavelength and  $L$  the distance between the sample and the photoplate.

The thin iron nitride films for TEM were deposited on 300 mesh Cu grids covered by 15  $\mu\text{m}$  thick carbon film. The layer thickness was kept  $< 30$  nm. The TEM analyses were carried out employing the analytical electron microscope, type Philips EM400 T, at an acceleration voltage of 120 kV. In Figure 2.19 a bright-field image of FeN is presented. The film consists of crystalline grains with the average diameter of 30 nm within amorphous FeN.

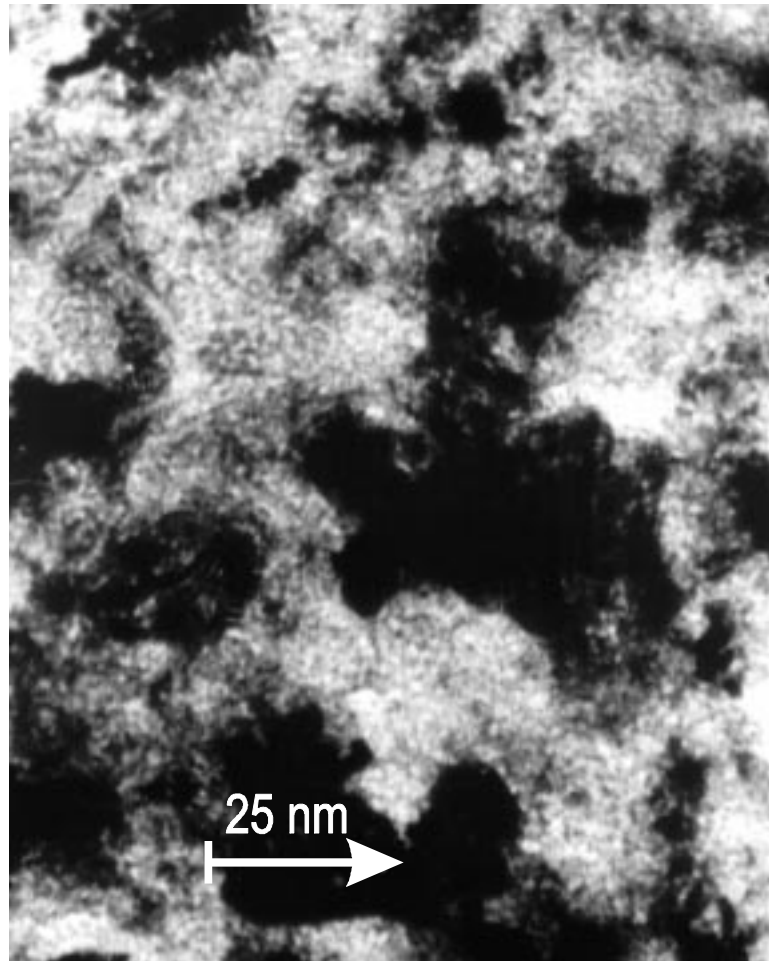


Figure 2.19: A TEM image of a FeN thin film prepared at 523 K.

### 2.2.7 Atomic Force Microscopy

The 3-dimensional surface topography of the thin films was obtained by Atomic Force Microscopy. The main interest was to find out the mean roughness of the samples and the average size of the grains. AFM scans the sample with a sharp tip mounted on a cantilever spring, usually made of silicon, silicon oxide or silicon nitride. The electron cloud of the tip presses against the clouds of individual atoms in the sample, generating a repulsive force that varies with the surface relief. The force deflects the tip, whose movements are monitored by a laser beam reflected from the top of the cantilever to a photodiode sensor. A feedback mechanism responds to the changes in the beam's path by activating a piezoelectric control, which adjusts the sample's height so that the deflection of the arm remains constant. The sample's movements are translated into a surface profile. One of the most important factors influencing the resolution, which may be achieved with an AFM, is the sharpness of the scanning tip. Typical lateral resolution is of the order of 5 nm and the vertical  $\sim 0.2$  nm. The AFM setup is presented in Figure 2.20.

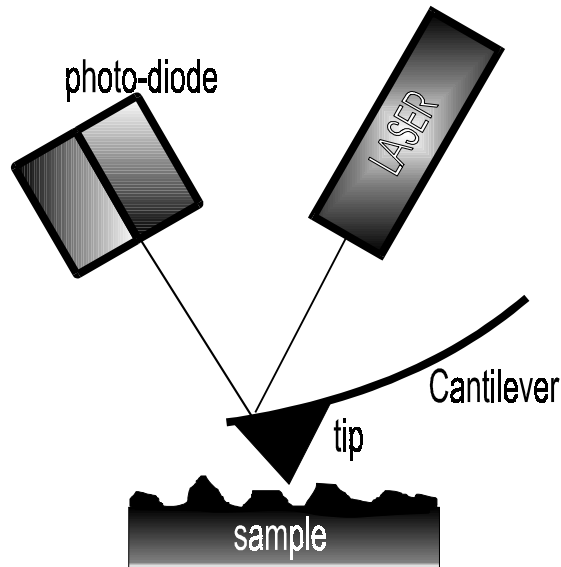


Figure 2.20: Schematic diagram of the AFM measurement setup.

The AFM can be operated in two principal modes with feedback control or without feedback control. If the electronic feedback is switched on, then the positioning piezo which is moving the sample (or tip) up and down can respond to any changes in force which are detected, and alter the tip-sample separation to restore the force to a pre-determined value. This mode of operation is known as constant force mode. If the feedback electronics are switched off, then the microscope is said to be operating in constant height or deflection mode. The image contrast depends on the tip-sample interaction and can be divided in three main classes: contact mode, tapping mode and non-contact mode. In contact mode the tip and sample remain in close contact as the scanning proceeds. In tapping mode the cantilever is oscillated at its resonant frequency (often hundreds of kilohertz) and positioned above the surface so that it only taps the surface for a very small fraction of its oscillation period. The short contact time means that lateral forces are dramatically reduced as the tip scans over the surface. The tapping mode gives possibility to phase imaging. This works by measuring the phase difference between the oscillations of the cantilever driving piezo and the detected oscillations. It is thought that image contrast is derived from image properties such as stiffness and viscoelasticity. In the non-contact mode the cantilever must be oscillated above the surface of the sample at such a distance that we are no longer in the repulsive regime of the intermolecular force curve.

The atomic force microscope, type Digital Instruments Multimode<sup>TM</sup> Nanoscope, was used in the tapping mode with the oscillation frequency of about 250 kHz. Figure 2.21 shows an AFM image of a Ni<sub>3</sub>N sample irradiated with 100 keV Xe<sup>+</sup> ions with a fluence of  $1 \times 10^{16}$  ions/cm<sup>2</sup> at 80 K. The  $3.3 \times 3.3 \mu\text{m}^2$  image reveals that the nitride film consists of relatively large grains of  $\sim 450$  nm diameter. The rms roughness obtained from the measurement is about 4 nm.

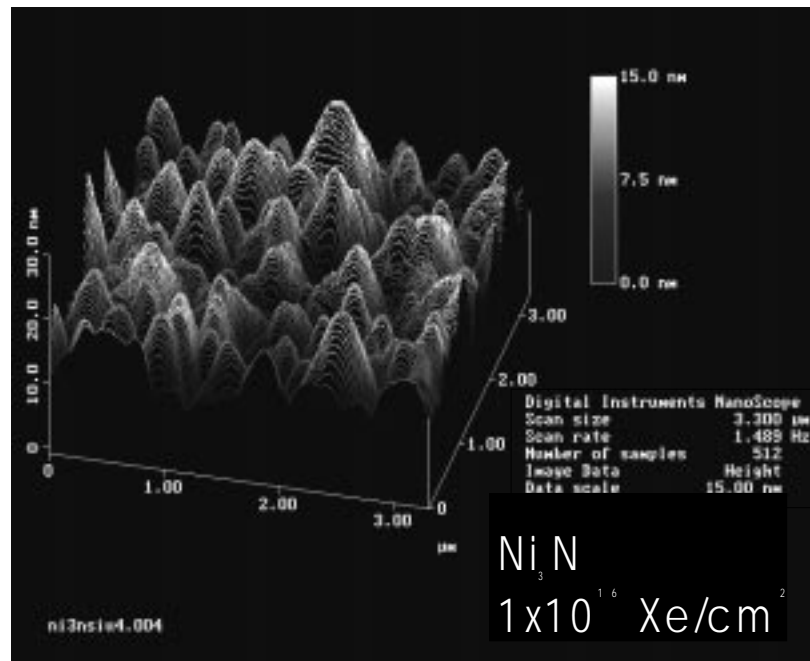


Figure 2.21: AFM image of the surface topography of a Xe irradiated  $\text{Ni}_3\text{N}$  sample.

### 3 Production of magnetron sputtered FeN and Ni<sub>3</sub>N thin films

The first chapter gives an overview about the Fe-N and Ni-N phase diagrams emphasizing on FeN and Ni<sub>3</sub>N structures. The following chapters present the systematic investigations of the influence of deposition parameters on thin nitride film properties in reactive magnetron sputtering. In every chapter the effect of one deposition parameter, such as gas mixture and pressure, substrate temperature, substrate bias voltage and RF power, is discussed by collecting the results obtained from various analyzing methods. In the chapter 3.6 the thermal stability of the nitride films, monitored by annealing in different atmospheres, is investigated. The chapters are divided into two parts, the larger and more detailed part presents the results concerning the production of FeN layers and the other part is dedicated to Ni<sub>3</sub>N.

#### 3.1 Fe-N and Ni-N phase diagrams

##### FeN

Iron nitrides, as well as other transition metal nitrides, are compounds of great scientific interest because of their properties making them useful in many applications, e.g. as protective coatings, diffusion barriers etc. The iron-nitrogen phase diagram consists of several interstitial solutions ( $\alpha$ ,  $\gamma$ ,  $\epsilon$ ), chemical compounds ( $\gamma'$ -Fe<sub>4</sub>N,  $\zeta$ -Fe<sub>2</sub>N) and metastable phases ( $\alpha'$ -martensite,  $\alpha''$ -Fe<sub>16</sub>N<sub>2</sub>) [35,36]. The Fe-N phase diagram at atmospheric pressure is presented in Figure 3.1, where the high temperature region exceeding 1200 K has been extended by calculations [37].

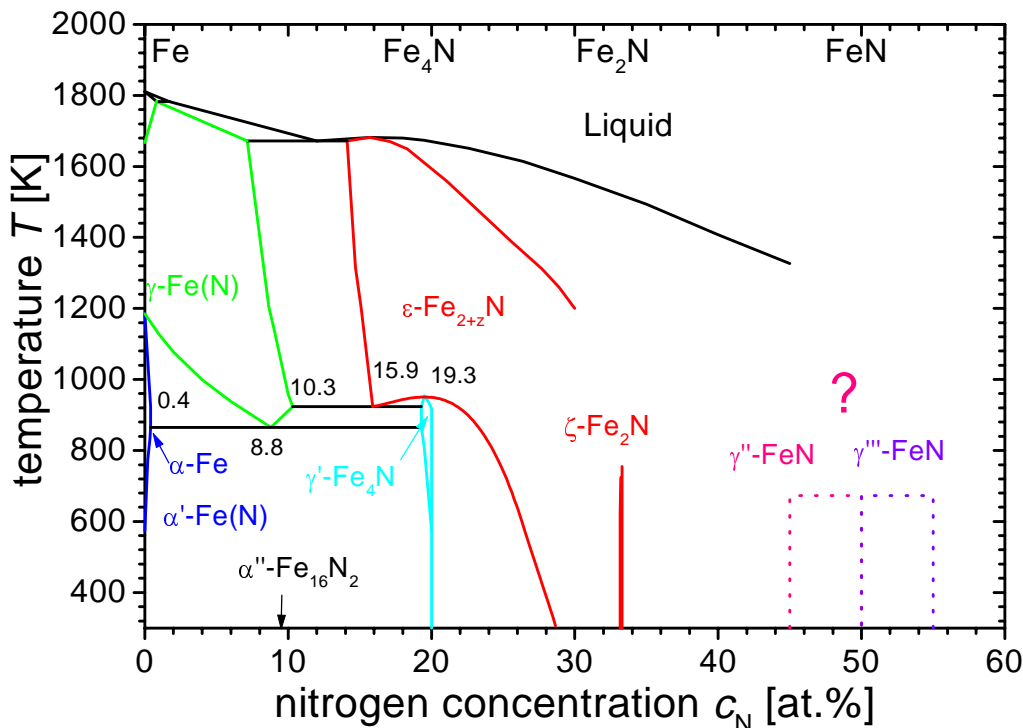


Figure 3.1: Fe-N phase diagram [36,37].

The  $\epsilon$ -phase, covering the nitrogen concentration range from 15 to 33 at.%, and the  $\gamma'$ -phase, a nearly stoichiometric line compound, are used as hard coatings, because of their good tribological and corrosion-resistance properties. The  $\alpha''$ - $\text{Fe}_{16}\text{N}_2$  has attracted interest due to its giant magnetic moment [38]. In contrast to the nitrogen-poor side, phases at the nitrogen-rich side are less known. Some years ago the new compound FeN was successfully prepared by reactive magnetron sputtering [39]. FeN was found to have an intermixed structure of two phases, of NaCl - and ZnS-type structures. Due to its cubic symmetry, the phase named  $\gamma'''$ - and  $\gamma''$ -FeN, respectively. FeN with  $y \leq 0.5$  show metallic behavior in the temperature dependence of the electric resistivity [40]. At room temperature both  $\gamma'''$ - and  $\gamma''$ -FeN are paramagnets. At 4.2 K  $\gamma''$ -FeN transforms to a nonmagnet, while  $\gamma'''$ -FeN shows two magnetic sextets at 10 K corresponding to two kinds of Fe atoms in NaCl-type nitride. Measurements revealed that  $\gamma'''$ -FeN is then an antiferromagnet. Several publications have reported the properties of this new phase [8,10,41], but despite of the great interest in extending the Fe-N phase diagram and finding out the properties of the new compound the final structure and the stability region still remained unclear. The main motivation in producing FeN films in this work was to obtain the lacking information and complete the phase diagram in this new regime.

### Ni<sub>3</sub>N

X-ray and electron diffraction studies have yielded a fairly complete picture of the possible nickel nitride lattice structures. The equilibrium solid phases of the Ni-N system are the fcc terminal solid solution Ni, the fcc nitride,  $(\text{Ni}_4\text{N})_I$  [42], its facecentered tetragonal modification  $(\text{Ni}_4\text{N})_{II}$ , and the hcp nickel nitride,  $\text{Ni}_3\text{N}$ . In addition, nickel azide,  $\text{NiN}_6$ , may be an equilibrium phase and other nitrides like  $\text{Ni}_2\text{N}$  and  $\text{Ni}_3\text{N}_2$  have been reported [34]. The Ni-N phase diagram is plotted in Fig.3.2. The concentration of nitrogen in nickel equilibrated with nitride has not yet been determined reliably at every temperature. The fugativity of molecular nitrogen at which these phases coexist is also undetermined. At temperatures above about 873 K, it has not been possible to maintain nitrogen fugacities in the presence of Ni large enough to stabilize a nitride. Nickel nitride can therefore said to be a relatively weakly bound nitride. The  $\text{Ni}_3\text{N}$  phase is stable only up to a temperature of about 523 K and the nitrogen is soluble between 20 and 25 at.%.

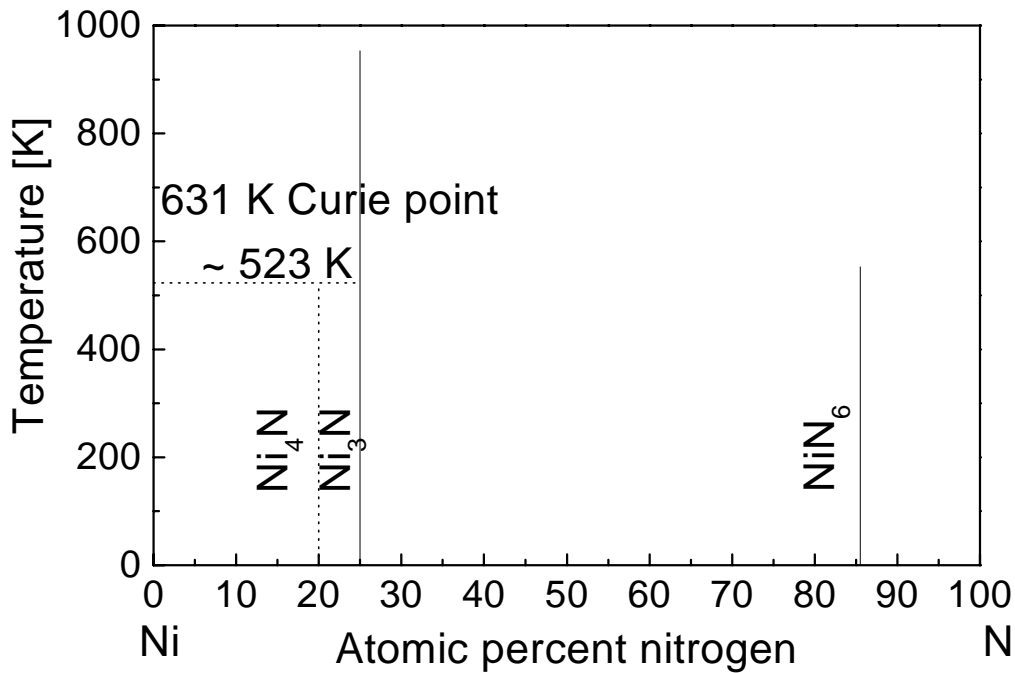


Figure 3.2: Ni-N phase diagram.

### 3.2 Gas mixture and pressure

The gas mixture and pressure are among the most important deposition parameters. Many properties of thin films like stress and optical reflectance are found to depend on the sputtering pressure [43]. In reactive sputtering the composition and the phase structure of the sample are greatly influenced by the partial pressures of the reactive and the inert gas. In order to find the optimal gas flows in producing FeN and Ni<sub>3</sub>N phases, both gas flows, Ar and N<sub>2</sub>, were varied systematically while keeping the other deposition parameters fixed.

#### FeN

One set of FeN films was prepared at room temperature, keeping the N<sub>2</sub>-flow constant at the maximum flow of 30 sccm and varying the Ar-flow from 15 to 30 sccm. The target-substrate distance and the RF power were 8 cm and 110 W, respectively. Since CEMS accurately detects the amount of different phases present in the sample, it was used as a determining method in finding the optimum gas flows. In Figure 3.3a a typical CEM spectrum of a FeN sample, deposited at 293 K with 30 sccm N<sub>2</sub>- and 27 sccm Ar-flows, is shown. The spectrum was deconvoluted into two single lines (S1, S2) and a quadrupole-split doublet (D). The two singlets were fitted corresponding to Fe<sup>3+</sup> cations in the ZnS-structure,  $\gamma''$ -FeN, and Fe<sup>2+</sup> cations in the NaCl-structure,  $\gamma'''$ -FeN, all having the nearest nitrogen neighbor sites occupied. These results are not sufficient to clarify the origin of the doublet and it will be discussed later in the bias voltage chapter. The hyperfine parameters of the subspectra are listed in Table 2. In Figure 3.4a the relative fractions of the CEM subspectra are plotted as a function of the Ar-flow. The pure FeN-phase is suggested to consist of the single line S1 [10]. Therefore the S1 component was used as an indicator of the cubic FeN phase.

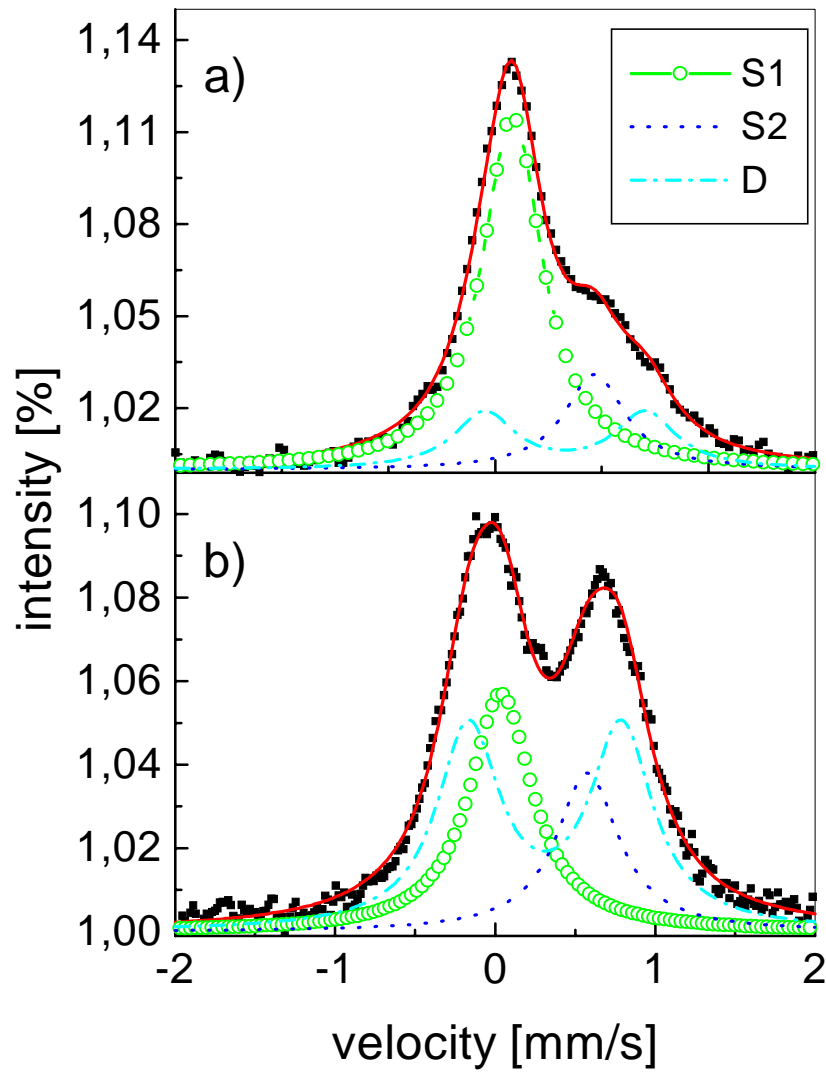


Figure 3.3: CEM spectrum of a FeN film deposited at room temperature with a) 27 sccm Ar- and 30 sccm N<sub>2</sub>-flow and b) 27 sccm Ar- and N<sub>2</sub>-flow.

Table 2. Hyperfine parameters of FeN.

Subspectra	$\delta$ [mm/s]	QS [mm/s]
S1	0.09(3)	
S2	0.48(5)	
D	0.32(2)	0.77(11)

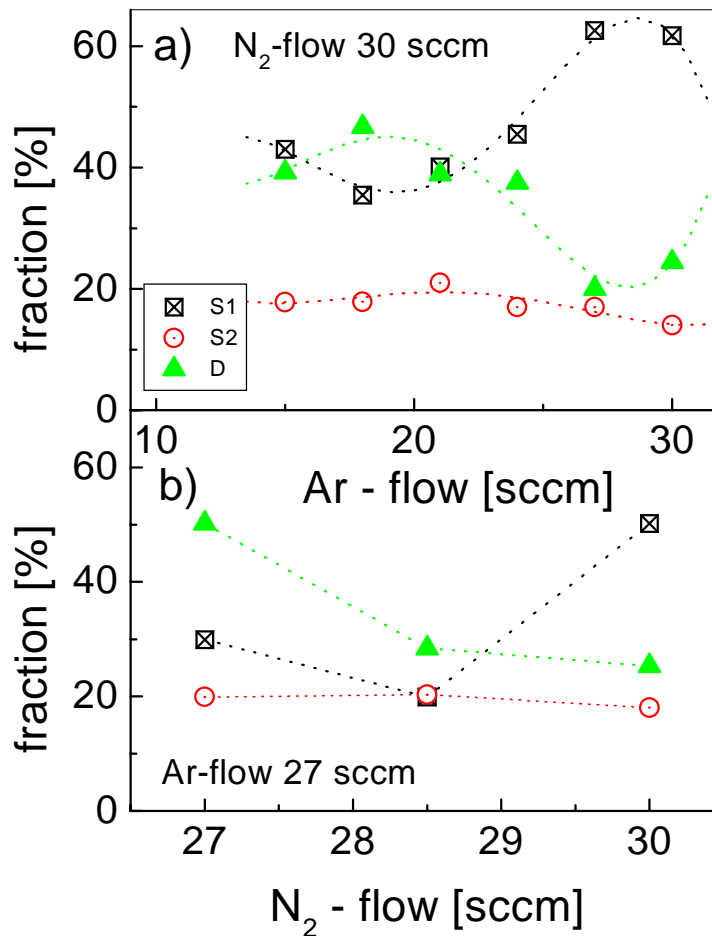


Figure 3.4: The fractions of the CEM subspectra as a function of a)  $N_2$ - and b) Ar-flows. The errors are smaller than the symbols.

It can be seen that a change in the Ar-gas flow does not linearly affect the fractions of the subspectra, but maxima and minima can be found at certain flow-rates. The largest relative fraction of the S1 line was achieved with an Ar-flow of 27 sccm. This set of samples was also measured by RBS. The iron content of the films is plotted as a function of the Ar-flow in Figure 3.5a. The increasing Ar-flow reduces the Fe-concentration, which is caused by the increasing ionization in the plasma. The Fe concentration at the optimum gas flow is not 50 at.%, which would be expected for the pure FeN phase. RBS detects, in principle, all the elements, but the mass resolution is limited and the detection efficiency for low-Z elements rather poor. In particular, RBS cannot differentiate between light elements, such as N and O.

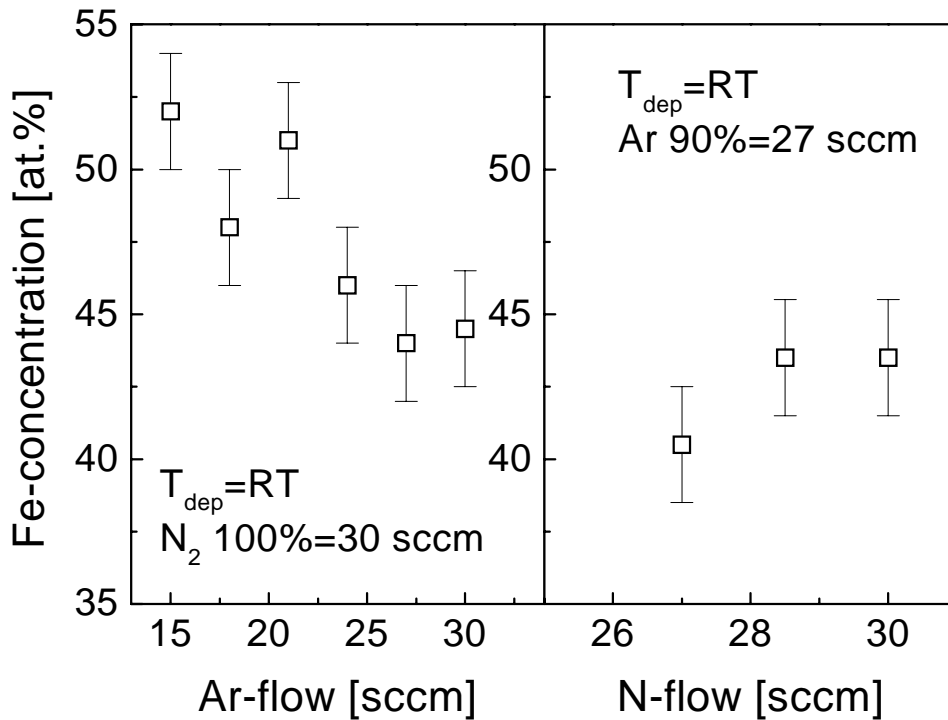


Figure 3.5: Fe contents determined by RBS as function of Ar- and  $N_2$ -flows.

In another series the Ar-flow was fixed to 27 sccm while the  $N_2$ -flow was slightly varied. In Figure 3.3b the CEM spectrum of a sample deposited at 293 K with 27 sccm Ar- and  $N_2$ -flows is plotted. A slight variation in the  $N_2$ -flow remarkably increases the fraction of the doublet and at the same time decreases the amount of both single lines. When the fractions of the subspectra are plotted over the  $N_2$ -flow (see Figure 3.4b), the optimum  $N_2$ -flow, which exhibits the largest relative amount of S1, was found to be 30 sccm.

### $Ni_3N$

Gas flow variation depositions were also carried out for the production of  $Ni_3N$  films. Since the magnetic properties of Fe and Ni targets are quite similar, the FeN deposition series were used as a guideline in choosing the optimum gas flows for the deposition of  $Ni_3N$ . The stoichiometry closest to  $Ni_3N$  (determined by RBS and RNRA) was achieved with an Ar-flow of 27 sccm and a  $N_2$ -flow of 12 sccm. However, the analysis showed always an excess of nitrogen in the films.

### 3.3 Substrate temperature

The second step in tuning the deposition parameters was to vary the substrate temperature, which especially affects the crystalline structure and the possible epitaxial growth of the films. Generally high temperatures and low deposition rates lead to well crystallized structures and to the thermodynamically most stable orientation. Another intention in increasing the temperature was to accomplish the out-diffusion of extra nitrogen and possible impurities (O,H) already during the film growth.

## FeN

Both the N<sub>2</sub>- and Ar-flow were fixed at their optimum values (N<sub>2</sub> 30 sccm, Ar 27 sccm) when producing the FeN films at elevated temperatures. The substrate temperature was varied from room temperature up to 820 K. In order to improve the crystalline structure, to maximize the fraction of the S1 line in the CEM spectrum and to determine the deposition temperature up to which the phase structure remains stable. Figure 3.6 show RBS spectra of samples deposited at 293 K and 523 K, respectively. The homogeneity of the film improves with increasing substrate temperature. The interface between the FeN film and the silicon substrate seems less broad than after room temperature deposition. The diffusivity of ad-atoms on the substrate is dependent on the temperature. Especially critical is the growth of the first atomic layers. Obviously the elevated substrate temperature seems to favor the formation of FeN compound over the diffusion of Fe or N into silicon.

Figure 3.7 illustrates TOF-ERDA concentration profiles of three samples deposited at room temperature, 388 K and 523 K. The fractions of both Fe and N increase with increasing temperature, while the concentrations of the other impurity elements C and O detected in the films decrease. The required 1:1 ratio of Fe to N was achieved at 523 K, although still some impurities remained in the sample.

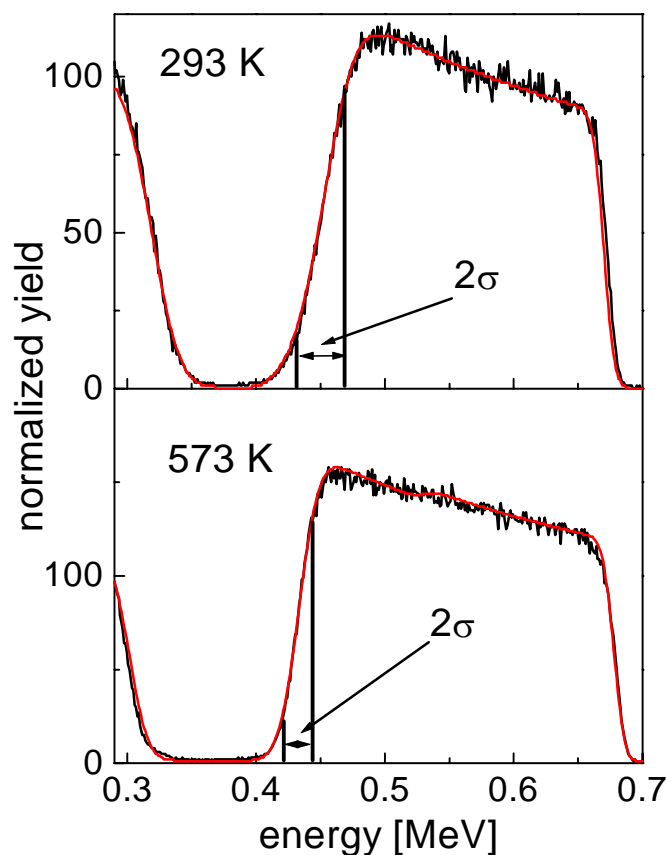


Figure 3.6: RBS spectra of FeN samples produced with 27 sccm Ar- and 30 sccm N<sub>2</sub>-flows a) at room temperature and b) at 573 K.

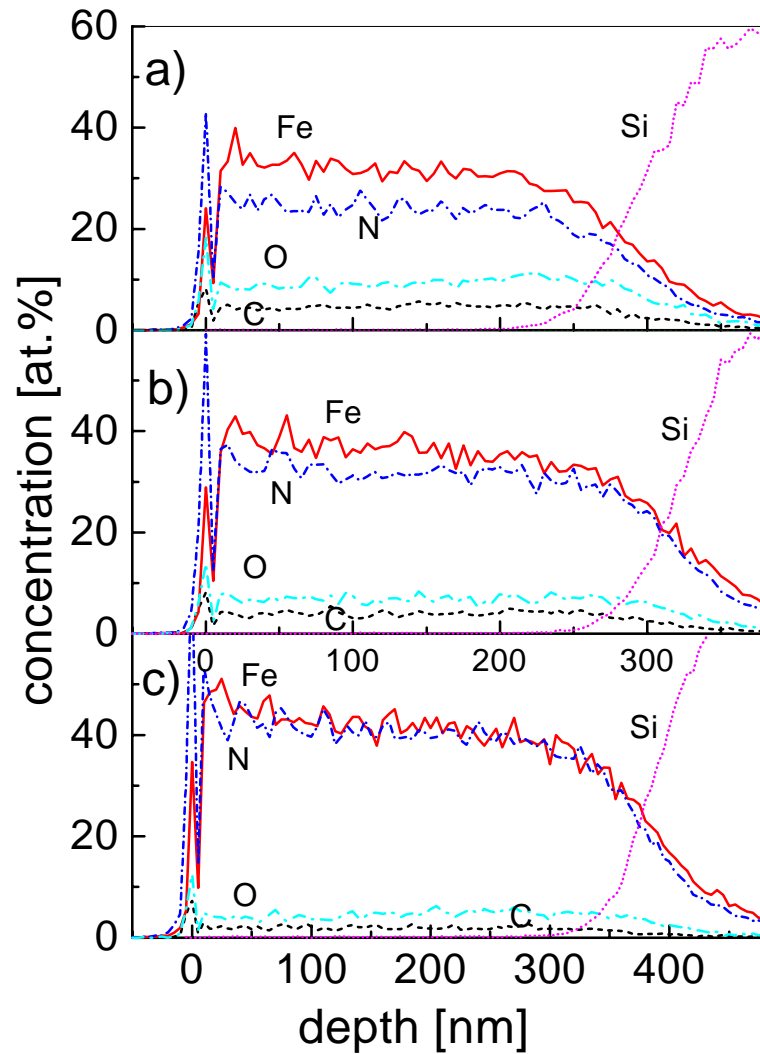


Figure 3.7: TOF-ERDA elemental profiles of samples deposited at different temperatures: a) 293 K, b) 388 K and c) 523 K. Gas flows were the same at every temperature: Ar 27 sccm and  $N_2$  30 sccm.

Higher deposition temperatures increase the relative amount of the S1 signal in the CEM spectrum. The maximum amount was found at a temperature of about 523 K. The CEM spectrum of the corresponding sample is presented in Figure 3.8a. In Figure 3.9 the Fe-concentrations (determined by RBS and RNRA) of the samples are plotted as a function of the deposition temperature. Above 615 K, the structure of the FeN films suddenly changed to the  $\epsilon$ -phase, which is indicated by an increase of the Fe-content. The phase transition can clearly be seen in the CEM spectra. At 615 K (Figure 3.8b), no indications of the  $\gamma$ -phases are present. The two quadrupole doublets were identified to belong to the  $\epsilon$ -phase.

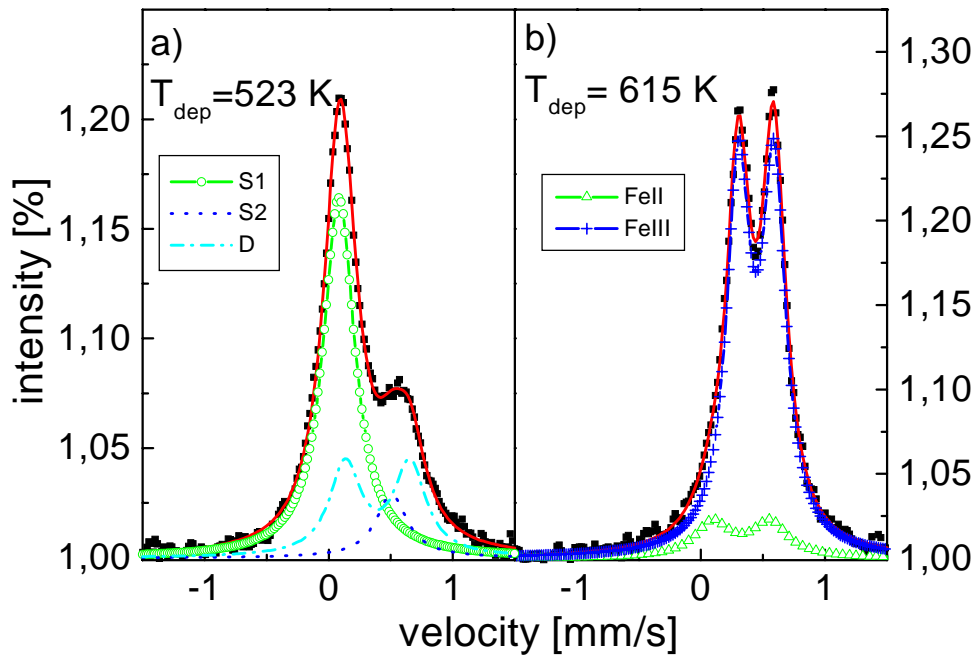


Figure 3.8: CEM spectra of two FeN samples prepared a) at 523 K and b) at 615 K temperatures.

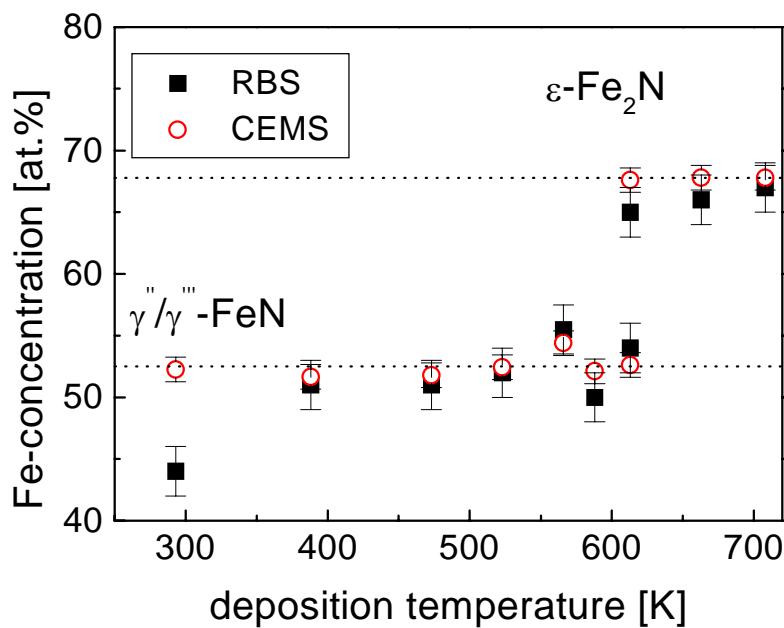


Figure 3.9: Fe concentrations of FeN films over a wide range of deposition temperatures.

The line widths of the CEM spectra decrease with increasing deposition temperature (see Figure 3.10). This can be correlated with the improving crystallinity of the structure, e.g. decreasing number of defects in the structure.

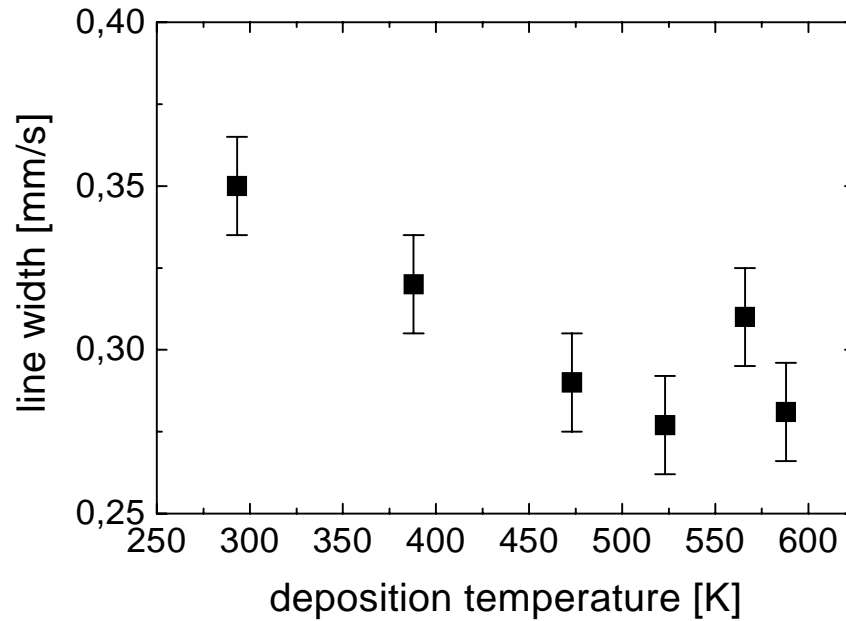


Figure 3.10: CEMS line width as function of the deposition temperature.

The XRD and TEM patterns of the FeN films could be indexed belonging to two fcc structures with lattice parameters of  $a = 0.452(4)$  nm ( $\gamma'''$ -phase) and  $a = 0.435(5)$  nm ( $\gamma''$ -phase). Samples produced at room temperature exhibited broad XRD peaks (Figure 3.11a). The deposition temperatures have to be above room temperature to achieve well-crystallized structures (Figure 3.11b). All the samples had the preferred orientation of FeN(111). The relative intensity of the FeN(220) plane increased with increasing N-concentration, while the intensities of the FeN(111), FeN(200) and FeN(311) planes decreased. At higher substrate temperatures the growing film may reorient to adopt the thermodynamically most stable orientation. The bright field TEM images of the FeN layer deposited at 523 K showed that it consists of crystalline grains with an average size of 30 nm surrounded by amorphous FeN (Figure 3.12). The distance between the grains was of about the same order. In the diffraction pattern, the FeN(111) Debye-Scherrer ring confirmed most clearly the texture determined by XRD. Also the lattice constants were within the error equal to the ones measured by XRD.

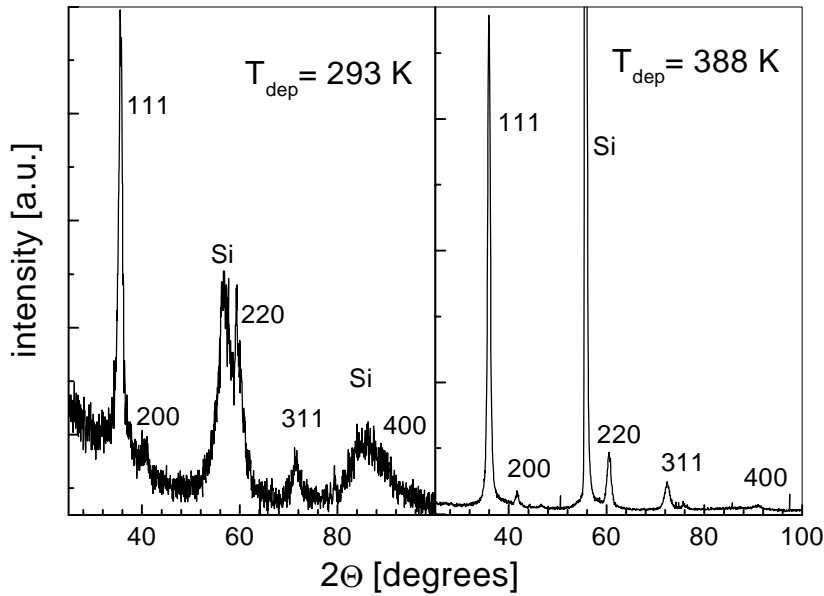


Figure 3.11: XRD patterns of FeN films prepared at room temperature and at 388 K.

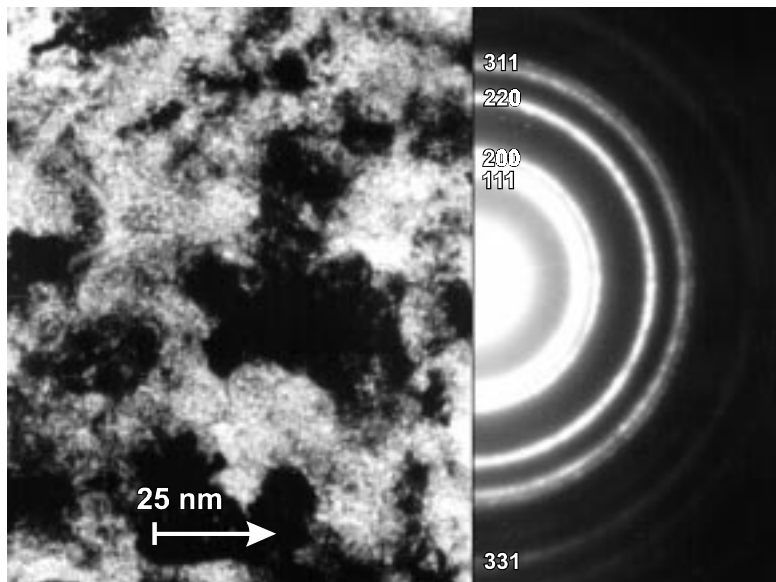


Figure 3.12: A TEM image and a SAD pattern of a FeN sample prepared at 523 K.

### Ni<sub>3</sub>N

The variation of the N<sub>2</sub> partial pressure in the chamber was not sufficient to produce Ni<sub>3</sub>N with the correct stoichiometry at room temperature. As mentioned in the latter chapter the RBS and RNRA analysis showed an excess of nitrogen. The XRD spectra exhibited peaks belonging to the Ni<sub>3</sub>N phase, which indicated that the excess nitrogen was located at interstitial sites and/or at grain boundaries. The Ni<sub>3</sub>N phase is thermally stable only up to a temperature of 523 K. To assure that the Ni<sub>3</sub>N structure does not start to dissociate during the deposition, but only the diffusion of nitrogen from the surface during film growth is enhanced, the substrate temperature was elevated only up to about 370 K. The analysis of the films revealed that this temperature was not enough to achieve the desired stoichiometry, though. The influence of other deposition parameters still needed to be tested.

## 3.4 Substrate bias voltage

### FeN

Keeping all the other production parameters constant (Ar-flow 27 sccm, N-flow 30 sccm, temperature 573 K, target-substrate distance 8 cm, RF power 110 W) a DC bias voltage between -20 V and +20 V was applied to the substrate while depositing the FeN films. At 0 V bias voltage, there was a possibility to either keep the substrate holder isolated or connected to the sputtering chamber. RNRA and RBS analysis showed that the most homogeneous layers were produced with zero bias voltage. With both negative and positive bias voltages the deeper part of the layer has a lower Fe-concentration than the surface. In all the cases the film growth rate was very low and therefore the thickness did not exceed 160 nm, even after 6 hours of deposition. Only in the cases where no bias voltage was applied, the N-content of the samples was close to 50 at.%. TOF-ERDA analyses revealed that these films contained, in addition to Fe and N, impurities of O, C and H. Figure 3.13 compares TOF-ERDA and CEM spectra obtained at different bias voltages. The relative fractions in the CEM subspectra vary strongly with the bias voltage. The composition of the films, especially with regard to the impurities, could also be correlated with the bias voltage. Particles having an opposite charge to the substrate holder can be attracted by the bias voltage. Especially in cases where the voltage was +20 V and -20 V, the amount of these contaminants grew large (~20 at.%). The fractions of the two singlets and the doublet are plotted as a function of the bias voltage in Figure 3.14. It is obvious that the maximum fractions of S1 and S2 are achieved when no bias voltage is applied. In the case of the +20 V bias, the substrate was SiO<sub>2</sub>, which explains the rising O concentration in the film substrate boundary. The sample prepared with -20 V voltage was further analyzed by XRD. The diffraction spectrum shows a very strong texture along the FeN(111) direction. The lattice parameter is surprisingly large,  $a = 0.470$  nm, indicating the  $\gamma'''$ -phase.

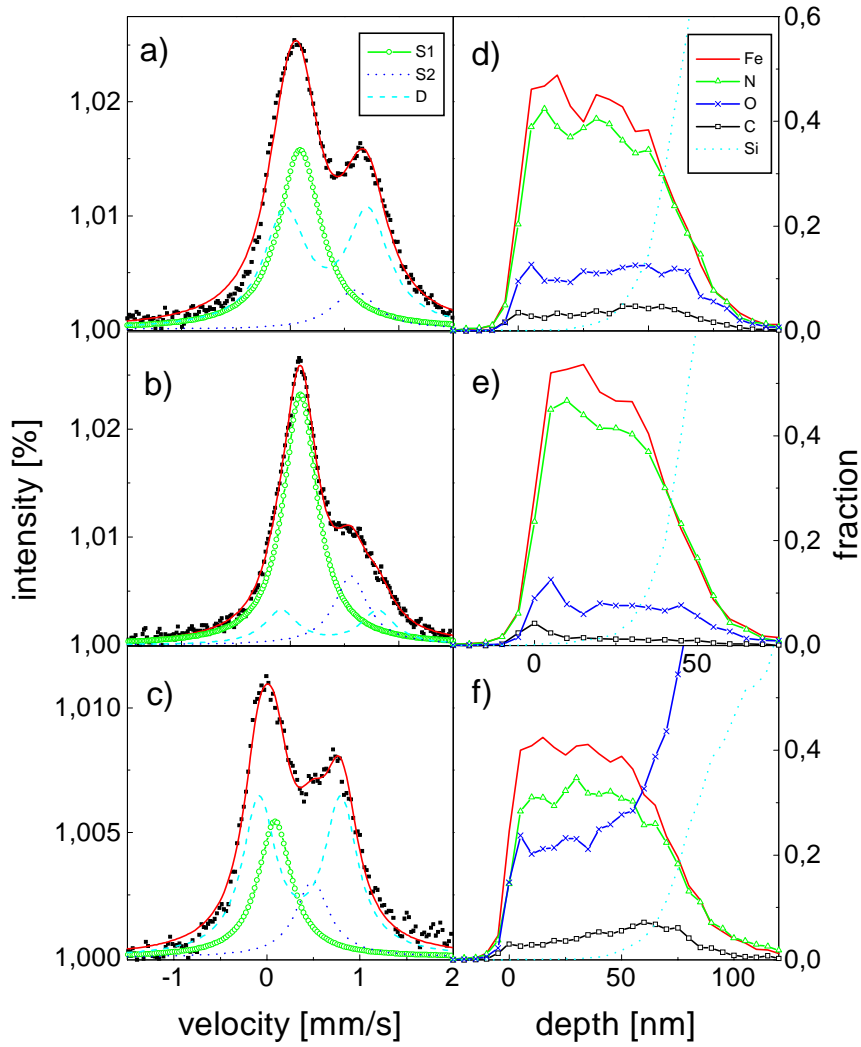


Figure 3.13: CEM and TOF-ERDA spectra of samples deposited at 573 K but with different substrate bias voltages: (a) and (d) -20 V, (b) and (e) 0 V, and, (c) and (f) +20 V.

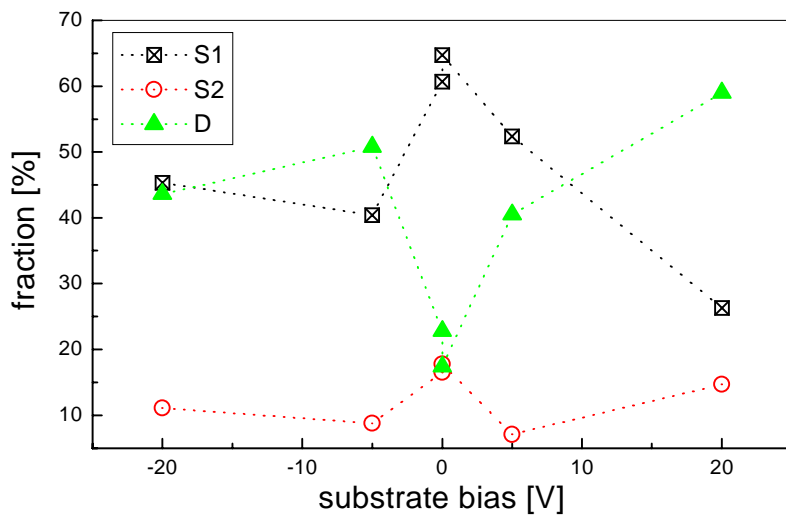


Figure 3.14: CEM subspectra fractions as a function of the substrate bias voltage.

## Origin of the doublet

The origin of the quadrupole doublet remained unexplained until now. It can be resolved by comparing the fraction of the doublet in the CEM spectra with the amount of impurities measured by TOF-ERDA. Figure 3.15 shows the evident connection between them. The right hand side y-axis denotes the probability of nearest neighboring sites to be occupied in the NaCl-type structure. The probabilities have been calculated using the binomial distribution (see equation 2.35).  $P_{12}$  stands for summing the probabilities of one and two nearest neighboring sites to be occupied by an impurity atom or to be vacant. The agreement between theoretical calculation and experimental results confirms the doublet to be due to the EFG (electric field gradient) tensor caused by the electrically asymmetric environment of the Fe atoms in the lattice (crystal defects and contaminant elements on the nitrogen sites). Another proof for the doublet to originate from the NaCl-structure ( $\gamma''$ -FeN) can be gained from XRD measurements. In Figure 3.16 the lattice constants of all the films analyzed are plotted as a function of the CEMS doublet fraction. The deposition parameters, therefore, vary between various samples. The lattice constant of the  $\gamma''$ -phase stays relatively independent of the doublet fraction. Instead, the  $\gamma''$ -phase lattice constant increases with the increasing fraction of the doublet.

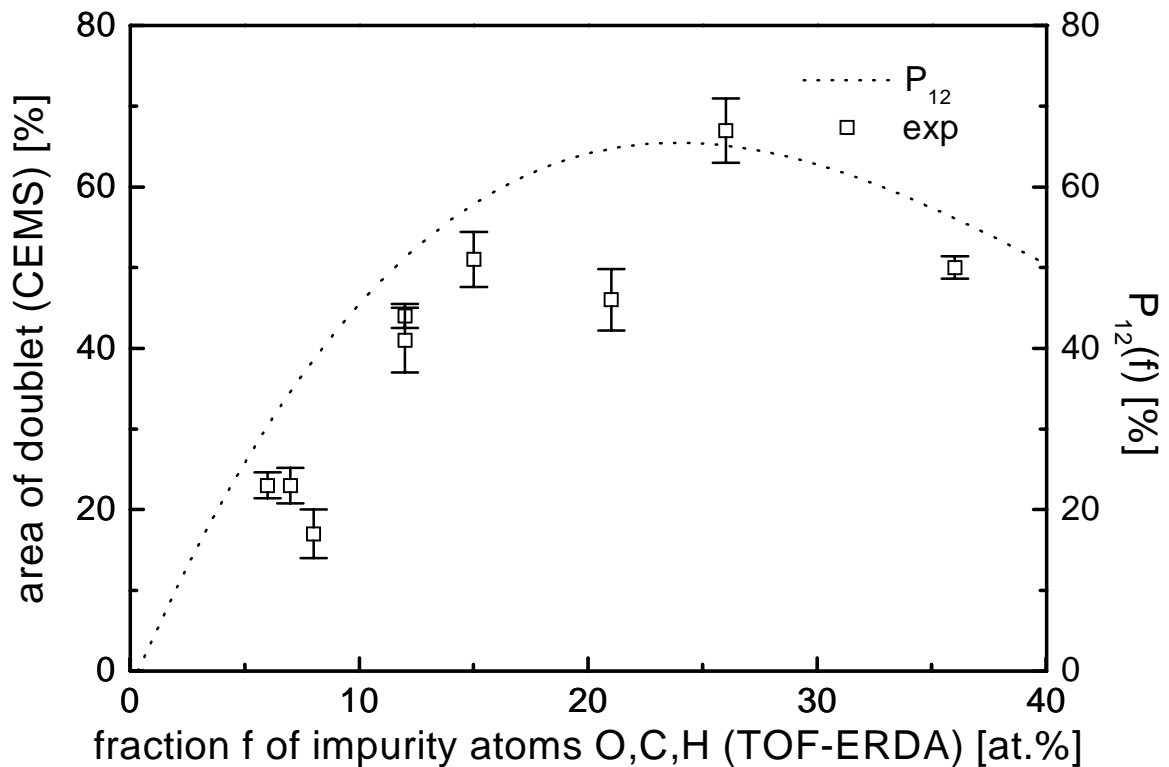


Figure 3.15: Comparison of TOF-ERDA results with the fraction of the CEMS doublet and with the probability of the missing nearest neighbors of Fe atoms in the NaCl-structure.

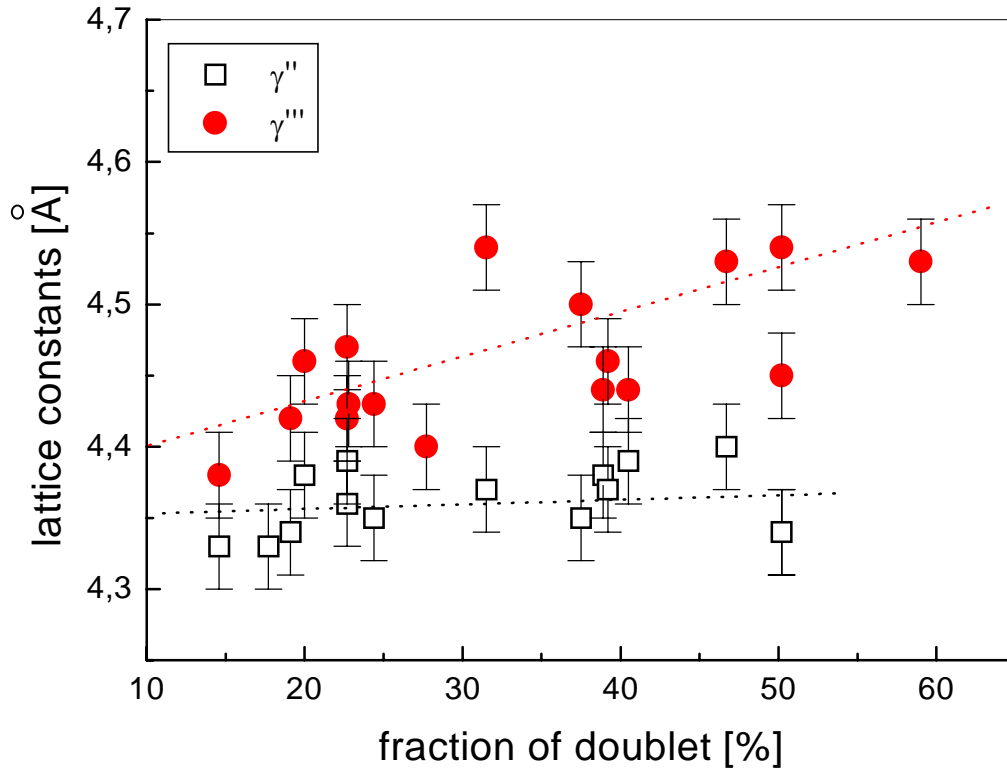


Figure 3.16: Lattice constants of  $\gamma''$ - and  $\gamma'''$ -phases vs. the fraction of the CEMS doublet.

### 3.5 RF power

The sputtering yield of the target atoms increases with the increase of the kinetic energy of the bombarding particles. Therefore, the amount of sputtered target material in the deposited film is directly proportional to the RF power applied to the system.

#### FeN

In order to confirm this expectation the RF power was increased from 110 W up to 160 W. All analyzing methods indicate an increase in the Fe content. In addition the CEM spectra reveal that the FeN phase is converted into the  $\epsilon$ -structure. Iron nitride films deposited with 110 and 160 W, respectively, are shown in Figure 3.17. At 160 W RF power the  $\epsilon$ -Fe<sub>2</sub>N<sub>1-x</sub> quadrupole doublets are dominating the CEM spectrum, while only a small fraction of  $\gamma''$ -FeN (singlet S1) is left.

#### Ni<sub>3</sub>N

The first Ni<sub>3</sub>N depositions were done with a RF power of 110 W. After reducing the N<sub>2</sub>-flow and elevating the substrate temperature there was still some excess nitrogen in the films. Due to that the RF power was increased up to the value of 150 W which was enough to produce the Ni<sub>3</sub>N-phase with correct stoichiometry. In Figure 3.18a a RBS spectrum of Ni<sub>3</sub>N film deposited on Si-substrate at 523 K is shown, with 150 W RF power and with an Ar-flow of 27 sccm and a N<sub>2</sub>-flow of 12 sccm. The analysis of the RBS spectrum exhibits a homogeneous film of 80 nm thickness with the stoichiometric composition Ni<sub>75(2)</sub>N<sub>25(2)</sub>.

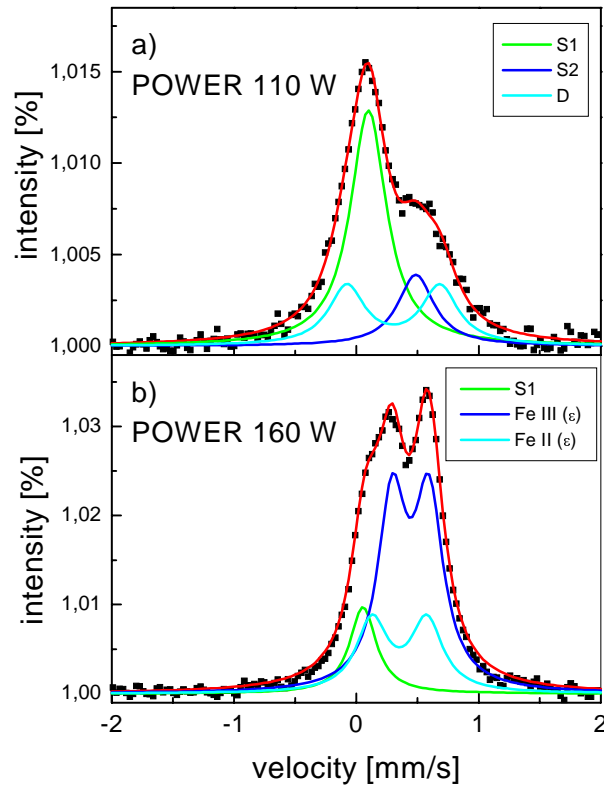


Figure 3.17: CEMS spectra of FeN films prepared with different RF powers.

The depth profile of Ni obtained from this RBS spectrum is presented in Figure 3.18b along with the N-profile obtained from RNRA. Both profiles confirm the homogeneous and stoichiometric nature of the deposited nitride layer. XRD analysis of this film exhibits several sharp diffraction peaks corresponding to the  $\text{Ni}_3\text{N}$  compound, which has a hexagonal structure and lattice constants of  $a = 0.269(5)$  nm and  $c = 0.432(5)$  nm (see Figure 3.19). The film has (101) preferred orientation.

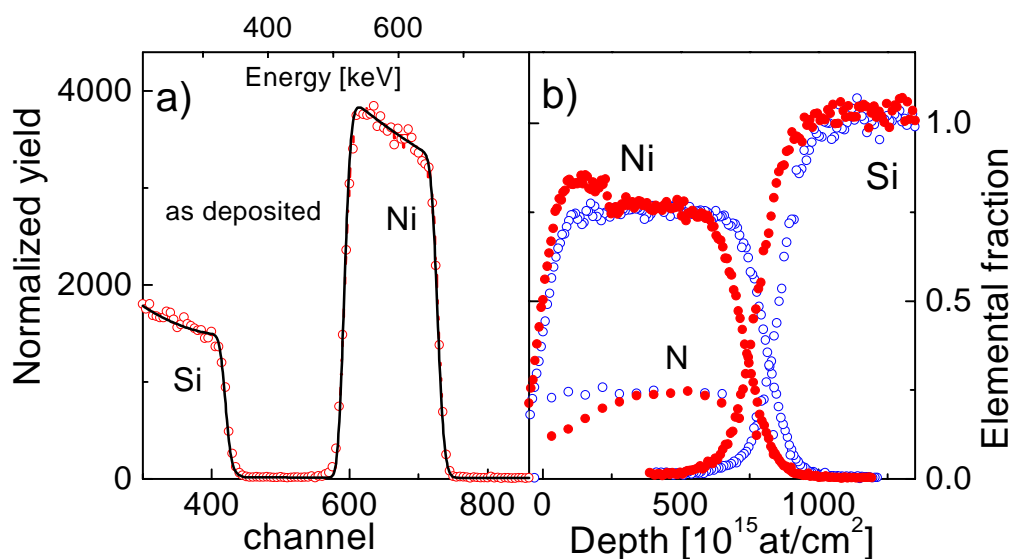


Figure 3.18: a) RBS spectrum and b) elemental profiles of as deposited  $\text{Ni}_3\text{N}$  film on Si substrate at 523 K, with 150 W RF power, 27 sccm Ar- and 12 sccm  $\text{N}_2$ -flow.

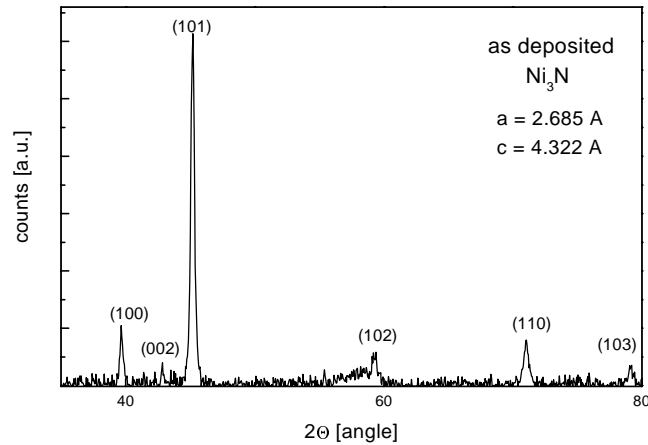


Figure 3.19: XRD spectrum of as deposited Ni<sub>3</sub>N film on silicon substrate.

### 3.6 Stability against annealing

#### Thermal stability of the FeN films

A sample prepared at room temperature with an Ar-flow of 27 sccm and a N<sub>2</sub>-flow of 27 sccm, at 110 W RF power and 293 K, was heated in vacuum, pressure  $\sim 5 \times 10^{-6}$  mbar. The fraction of the quadrupole doublet in the CEM spectrum was especially large. The aim was to reduce the doublet fraction and to observe how annealing affects other properties of the layer. The sample was annealed in 50 K intervals between 423 K and 723 K for 1 h, respectively. After the treatment, several analyses were carried out. The CEM spectra after every annealing step are shown in Figure 3.20. With increasing annealing temperature the fraction of the doublet grows constantly, while the single line fractions decrease. After heating at 573 K the S2 line has totally vanished. Heating at a temperature of 673 K produces an oxidized layer. The changes of the isomer shifts and the quadrupole splitting as a function of the annealing temperature are presented in Figure 3.21. The quadrupole splitting of D and the isomer shift of S2 decrease, while the isomer shifts of D and S1 increase slightly with increasing temperature. The increase of the quadrupole splitting indicates the reorganizing of the lattice. The crystallinity of the structure improves, which is also proved by the decreasing lattice constant. The XRD analysis resulted in a lattice constant of  $a = 0.454(5)$  nm for the as deposited sample whereas after the heating at 523 K the value was  $a = 0.447(5)$  nm. The decreasing (increasing) isomer shift implies the uptake (intake) of the electron density at the iron nucleus. At 573 K the S2 line vanishes. At 723 K the layer becomes oxidized, which is indicated by the typical iron oxide sextet lines in the CEM spectrum. The fact that the fraction of S2 diminishes faster than the one of S1 and that the S2 line vanishes totally could mean that the oxygen atoms prefer the NaCl-structure. This is in good agreement with the growing fraction of the doublet, which also originates from the NaCl-structure.

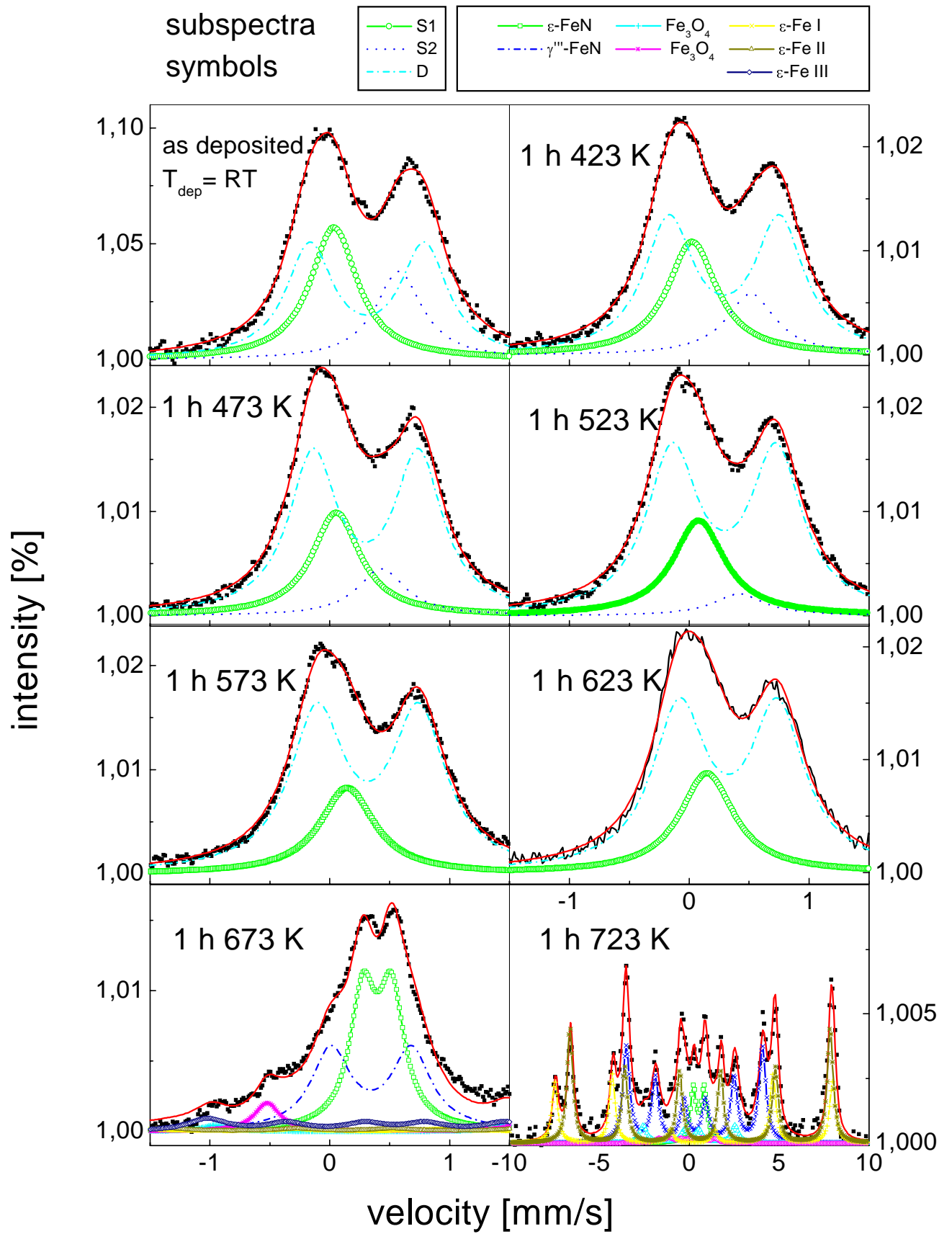


Figure 3.20: CEM spectra of the FeN samples annealed in vacuum for 1 h at each temperature.

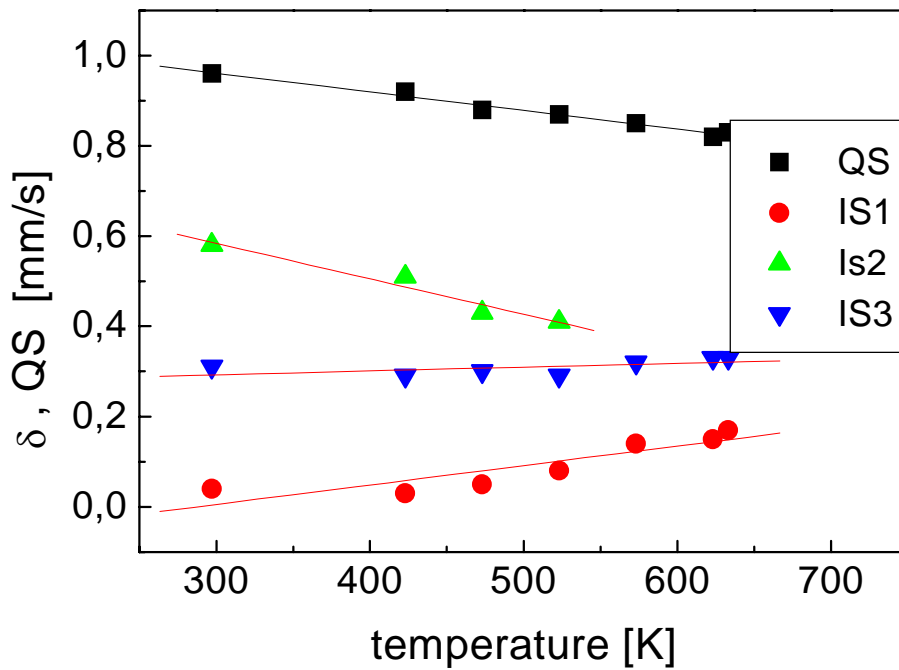


Figure 3.21: Isomer shifts and quadrupole splitting as function of the deposition temperature of the vacuum annealing series. The absolute error is included in the size of the symbol.

In Figure 3.22a the iron fractions obtained from RBS of an as deposited and a sample annealed in vacuum at 523 K are plotted. The Fe signal has slightly increased its intensity after the annealing, which is an indication for dissociation of FeN and out-diffusion of nitrogen. The TOF-ERDA measurement done after the last heating step at 723 K (see Figure 3.22b) shows that almost all nitrogen has left the sample and been replaced by oxygen. This proves that the FeN has dissociated and the film has oxidized.

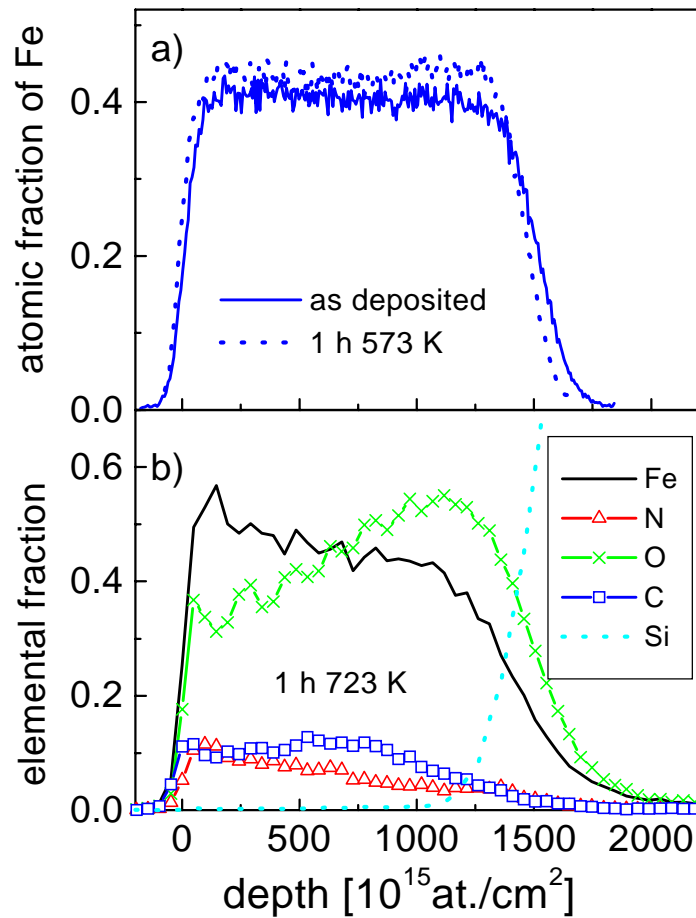


Figure 3.22: RBS spectra of the FeN samples annealed in vacuum.

The CEM spectrum of a sample deposited at 573 K with 27 sccm Ar-flow and 30 sccm N<sub>2</sub>-flow was dominated by the singlet S1. This sample was heated in H<sub>2</sub>-flow at 473, 523 and 573 K, for 1 hour, respectively. The goal was to achieve a pure FeN phase consisting only of the S1 single line and therefore reduce the relative fractions of the other subspectra contributions. The development of the subspectra fractions in the CEM spectra with the increasing temperature is shown in Figure 3.23a. At the first heating step at 473 K, the S1 fraction decreased, but increased again at 523 K. The fraction of the doublet experienced an opposite trend while the fraction of the S2 line decreased continuously. At 573 K the layer became fully oxidized. Then only small fractions of  $\epsilon$ -Fe<sub>3</sub>N<sub>1+x</sub> were found in the CEM spectrum which otherwise could be decomposed into iron oxide sextets. Figure 3.24 presents the hyperfine parameters of the subspectra as a function of the heating temperature. The decrease of the quadrupole splitting and of the isomer shift of the S2 singlet was similar to the heating series performed in vacuum. We already know that the decreasing quadrupole splitting indicates the rearrangement of the structure into improved crystallinity. The change in the isomer shift was a sign of the changing electronic density at the Fe nucleus. The isomer shifts of S1 and of the quadrupole doublet first increased, but in contrast to the vacuum heating, after the 523 K heating step the values decreased a little. The line width decreased continuously with the increasing annealing temperature. The TOF-ERDA performed after 473 K annealing showed a very homogeneous FeN layer with low impurity concentrations (O~5 at.%, C~2 at.%). This was verified by RNRA and RBS analyses.

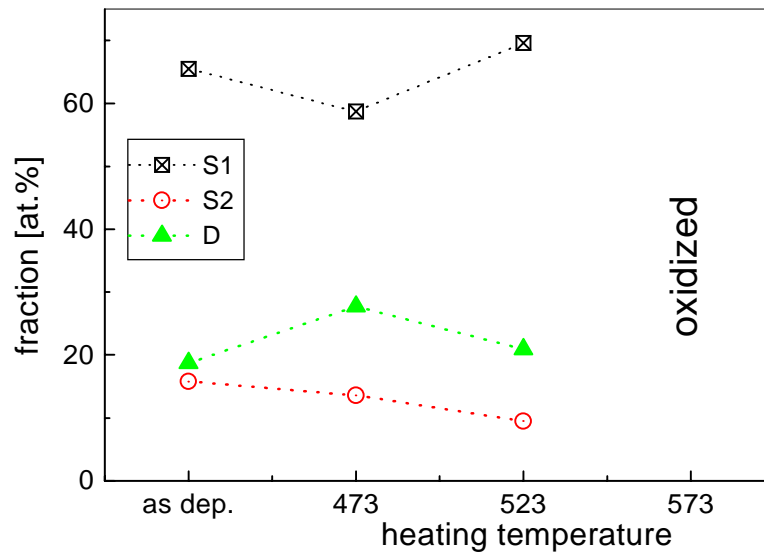


Figure 3.23: Fractions of CEM subspectra of samples annealed in  $H_2$  as a function of the annealing temperature.

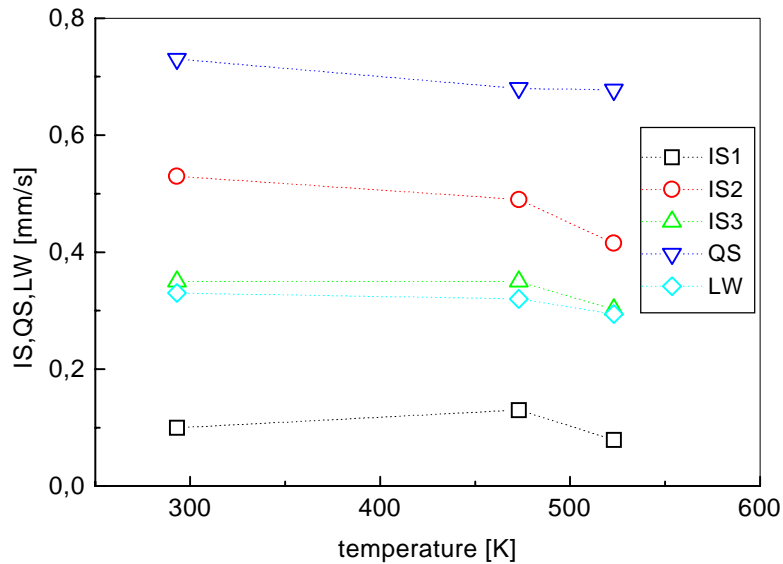


Figure 3.24: CEMS hyperfine parameters (isomer shift, quadrupole splitting and line width) of a sample heated in  $H_2$ .

Nitride layers can be formed thermochemically in an atmosphere containing  $NH_3$ . Nitriding temperatures of 773-873 K usually lead to porosity of the layer. Inia et al. [44] introduced a method to form iron nitrides at temperatures of 600 K and below, using a thin nickel layer on top of Fe. On a sample having a small fraction of the doublet in the CEM spectrum, a 10 nm thin Ni layer was evaporated. The sample was then annealed in  $NH_3$  at 625 K for 1 hour. At the same time, a similar sample without a Ni layer was treated in the same way. The heating was repeated at the same temperature for 4 hours. The aim was to observe how the nitrogen-rich films react to the heating in  $NH_3$ . CEM spectra of the as deposited and heated samples are shown in Figure 3.25. After 1 hour of heating, the fractions of S1 and S2 had decreased considerably. After a 4-hour heating period,  $N_2$  had diffused out of the samples, leaving the films in the  $\epsilon$ -phase. The nitrogen profiles measured by RNRA are displayed in Figure 3.26. The 1-hour-heating reduces the N-content of the sample surfaces. On the contrary, the deeper layers gain higher N-concentrations. After 4 hours, the drop in

the N-content was obvious and extensive throughout the whole film. In summary, heating in  $\text{NH}_3$  reduced the nitrogen content of the sample.

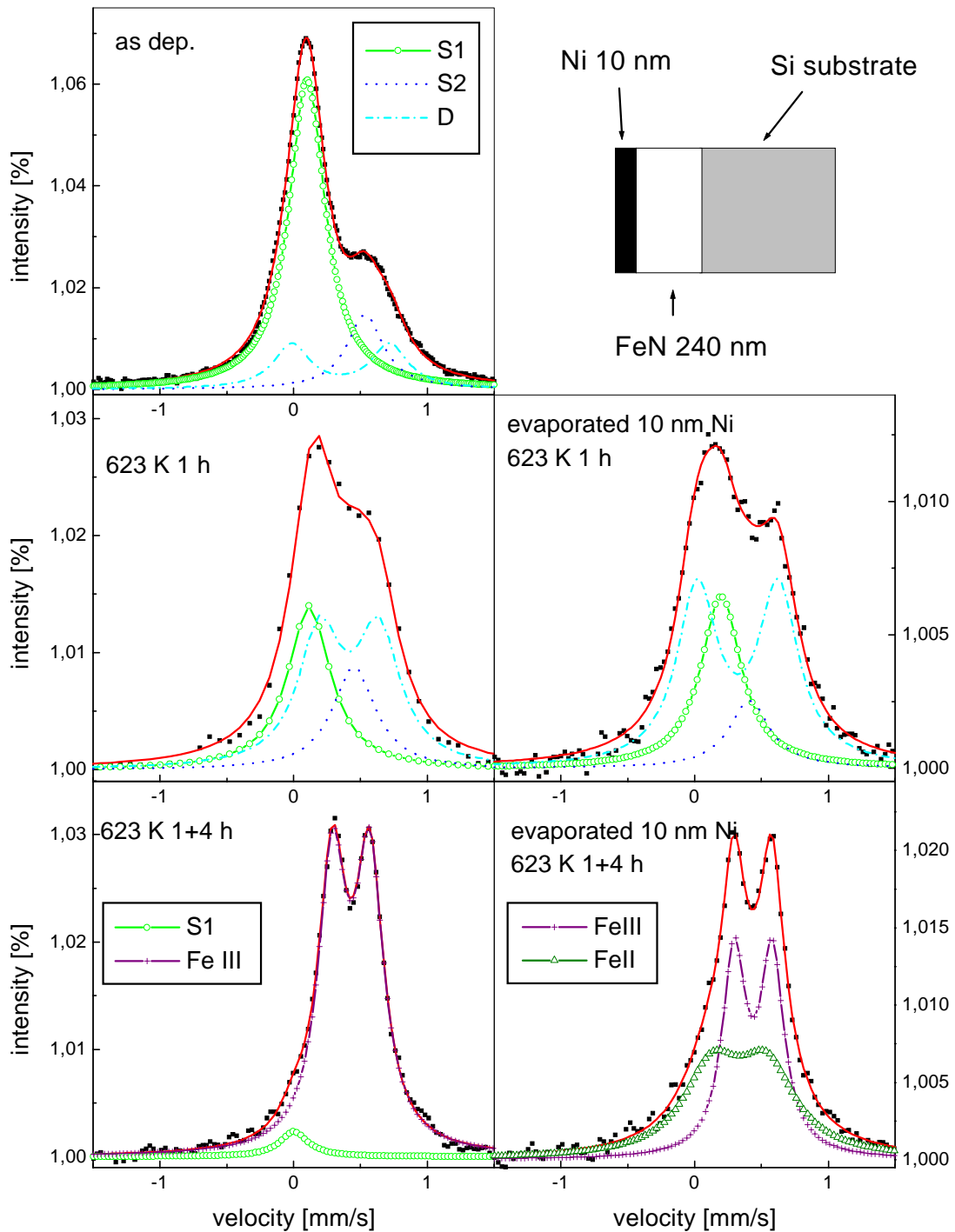


Figure 3.25: CEM spectra of two samples heated in  $\text{NH}_3$ . On the other sample a 10 nm thin Ni layer was evaporated before heating.

The temperature was chosen perhaps too high and the heating time too long to promote the uptake of nitrogen. FeN started decomposing. The affinity of N for FeN plays an important role and is probably much lower than that for Ni.

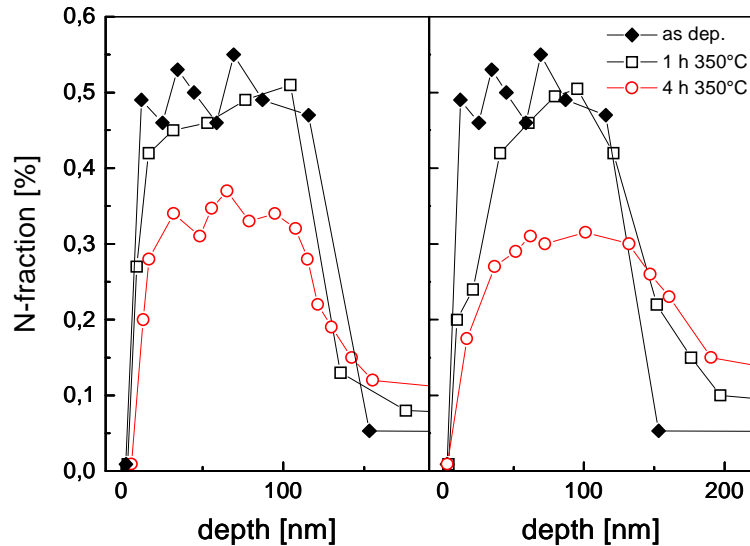


Figure 3.26: RNRA profiles of samples heated in  $\text{NH}_3$  (623 K for 1 h and 4 h). The (absolute) errors are smaller than the symbols used.

### Thermal stability of the Ni<sub>3</sub>N films

Several Ni<sub>3</sub>N samples, having about 5 at.% excess of nitrogen, were heated both in air and in vacuum. The goal was to find out whether the nitrogen diffuses out without the layer to be oxidized. The temperatures were chosen low enough to be certain that the Ni<sub>3</sub>N phase would not start dissociating, but hoping that nitrogen atoms sitting at interstitial places and at grain boundaries would diffuse out. Three identical samples were heated separately. One of them was annealed in air at 398 K, the second also in air but at a slightly higher temperature of 443 K and the third sample in vacuum at 398 K. Each of the annealings lasted for one day (24 h). Since the results from all the different annealings were similar, they are presented together. The most precise information of the possible changes in the nitrogen content is given by RNRA. In Figure 3.27 RNRA spectra of all the annealed samples along with the as deposited nitrogen profile are presented.

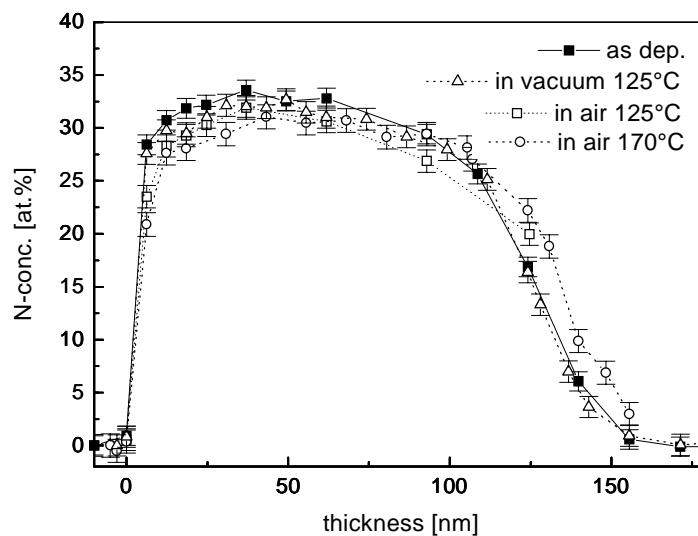


Figure 3.27: RNRA nitrogen profiles of Ni<sub>3</sub>N films annealed in vacuum or in air at different temperatures for 24 h each.

The nitrogen profiles develop in the expected way: the nitrogen concentration slowly decreases with the increasing heating temperature. Obviously, the out-diffusion of nitrogen at the temperatures used in this work was quite moderate. There seem to be no differences between the annealings done at different atmospheres. The RBS spectra taken from the samples showed a similar decrease in the N-content as RNRA. No indications of oxidation were found. The XRD measurements exhibit no changes in the diffraction patterns compared to the spectrum of an as-deposited sample.

### 3.7 Discussion, summary and outlook of characterization

After systematic investigation of the optimum parameters for deposition of  $\text{FeN}_y$ , of the correct 1:1 stoichiometry and of 90 % phase purity, and  $\text{Ni}_3\text{N}$  films were found. The thin nitride films were successively produced. The influence of the deposition parameters on the nitride film properties was studied and the results are summarized in Table 3.

Table 3. Influence of the deposition parameters in reactive magnetron sputtering.

<b>Deposition parameter</b>	<b>Influence on the nitride film</b>
<b>Gas flows, i.e. Ar and <math>\text{N}_2</math> partial pressures</b>	varying nitrogen content, very non-linear effect
<b>Substrate temperature</b>	increasing $T_{\text{subs}} \Rightarrow$ decreasing nitrogen and impurity content, improved crystallinity and homogeneity
<b>RF power</b>	increases the amount of sputtered target material in the compound
<b>Substrate bias voltage</b>	increases the impurity (O,C,H) content

The production of thin nitride films by reactive magnetron sputtering is a complex process in which the sputtering parameters strongly affect the properties of the films. Preparing a pure phase turns out to be rather difficult, especially when the role of light contaminant elements (H,C,O) in the production of single-phase nitride films is considered. The thermodynamics strongly prefer the formation of oxides over nitrides and therefore the nitridation process is extremely sensitive to the presence of oxygen even in very small amounts. Some atomic percent of oxygen and other light impurity elements, such as carbon and hydrogen, were found in every nitride film.

In view of the complexity of the Fe-N phase diagram and the little information available for the new FeN phase, the films were characterized by using several nuclear (ion-beam analytical and hyperfine) as well as conventional thin film analyzing techniques. The comprehensive analyses gave evidence that a combination of TOF-ERDA for profiling the constituent elements in the films, and of CEMS for identifying the phases is best suited for checking the quality of the FeN films. The properties of the FeN phase, the structure and the stability range are presented in Table 4.

Table 4. Properties of the magnetron sputtered FeN.

<b>Structure</b>	Mixture of two cubic phases $\gamma'''$ -FeN: NaCl-type , a = 0.446 nm $\gamma''$ -FeN: ZnS-type , a = 0.435 nm the pure FeN assumed to have ZnS-type structure								
<b>Stability</b>	Deposition temperature range: 293 – 615 K <table border="0" data-bbox="288 555 1056 763"> <thead> <tr> <th data-bbox="288 555 735 589"><b>Annealing atmosphere</b></th> <th data-bbox="735 555 1056 589"><b>maximum temperature</b></th> </tr> </thead> <tbody> <tr> <td data-bbox="288 611 735 645">In vacuum</td> <td data-bbox="735 611 1056 645">~ 623 K</td> </tr> <tr> <td data-bbox="288 667 735 701">In H<sub>2</sub>-flow</td> <td data-bbox="735 667 1056 701">~ 523 K</td> </tr> <tr> <td data-bbox="288 723 735 757">In NH<sub>3</sub></td> <td data-bbox="735 723 1056 757">~ 623 K</td> </tr> </tbody> </table>	<b>Annealing atmosphere</b>	<b>maximum temperature</b>	In vacuum	~ 623 K	In H <sub>2</sub> -flow	~ 523 K	In NH <sub>3</sub>	~ 623 K
<b>Annealing atmosphere</b>	<b>maximum temperature</b>								
In vacuum	~ 623 K								
In H <sub>2</sub> -flow	~ 523 K								
In NH <sub>3</sub>	~ 623 K								

An open question is still the nitrogen solubility limits of the FeN phase. What concentration range do  $\gamma''$ - and  $\gamma'''$ -FeN cover? What is the maximum solubility of nitrogen in iron?

The combination of RBS, RNRA and XRD served best in the analyzing of Ni<sub>3</sub>N layers. When the information given by the analyzing methods is understood and the characteristics of the deposition system are known the reactive magnetron sputtering can be utilized for tailoring the structure and the stoichiometry of transition metal nitrides over a wide concentration range.

## 4 Ion-beam irradiation of Ni<sub>3</sub>N/Si bilayers

The former chapter presented a detailed investigation of the production of thin nitride films via reactive magnetron sputtering. Both FeN and Ni<sub>3</sub>N phases were successfully deposited with the right structure and stoichiometry. Due to its interesting properties, being a weakly bound system, Ni<sub>3</sub>N was chosen as a bilayer material for ion beam mixing experiments. Thin nickel nitride layers were sputtered on Si-substrate and then irradiated with energetic Xe ions.

This chapter is divided into two main parts: the first gives a short introduction to ion beam mixing and especially to the parameters that affect atomic transport processes during ion irradiation. The effects of energetic ions on the surface and on the deeper parts of the sample are discussed. The second part presents the experimental results obtained from Xe irradiations. The modification of the nitride surface has been investigated by ions with low incident energy. For the mixing of Ni<sub>3</sub>N/Si interface were used two higher Xe ion energies and also the effect of the irradiation temperature was observed.

### 4.1 Irradiation induced surface effects

Energetic particle bombardment removes atoms in the near-surface layers of the sample. This removal, called sputtering, sets the limit of the maximum concentration of atoms that can be implanted and retained in the target [14]. At low ion fluences the resulting depth concentration profile of the incident ions implanted in the material is well characterized by a gaussian distribution. During high dose implantation an equilibrium state is reached, where as many implanted atoms are removed by sputtering as are replenished by implantation. Then the maximum concentration of the implanted profile is usually at the surface and falls off over a distance comparable to the initial ion range. Different target species may be sputtered at different rates. Indeed, preferential sputtering has been observed in many cases due to differences in binding energies, amounts of energy transferred to atoms of different masses, and sputtering probabilities.

The sputtering does not only lead to material loss but it also changes the topography of the surface. Usually ion irradiation increases the surface roughness. The sputtering yield ranges normally between 0.5-20 atoms/incident ion, depending upon ion species, ion energy and target material. Also Gibbsian absorption [45], known as thermal surface segregation, as well as the effects of spatially nonuniform rates of damage and ion deposition, should to be taken into account.

Irradiation may also change the composition of the target surface. These changes extend usually to a depth comparable with the range of the incident ion. The preferential sputtering may induce the migration of atoms toward the surface to compensate the loss of certain species or deeper in the sample to dilute the surface enrichment. In addition the altered composition is caused by radiation enhanced diffusion, recoil implantation or cascade mixing. The following section addresses these processes affecting compositional changes.

## 4.2 Ion beam mixing

Ion beam mixing (IBM) is a widely used method for modifying the structure and properties of bilayer and multilayer systems [12-14]. The idea behind IBM is to create a surface alloy by homogenizing alternate layers deposited in a thickness ratio so that they result in a desired final composition after mixing. By IBM the amount of material A introduced in material B in a bilayer system exceeds greatly the maximum concentration that can be achieved by direct implantation. The ion bombardment leads to alternations both in the surface and in the deeper parts of the sample. The compositional changes brought about by ion bombardment deeper in the system, in the bulk material or in the interface between two different layers, are classified into recoil implantation, cascade mixing and radiation-enhanced diffusion. Microstructurally, the phases present are often altered, new metastable phases may form, the grain growth and the preferred texture can be changed. All these effects (illustrated in Figure 4.1) need to be understood before one can determine the effect of ion irradiation.

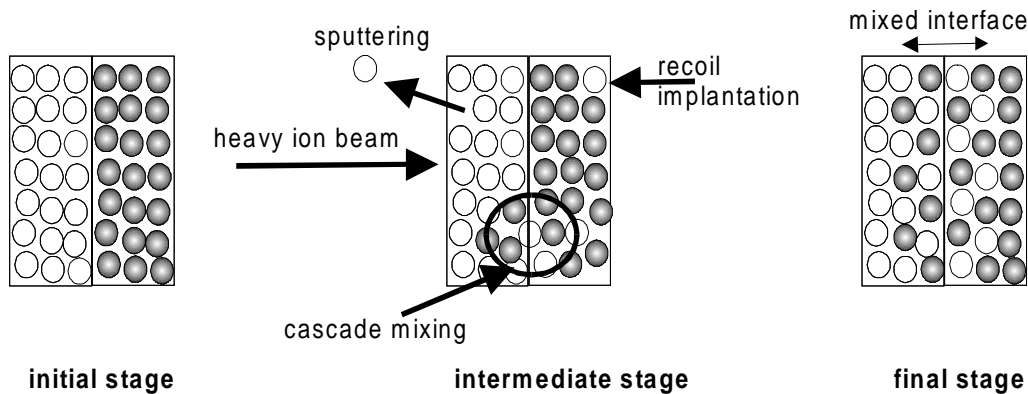


Figure 4.1: Schematic diagram of ion beam mixing processes.

When energetic particles penetrate into a solid they lose energy due to nuclear stopping, elastic collisions between the incident ion and the target atoms, and electronic stopping, electronic excitation and ionization of the target atoms. The collisions with the target atoms lead to cascades of primary, secondary, etc., recoils, which relax within a time constant of the order of picoseconds. The short duration and the small sizes of the cascades have precluded direct experimental investigation of their dynamics and the investigations are limited to what has occurred after establishing thermal equilibrium [15]. Molecular-dynamic calculations have provided important information on the different atomic relocation processes that decay with different time constants: (i) the collisional stage lasting a few tenths of a picosecond, (ii) the thermal spike stage lasting several picoseconds, and (iii) the relaxation stage lasting a few tenths of a picosecond. After thermal equilibrium has been established, the excess of defects produced may lead to enhanced mass transport, which can last up to several seconds depending on the temperature. The mixing which occurs in the first two stages is termed ballistic, while the third phase involves collective behavior giving rise to the term “thermal spike” to describe the distribution of energy among the atoms.

For heavy ion bombardments and heavy matrices ( $Z > 20$ ) the collision cascades are dense and thermal spikes are most likely. A thermal spike is described for very small volume,  $\sim 3$  nm radius for a cylindrical spike, where all atoms are essentially in motion with  $\sim 0.1$ - $1$  eV/atom energy density. By considering the Maxwell-Boltzmann distribution in the energized cascade region, the

concept of temperature may be considered. Another condition for the spike formation can be given by the critical energy [13]

$$E_C = 3.92 \times 10^{-2} eV \cdot Z^{2.23} \quad (4.1)$$

where  $Z$  is the average charge number of the target. From Figure 4.2 shows that the energy of the recoiled atom has to be below the critical energy for the spike formation, but larger than the displacement threshold energy  $E_d \cong 30$  eV.

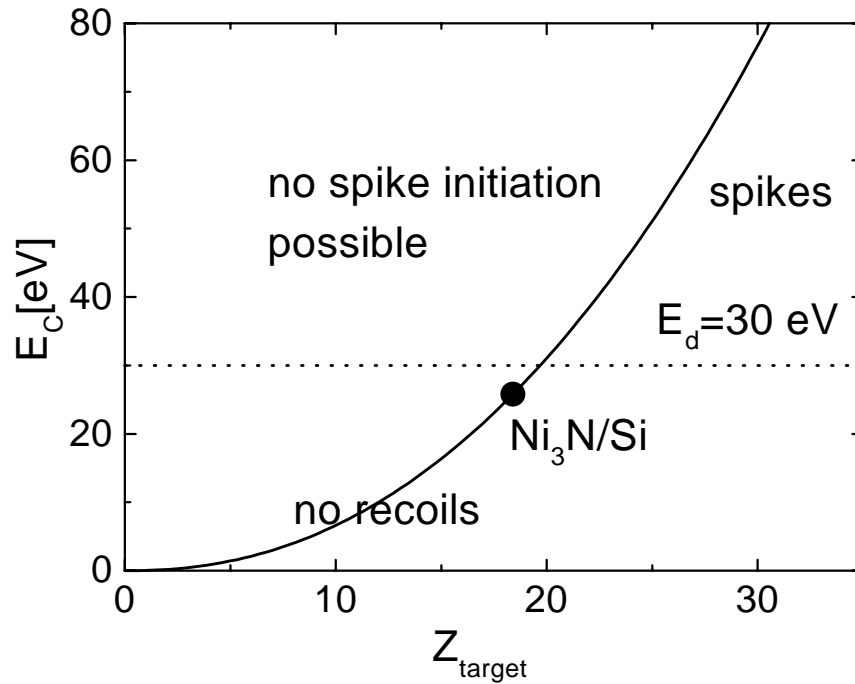


Figure 4.2:  $Z$  dependence on the critical energy  $E_C$  for spike initiation.

#### 4.2.1 Mixing due to ballistic effect

For systems with  $Z < 20$  the initiation of thermal spikes is not expected, but the mixing process is explained by the ballistic model which takes into account only the atomic collision kinetics, i.e. the atomic mass and density. The thermodynamic properties of the solid are not considered. An atom can be relocated by a single projectile ion with an energy in the keV range. The cross-section for such a collision is on the order of the square of the atomic radius and therefore a rare event. The cascade mixing, multiple relocations of atoms at low energies, dominates the ion beam mixing. In most of the investigations for low energy cascade mixing the broadening of the interface profile of a bilayer system, the variance, has been found to depend linearly on the ion fluence  $\Phi$

$$\Delta\sigma^2 = k\Delta\Phi \quad (4.2)$$

where  $\Delta\sigma^2 = \sigma_{\text{irr}}^2 - \sigma_{\text{as-prep}}^2$  is the increase of the variance as a result of the ion irradiation. The mixing efficiency is defined as the mixing rate divided by the deposited energy

$$\eta = \frac{\Delta\sigma^2}{\Delta\Phi \cdot F_D} \quad (4.3)$$

By the help of the mixing efficiency it is possible to compare experiments done on the same target material but with varying incident ion and energy.

In the recoil cascades most of the displaced atoms have kinetic energies close to the displacement threshold  $E_d \sim 20$  eV and thereby a similar range  $R_d \sim 1$  nm. The relocation process is equivalent to stable Frenkel pair formation. The motion can be regarded as a random-walk process. The collisional mixing rate given by Sigmund and Gras-Marti becomes [46]

$$k_{ball} = \frac{1}{6} \Gamma_0 \xi \frac{F_D R_d^2}{N E_d} \quad (4.4)$$

with

$$\xi = \sqrt{\frac{4M_i M_r}{(M_i + M_r)^2}} \quad (4.5)$$

where  $\Gamma_0 = 0.608$  is a dimensionless constant,  $\xi$  a kinematic factor involving the masses of the colliding atoms,  $F_D$  is the deposited energy per ion per unit length and  $N$  is the atomic density. The  $F_D$  value should be corrected for the non-isotropic ballistic energy transport of the primary recoil atoms in a following way [12]

$$F_D(z) = (2n_v(z) + n_r(z)) \cdot E_D \quad (4.6)$$

where  $n_v(z)$  stands for the number of produced vacancies per nm and incident ion and  $n_r(z)$  is the number of replacement collisions of the target atoms, respectively. The large energy transfer in nearly central collisions results in a large displacement of the recoil deeper into the target. The estimates for  $F_D$  were calculated by means of the cascade mode in TRIM [22].

#### 4.2.2 Mixing due to thermal spikes and thermochemical properties

It has been clearly demonstrated that the thermochemical properties of systems with  $Z > 20$  have a strong influence on the mixing process. In many metallic bilayer experiments the dependence of  $\Delta\sigma^2$  on  $\Phi$  deviates by factor of ten or more from the ballistic value[47]. The effect of the increasing negative heat of mixing and the decreasing cohesive energy have been observed to enhance the amount of mixing. They are taken as an evidence of the thermal spike formation, where the dominant atomic transport mechanism can be described as diffusional intermixing in a non-ideal solution

$$D = D_0 [1 - 2\Delta H_{mix} / k_B T]. \quad (4.7)$$

$D_0$  is the self-diffusion coefficient,  $\Delta H_{mix}$  the mixing enthalpy,  $k_B$  the Boltzman constant and  $T$  the temperature. The equation (4.7) shows that chemical biasing can contribute to ion mixing only when the particle kinetic energies are of order 1 eV. The search for theoretical explanation for transport processes in thermal spike has created some semiempirical model. The global spike model is based on a cylindrical spike around the ion path [3]. Formation of spatially separated local spherical spikes was assumed in some medium- $Z$  metallic bilayers by Borgesen and co-workers [48]. The overlapping of local spherical spikes in subcascades leading to cylindrical spike geometry

is expected when a recoil atom has reached the critical energy  $E_{sc} \approx 0.5 \text{ eV } Z^{2.23}$ . Different mixing mechanisms result in different relationships between the mixing rate  $k$  and the energy density  $F_D$  deposited by collisions:

- ballistic mixing  $k \propto F_D$
- global spikes  $k \propto F_D^2$
- local spikes  $k \propto F_D$
- radiation enhanced diffusion  $k \propto F_D^{1/2}$

The  $F_D$  dependence can thus be used for the characterization of the dominant mixing mechanism.

Mixing of ballistic ( $Z < 20$ ) systems seems also to depend on thermochemical potentials but the evidence for that is not yet sufficient. The theory explaining the nature of the transport process needs to be developed as well. In the case of a compound formation, Desimoni and Traverse have proposed a model that is incorporating a chemical driving force [49]. In several experiments the dependence of the variance  $\Delta\sigma^2$  of the mixed interface on the irradiation fluence  $\Phi$  was found to be either quadratic or linear. Depending on the fluence range, under a certain critical value, the mixing process is reaction controlled, e.g. compound formation, and above that fluence the process is diffusion controlled. The growing mixed region has in the latter case reached a critical thickness and the diffusion through the newly formed compound limits the mixing kinematics. Of course both types of processes are present in a given system all the time. For highly reactive systems the critical fluence is rather low. In some bilayers, such as Pd/Si, the ranges over which the individual processes dominate are clearly divided, while for example Cr/Si seems to experience purely quadratic dependence [50],[51]. The chemical reaction rate of the latter system is low which causes a relatively high critical dose. In the case of compound formation, the ballistic model can be corrected as follows

$$k_{comp} = k_{ball} \cdot 2 \cdot \left[ \frac{N_A}{a/(a+b)} + \frac{N_B}{b/(a+b)} \right] \quad (4.8)$$

$N_A$  and  $N_B$  are the atomic densities of the top layer A and the bulk material B in a bilayer where the ion irradiation leads to the chemical reaction  $A + B \Rightarrow A_aB_b$ .

### Radiation enhanced diffusion (RED)

In order to study the amount of intermixed atoms purely due to athermal mixing, the sample has to be cooled during the ion bombardment to suppress the thermally activated migration processes. At lower temperatures ion mixing is considered temperature independent. However, at elevated temperatures the radiation-enhanced diffusion dominates and the ion beam induced acceleration of atomic transport processes is mainly determined by vacancy-interstitial recombination [3]. The irradiation does not effect the activation energy of the defect migration, but only the concentration leading to a balanced production and annihilation of defects. RED has a more important role at low-mass ion irradiations. Experiments on the temperature dependence of mixing have shown that there are two critical temperatures  $T_C$  and  $T_{eq}$ ,  $T_C < T_{eq}$ , so that metastable phases are expected to form

between  $T_C$  and  $T_{eq}$  and equilibrium phases are expected to form above  $T_{eq}$  [52].  $T_C$  is defined as a formation energy for small holes, i.e. smaller sized constituent in the compound, while  $T_{eq}$  for large holes, i.e. larger sized constituent, and their empirical formulas are

$$T_C = 4.0 \cdot \Delta H_{V_{small}} \quad (4.9)$$

and

$$T_{eq} = 3.8 \cdot \Delta H_{V_{large}} \quad (4.10)$$

where temperatures are given in K and the vacancy formation enthalpies in kJ/mole. Miedema's model [53] gives the vacancy formation enthalpies for an alloy  $A_{1-x}B$  as follows

$$\Delta H_V^A = c_A \Delta H_{IV}^A + (1 - c_A)(V_A/V_B)^{5/6} \Delta H_{IV}^B \quad (4.11)$$

and

$$\Delta H_V^B = c_B \Delta H_{IV}^B + (1 - c_B)(V_B/V_A)^{5/6} \Delta H_{IV}^A \quad (4.12)$$

where  $\Delta H_{IV}^A$  and  $\Delta H_{IV}^B$  are the mono vacancy formation enthalpies in pure A and B.  $V_B/V_A$  is the molar volume ratio and  $c_A$  and  $c_B$  are the concentrations depending on  $x$ . According to de Reus the radiation-enhanced diffusion occurs when the smaller constituent of the alloy becomes mobile and the formation of equilibrium crystal structures requires collective motion of both constituents [52]. The literature values for the variables above were not found for Ni<sub>3</sub>N, but only for pure Ni [54]. Equation (4.9) gives the value of 344 K for the critical temperature of Ni.  $\Delta H_{small}$  for Ni is 86 kJ/mole.

Cheng et al. obtained from experimental results a relationship between the critical temperature and the cohesive energy

$$T_C = 100 \cdot \Delta H_{coh} \quad (4.13)$$

For Ni<sub>3</sub>N/Si the critical temperature using (4.13) becomes about 440 K. The cohesive energy is taken as an average value of  $\Delta H_{coh}$  for Ni<sub>3</sub>N and Si. Before starting on the discussion of the irradiation results, the some important quantities of Ni<sub>3</sub>N/Si system are listed in table 2.

Table 2. Average atomic density, average charge number, critical energy, equilibrium temperature, critical temperature, cohesive energy and heat of reaction for the most probable chemical reaction between the bilayer materials.

System	Atomic density [at/nm <sup>3</sup> ]	$Z_{ave}$	$E_C$ [eV]	$T_{eq}$ [K]	$T_C$ [K]	$\Delta H_{coh}$ [eV/atom]	$\Delta H_r$ [eV/atom]
Ni <sub>3</sub> N/Si	73.65	18.4	26	-	-	4.595	-0.497

### 4.3 Low energy irradiation effects

In this chapter experimental results are presented for the 100 keV Xe<sup>+</sup> ion irradiation of Ni<sub>3</sub>N films resulting in the change of the surface roughness and film composition. At this energy, the Xe ions

do not reach the  $\text{Ni}_3\text{N}/\text{Si}$  interface. The low-energy irradiation results are necessary for determining the accurate interface growth rate during ion-beam mixing and ion-induced phase formation at the  $\text{Ni}_3\text{N}/\text{Si}$  interface. In many analyzing methods, such as RBS, the signal corresponding to the mixing at the interface is interfered by the signal due to irradiation effects on the surface.

The as-prepared  $\text{Ni}_3\text{N}/\text{Si}$  bilayers were irradiated with 100 keV  $\text{Xe}^+$  ions at 80 K for different fluences starting from  $0.5 \times 10^{16} \text{ Xe}/\text{cm}^2$  and increasing in steps of  $0.5 \times 10^{16} \text{ Xe}/\text{cm}^2$  up to the fluence of  $6 \times 10^{16} \text{ Xe}/\text{cm}^2$ . After every irradiation the samples were analyzed by various methods. By means of RBS the accumulation of the incident Xe ions in the target material could be observed. Figure 4.3 shows Xe concentration profiles for 100 keV Xe-ions up to the fluence of  $2 \times 10^{16} \text{ ions}/\text{cm}^2$ . The shape of the Xe profile stays gaussian at all dosis in spite of the sputtering. With increasing fluence the profile moves deeper into the sample. The ion irradiation induces defects, which seem to trap the Xe ions.

The collected Xe content was determined by integrating the Xe-peak area. The Xe content as function of the irradiation fluence is illustrated in Figure 4.4. The content increases with the implanted fluence and seems to reach the saturation level of about  $7.5 \times 10^{15} / \text{cm}^2$  at the fluence of  $2\text{-}3 \times 10^{16} \text{ ions}/\text{cm}^2$ , which corresponds to the collection efficiency of  $\approx 40 \%$ .

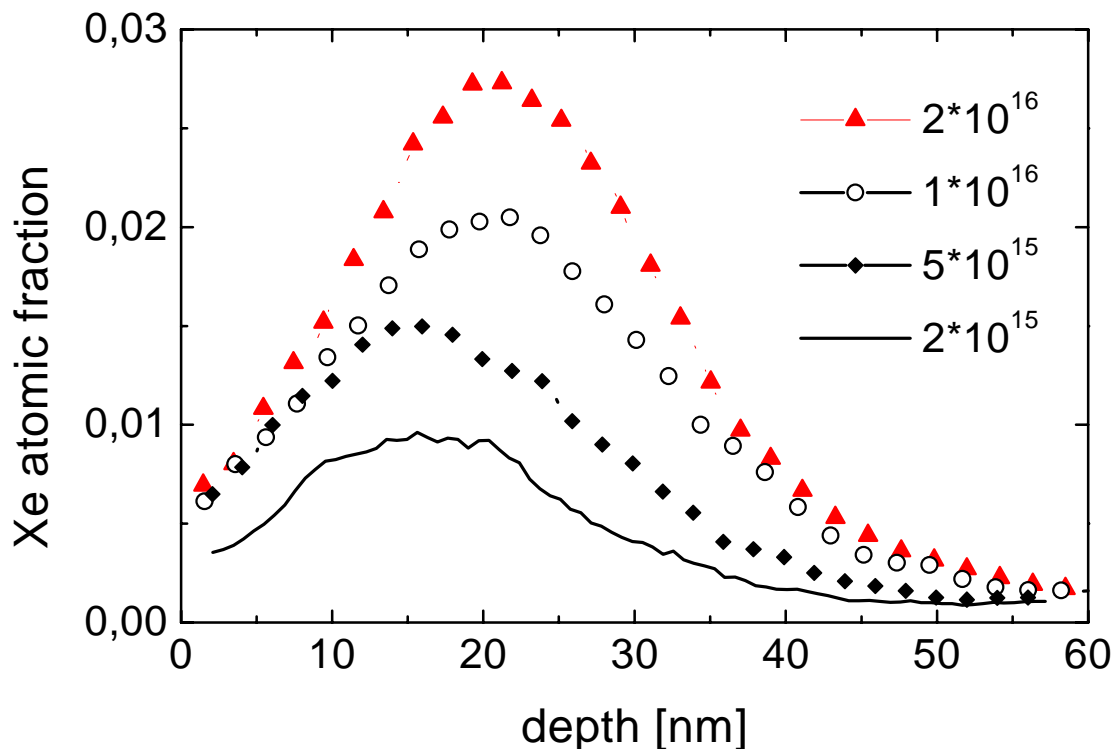


Figure 4.3: Xe-concentration profiles in  $\text{Ni}_3\text{N}$  after implantation with 100 keV Xe ions at 80 K.

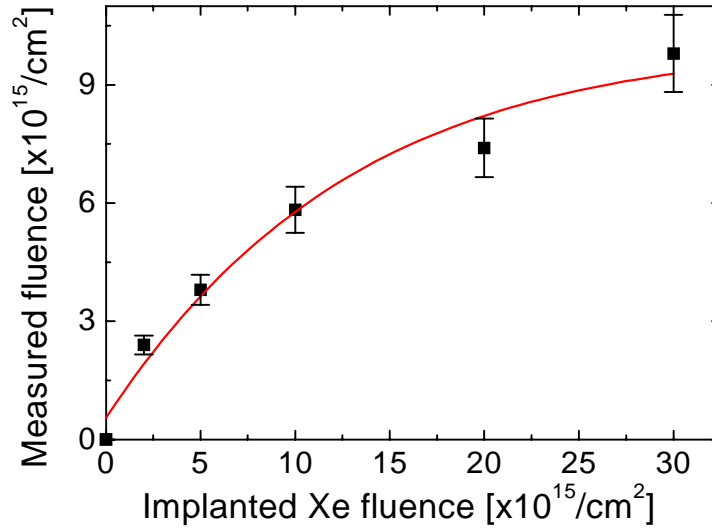


Figure 4.4: Collection curve of the integrated Xe-concentration profiles.

Figure 4.5a) show the RBS spectrum of an as-deposited Ni<sub>3</sub>N film along with that of a sample irradiated with a fluence of  $1 \times 10^{16}$  Xe/cm<sup>2</sup>. In the lower part of the figure the corresponding Ni and Si depth profiles determined by RBS and the nitrogen profiles measured by RNRA are presented. The combination of both methods gives very accurate information on the sample composition. When the as-prepared and the irradiated spectra are compared, three distinct features are clearly visible. Firstly the thickness of the irradiated layer has decreased due to surface sputtering. Secondly the near-surface composition has altered which can be observed as a change in the backscattering yield.

And third tails of the nickel signal (550 keV) and the Si signal (350 keV) are less steep than the as-deposited spectrum. Since we know that 100 keV Xe ions have not reached the substrate (the projected range of 100 keV Xe in Ni<sub>3</sub>N is  $\sim 25$  nm), the broadening cannot be due to mixing at the interface. The ion irradiation has obviously increased the surface roughness, which causes the broadening. From the Ni and N profiles displayed in Figure 4.5b) the stoichiometric changes of the nitride in the near surface region are clearly visible. The relative amount of nickel has increased while the nitrogen has been lost. Under irradiation Ni<sub>3</sub>N compound dissociates which leads to the outdiffusion of nitrogen. Ni<sub>3</sub>N is less resistive to energetic ions than the strongly bound nitrides AlN, TiN, CrN and Cr<sub>2</sub>N, for which no such deviations from stoichiometry were found [12]. At the interface Ni<sub>3</sub>N/Si there were no signs of nickel diffusion of the excess Ni (after the dissociation) into silicon. Ni is systematized to be a fast diffuser in silicon (especially in crystalline silicon) [55], but at 80 K or at room temperature the solubility is very low.

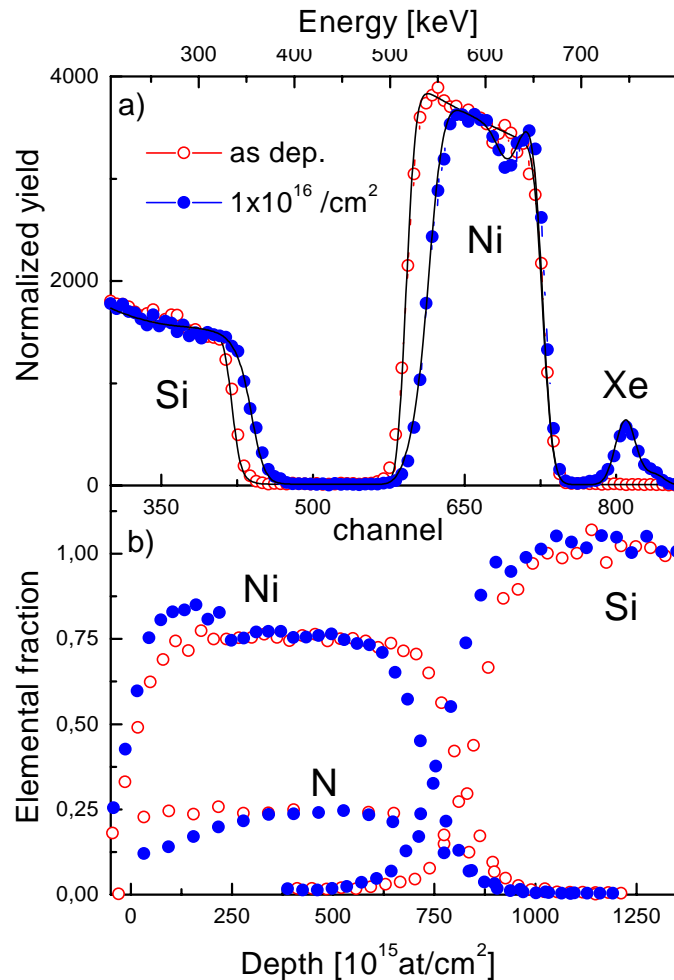


Figure 4.5: a) RBS spectra of as-prepared and irradiated ( $1 \times 10^{16}$  Xe/cm<sup>2</sup>) sample. b) Elemental profiles of the same samples determined by RBS (Ni and Si) and by RNRA (N).

The change in the near-surface composition raises the question, whether the Ni<sub>3</sub>N phase structure also has changed? Could we still see the Ni<sub>3</sub>N diffraction peaks in the XRD spectrum or has a new phase been formed?

The XRD spectra of the as-prepared Ni<sub>3</sub>N along with the spectra of two samples irradiated with 100 keV Xe ions with fluences of  $1 \times 10^{16}$  Xe/cm<sup>2</sup> and  $6 \times 10^{16}$  Xe/cm<sup>2</sup> are presented in Figure 4.6. At low fluences the 100 keV irradiation does not change the diffraction pattern at all. Even at such a high fluence as  $6 \times 10^{16}$  Xe/cm<sup>2</sup> the Ni<sub>3</sub>N peaks are still visible, even though the peaks have become broader due to the amorphization and have lost intensity because of the dissociation of the nitride and the sputtering effect. The very broad silicon peak is a result of the top nitride film thickness and the measurement geometry. Depending on the substrate orientation to the x-ray detector, the crystalline silicon causes an amorphous-like diffraction peak.

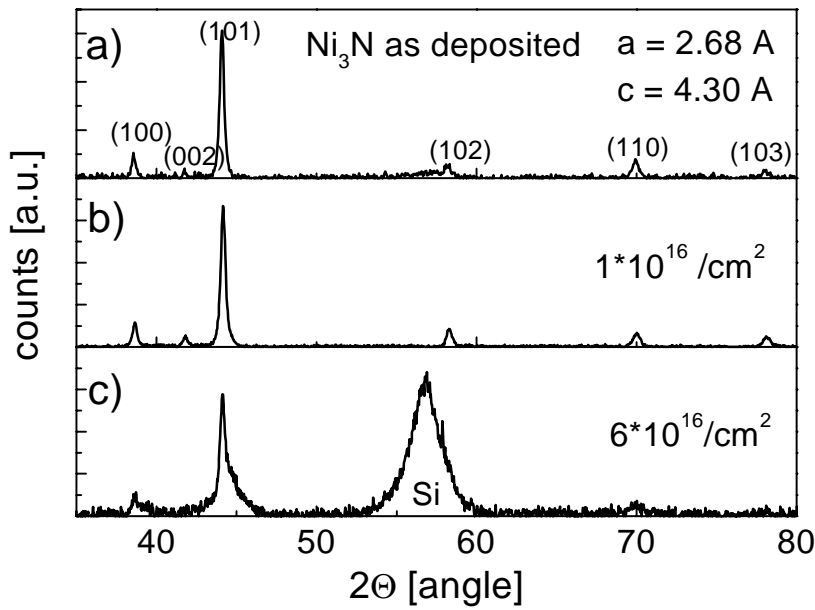


Figure 4.6: XRD spectra of a) an as-prepared and 100 keV Xe irradiated Ni<sub>3</sub>N/Si with fluences of b)  $1 \times 10^{16}$  and c)  $6 \times 10^{16}$  Xe/cm<sup>2</sup>.

The comparison of the as-deposited nitride layer thickness to the irradiated ones delivers us the information on the amount of material lost as a result of the sputtering. The sputter yield refers to the number of sputtered atoms per incoming ion. From TRIM95 simulation calculated value 7 atoms per ion is very close to the experimentally obtained sputtering yield of 6 atoms (Ni or N) per Xe ion. The sputtered thickness as a function of the irradiation fluence is plotted in Figure 4.7. At the fluence of  $1 \times 10^{16}$  Xe/cm<sup>2</sup>, sputtering removes about 15 nm and the sputtered layer linearly increases with the fluence.

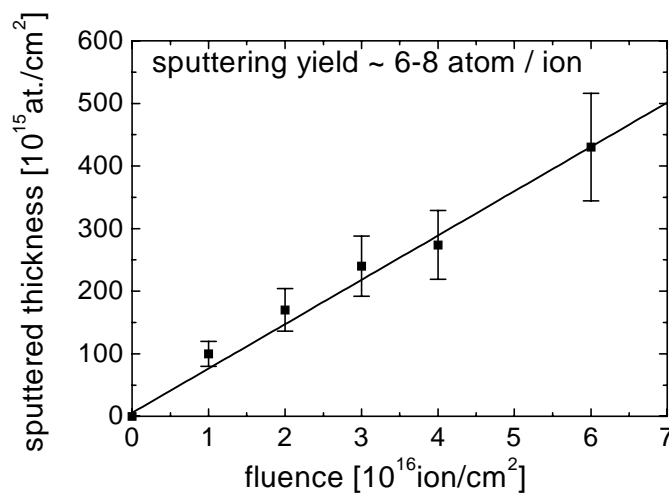


Figure 4.7: Sputtered thickness of Ni<sub>3</sub>N films as function of irradiation fluence for 100 keV Xe ions.

The broadening of the peak edges in the RBS spectrum was assumed to result from the increased surface roughening. To verify this assumption the sample surfaces were scanned by AFM. Figure 4.8 presents three-dimensional AFM images obtained from Ni<sub>3</sub>N films deposited on Si wafers; the first of the as-prepared sample and the second of the 100 keV Xe irradiated sample (fluence of

$1 \times 10^{16}$  Xe/cm<sup>2</sup>). The images have different sampling area, a)  $1 \times 1 \mu\text{m}^2$  and b)  $3.3 \times 3.3 \mu\text{m}^2$ . It is clear from these images that the surface roughness increases with the increasing fluence. The average roughness of the as deposited sample surface is  $\sim 1.9$  nm while after  $1 \times 10^{16}$  Xe/cm<sup>2</sup> irradiation fluence it has increased to almost 4 nm. Also the grain size changes due to ion bombardment. The as-prepared Ni<sub>3</sub>N film has rather large grains of the diameter  $\sim 225$  nm. The comparison of the film thickness of about 80 nm with the grain size suggests that the layer consists of very large, flat columnar grains. For increasing ion fluence the grain size first grows to 450 nm, but then decreases again to the value of  $\sim 200$  nm at the fluence of  $3 \times 10^{16}$  Xe/cm<sup>2</sup>.

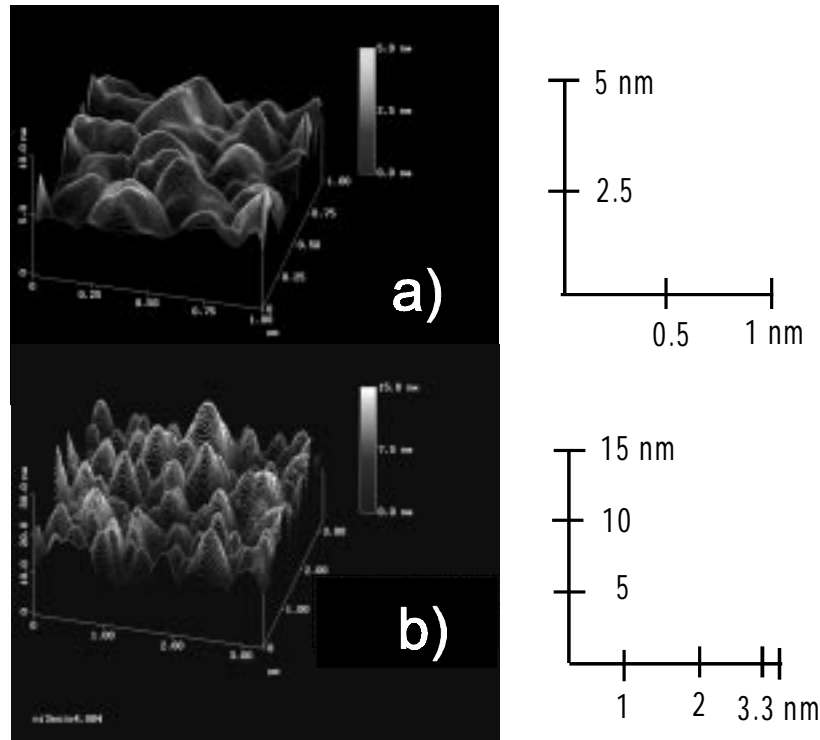


Figure 4.8: Atomic force micrographs of Ni<sub>3</sub>N films a) before and b) after 100 keV Xe irradiation at 80 K. The size of the depicted area is in a)  $1 \times 1 \mu\text{m}$  and in b)  $3.3 \times 3.3 \mu\text{m}$ .

The surface roughening is further illustrated in Figure 4.9, which shows a plot of the rms (root mean square: standard deviation of the height) surface roughness,  $\Delta\sigma_S(\Phi) = \sigma_S(\Phi) - \sigma_S(0)$ , determined also independently via RBS, as a function of the irradiation fluence  $\Phi$ .  $\sigma_S(\Phi)$  denotes to the roughness at the ion fluence  $\Phi$  and  $\sigma_S(0)$  is the surface roughness of the as-prepared sample. The surface roughness linearly scales with the fluence. The results of both AFM and RBS agree well with each other. In conclusion, the low energy irradiation experiments revealed that Ni<sub>3</sub>N phase is a weakly bound system, which dissociates under ion bombardment. Nitrogen is preferentially lost leading to compositional changes in the near-surface region. In spite of the preferential sputtering the Ni<sub>3</sub>N phase structure remains unaltered even at relatively high fluences. The influence of the ion bombardment on the surface topography was corroborated by means of AFM.

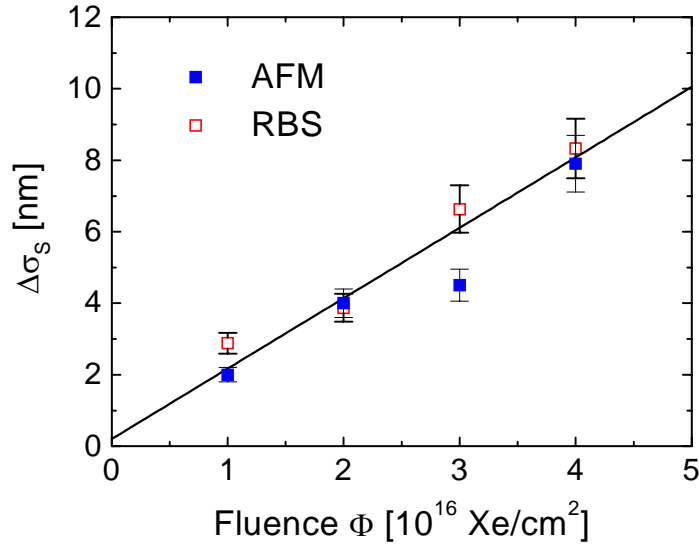


Figure 4.9: Increased surface roughness measured by RBS and AFM as a function of the irradiated fluence.

## 4.4 Ion-beam mixing and phase formation

In the next step Ni<sub>3</sub>N/Si bilayers were irradiated with 450 and 700 keV Xe ions both at 80 K and at room temperature. The goal was to study the atomic transport processes and the possible phase formation at the interface. Varying the incident ion energy gives a possibility to observe the effect of the changing deposited energy density on mixing. The effect of the elevated irradiation temperature may increase the amount of intermixed atoms, either due to radiation enhanced diffusion or higher reaction rates.

### 4.4.1 450 keV irradiations at 80 K

Figure 4.10 presents the RBS spectra of the as-prepared sample and some samples irradiated with 450 keV Xe ions at 80 K. Keeping the sputtering effect in mind, the film thickness of the top nitride layer, 80 nm, was chosen in such way that most 450 keV Xe ions would cross the interface. The projected range of 450 keV Xe in Ni<sub>3</sub>N is about 75 nm. From the figure one sees how the broadening of the interface region develops with the increasing irradiation fluence. Especially at low fluence the interface has an error-function like shape. At higher fluences,  $\geq 2 \times 10^{16}$  Xe-ions/cm<sup>2</sup>, one notes a shoulder at the front edge of the Si signal and the back edge of the Ni signal. Also visible in the RBS spectra is the reduction of the Ni<sub>3</sub>N film thickness due to sputtering. The sputtering yield is expected to be approximately the same as at 100 keV. Maybe slightly smaller as a result of the fact that the sputtering efficiency decreases with the increasing ion energy. The higher backscattering yield in the surface part of the film is again due to the dissociation of the nitride and the out-diffusion of nitrogen. All these features were observed in the low energy irradiations, too.

The Xe profile moves towards the surface with the growing ion fluence, which indicates the outgassing of Xe. Unfortunately the RBS signals of Ni and Xe are partly overlapping due to the low analyzing energy (900 keV). Therefore the detailed investigation of the Xe peak was not possible.

Some samples were sent to the accelerator laboratory of the University of Helsinki to be measured by RBS using 2 MeV  $\alpha$ -particles. The results were compared with the ones obtained by IONAS in order to confirm that the RUMP simulations were done in a correct way.

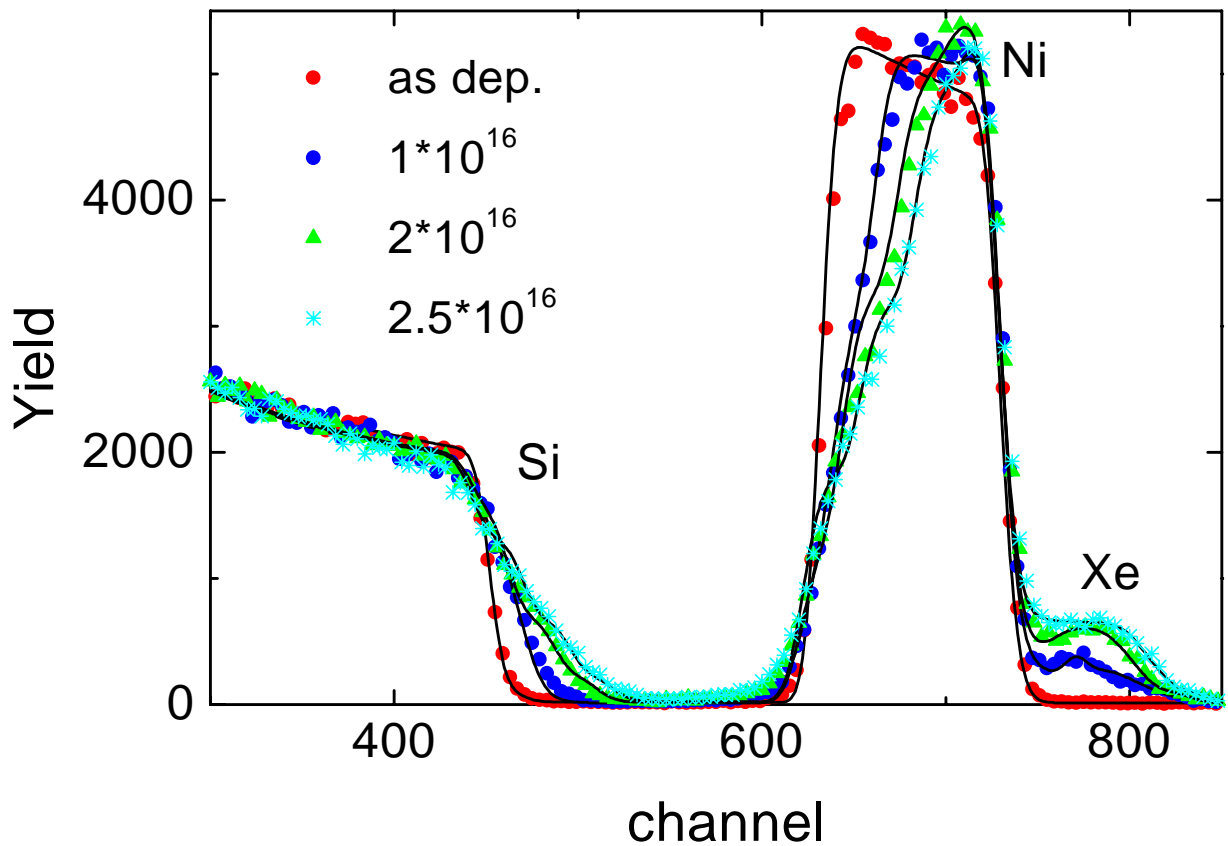


Figure 4.10: RBS spectra of the 450 keV irradiations at 80 K.

The RBS spectra already gave us some information about the irradiation effects. The more exact picture can be achieved by observing the elemental profiles obtained from RBS and RNRA. First the nitrogen profile of the irradiated films determined by RNRA is shown in Figure 4.11. The nitrogen is lost throughout the whole  $\text{Ni}_3\text{N}$  layer but at the surface region the loss is slightly higher than at the interface. Bolse [12] found out the same outcome in irradiations done on  $\text{Ni}_3\text{N}/\text{Al}$  bilayers. The nitrogen content was reduced at the surface region while at the interface it was slightly enhanced and stabilized by the ion beam mixing. AFM measurements revealed that the films consist of large grains (diameter  $\sim 225$  nm). Through the grain boundaries the out-diffusion of nitrogen is possible even at the low temperature of 80 K. Since the nitrogen was lost their profiles were not used in determining the mixing rate. However it was noted that the nitrogen profile broadened along with the interface region with the increasing irradiation fluence similarly as deduced from RBS. There was no noticeable diffusion of  $\text{N}_2$  into the silicon substrate. Here we must point out that the exact elemental composition in the interface region was not known. When calculating the nitrogen concentration the films were approximated to be composed of  $\text{Ni}_3\text{N}$ , which causes an error of some at. % on the nitrogen content at the interface.

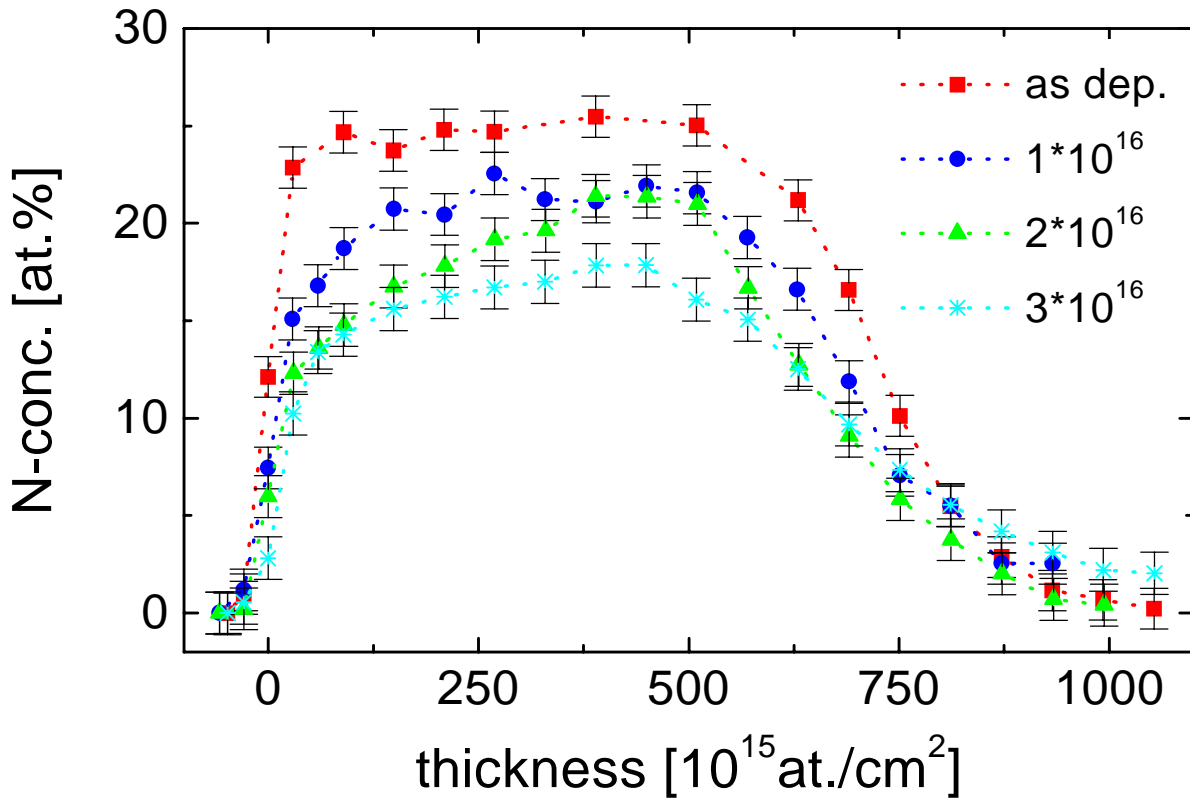


Figure 4.11: RNRA nitrogen profiles of the Xe ion irradiated Ni<sub>3</sub>N/Si bilayers with the ion energy of 450 keV at 80 K.

In the RUMP program, used for analyzing RBS spectra, the simulated xenon profiles were subtracted from the nickel ones, which were then used for determining the interface broadening. Such „cleaned“ elemental fractions of Ni and Si are plotted in Figure 4.12.

For describing the mixing effects we use the so called interface broadening variance  $\Delta\sigma_{\text{Int}}^2(\Phi) = \Delta\sigma_{\text{RBS}}^2(\Phi) - \Delta\sigma_{\text{S}}^2(\Phi)$ , which corrects the variance of the element profiles determined from RBS,  $\Delta\sigma_{\text{RBS}}^2(\Phi)$ , with respect to the increase of the surface roughness,  $\Delta\sigma_{\text{S}}^2(\Phi)$ . For this were used the values obtained at 100 keV beam energy (Figure 4.9). This may not be fully correct, but a rather good approximation because the surface structure (grain size) and sputtering yield change little. As shown in Figure 4.12, both the Ni and Si profiles provide values of  $\Delta\sigma_{\text{Int}}^2(\Phi)$ , which are plotted in Figure 4.13 versus the ion fluence  $\Phi$ . There is only a very weak increase of  $\Delta\sigma_{\text{Int}}^2(\Phi)$  notable up to  $\Phi = 0.5 \times 10^{16}$  Xe-ions/cm<sup>2</sup>, followed by a nearly linear increase at higher fluences. This fluence dependence of  $\Delta\sigma_{\text{Int}}^2(\Phi)$  through the whole fluence range has been approximated by a second-order polynomial in  $\Phi$ . From both the Ni and Si profiles we derived a consistent interface broadening rate/mixing rate of  $\Delta\sigma_{\text{Int}}^2(\Phi) / \Phi = (1.53 + 0.47 \times \Phi) \times 10^4$  atoms/nm<sup>2</sup>. Usually as mixing rate is given only the part depending linearly on the fluence. Assuming that the atomic density (N) varies according to the fractions of Ni<sub>3</sub>N and Si in the interface zone and after normalizing the mixing rate using average density  $N = 73.65$  /nm<sup>3</sup>, the obtained value becomes  $\Delta\sigma_{\text{Int}}^2(\Phi) / \Phi = 2.83$  (49) nm<sup>4</sup>.

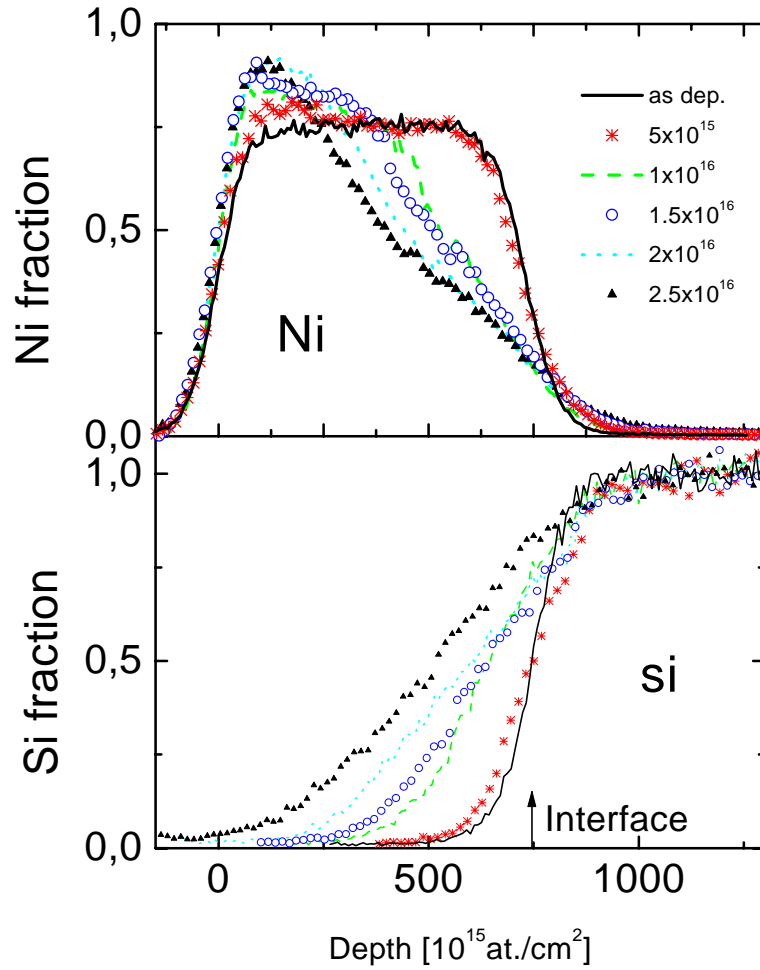


Figure 4.12: Elemental profiles from the 450 keV irradiations at 80 K.

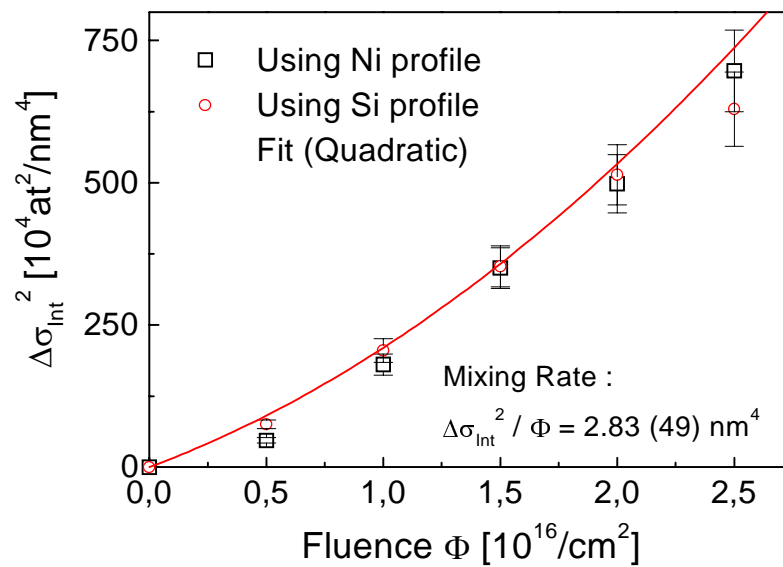


Figure 4.13: Interface broadening variance  $\Delta\sigma_{int}^2$  in  $Ni_3N/Si$  bilayers, due to 450 keV Xe ion irradiation at 80 K, as a function of the ion fluence.

Since RBS is only sensitive to the areal atomic density and therefore does not reveal whether atomic mixing or phase formation has been induced by the ion irradiation, also XRD analyses were performed. The results are illustrated in Figure 4.14. At the lowest fluence of  $0.5 \times 10^{16}$  ions/cm<sup>2</sup> there were hardly any visible changes in the XRD pattern. After the fluence of  $1 \times 10^{16}$  ions/cm<sup>2</sup> XRD measurements clearly revealed the formation and growth of the Ni<sub>2</sub>Si phase in the mixed region up to a dose of  $2.5 \times 10^{16}$  ions/cm<sup>2</sup> and then the formation of Si<sub>3</sub>N<sub>4</sub> at higher fluences. The most probable chemical reaction between Ni<sub>3</sub>N and Si is the formation of Ni<sub>2</sub>Si following the dissociation of Ni<sub>3</sub>N.

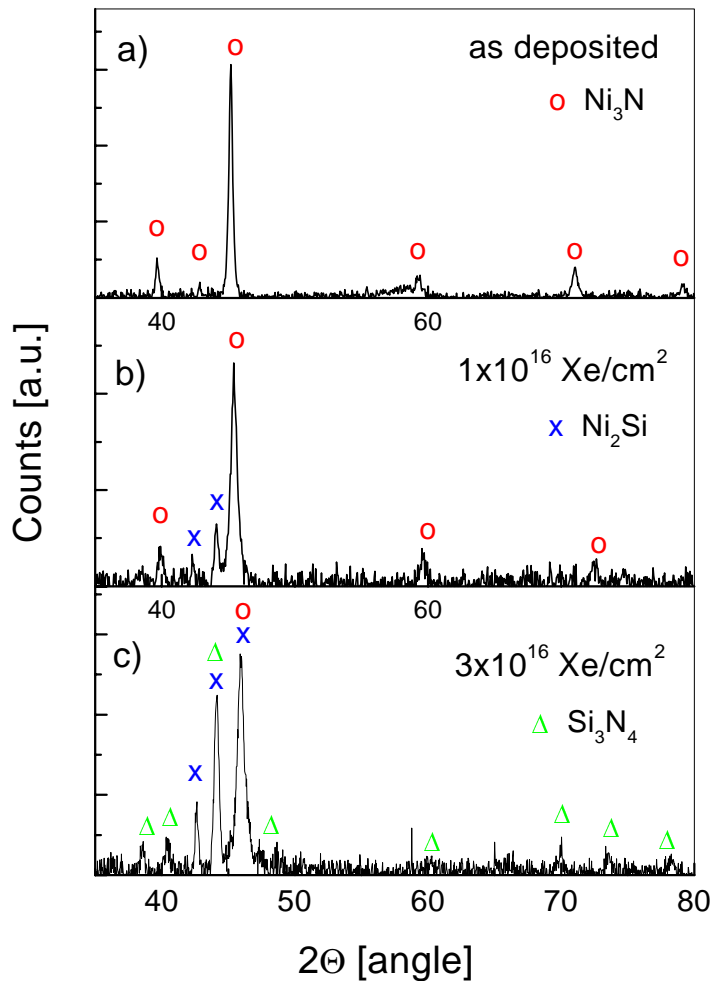


Figure 4.14: XRD spectra of Ni<sub>3</sub>N/Si bilayer samples taken before and after 450 keV Xe<sup>+</sup> ion irradiation at 80 K: a) as deposited, b)  $\Phi = 1 \times 10^{16}$  Xe/cm<sup>2</sup>, and c)  $\Phi = 3 \times 10^{16}$  Xe/cm<sup>2</sup>.

#### 4.4.2 700 keV irradiations at 80 K; the effect of irradiation energy

The Ni<sub>3</sub>N/Si bilayer irradiations were repeated with 700 keV Xe ions. The aim was to observe the effect of the higher ion energy, which corresponds to a slightly different deposited energy at the interface region. The fluences were chosen similar to 450 keV irradiations, starting from  $0.5 \times 10^{16}$  Xe/cm<sup>2</sup> and increasing in steps of  $0.5 \times 10^{16}$  Xe/cm<sup>2</sup>. Some typical spectra for Ni<sub>3</sub>N coated Si obtained by RBS are shown in Figure 4.15. The spectra exhibit the same effects as found under ion bombardment at 450 keV. However, there are some differences. The front part of Ni<sub>3</sub>N film seems to experience a slightly lower increase in Ni yield than in 450 keV case. The low energy ion beam causes more damage at the surface than 700 keV Xe ions that have a projected range of  $\sim 145$  nm in Ni<sub>3</sub>N. The Xe profile is more spread due to straggling and lies deeper in the sample.

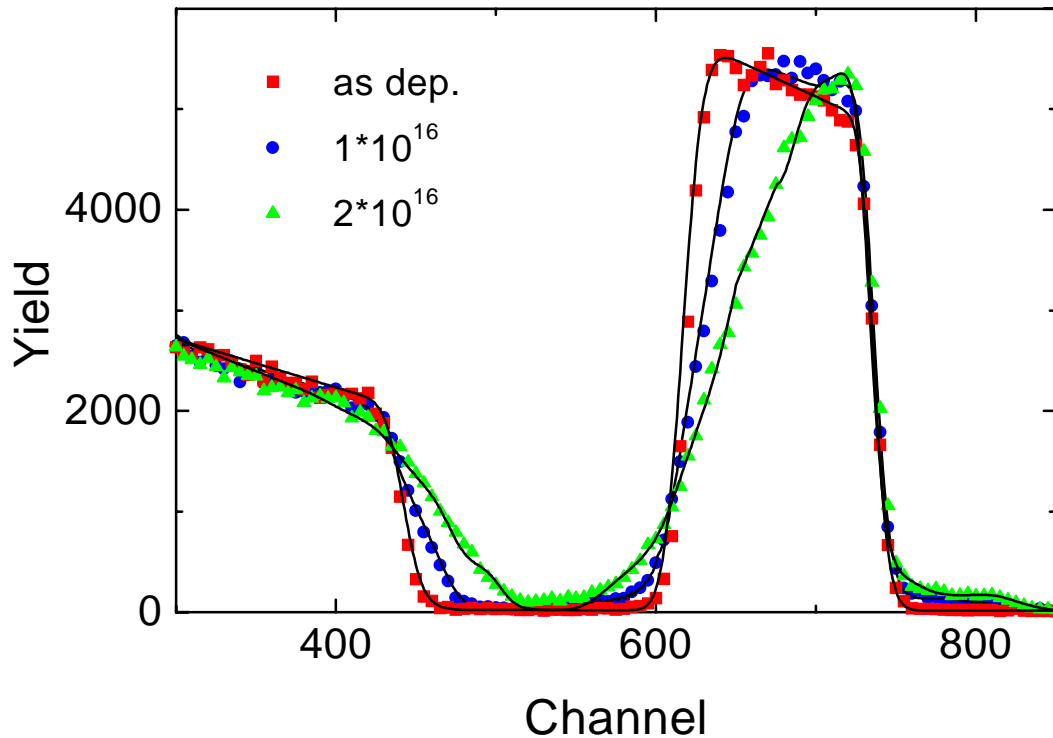


Figure 4.15: RBS spectra of the 700 keV Xe irradiations at 80 K.

The broadening of the interface can clearly be seen from the composition profiles transformed from the RBS spectra. If the profiles again are compared with those of 450 keV irradiations, the difference between the Ni contents at the surface becomes more obvious. 700 keV Xe irradiation produces less changes in the composition of the surface part of the film than 450 keV one. Surprisingly, the loss of the target material at the lowest fluence of  $0.5 \times 10^{16}$  Xe/cm<sup>2</sup> is much more effective. However, this might be an effect of the deposition process. The original thickness of the nitride film was found to vary by some nanometers (max. 5 nm) depending on the position of the silicon substrate on the target holder.

Before calculating the mixing rate from the interface broadening, we can check what has happened to the nitrogen profile under 700 keV Xe irradiation. The RNRA profiles in Figure 4.16 show that again the nitrogen content has decreased in the whole layer. There are no changes between the two irradiation energies at the fluence of  $1 \times 10^{16}$  Xe/cm<sup>2</sup> but at higher fluence the loss of nitrogen is more profound at 700 keV. Also the concentration profile has a different shape. The maximum of the profile shifts towards the surface, away from the interface region. The nitrogen content spreads with the broadening interface.

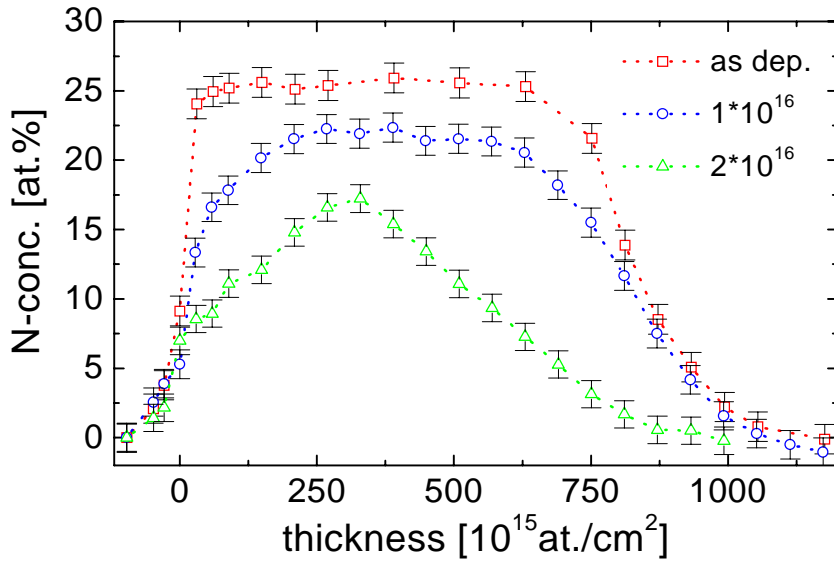


Figure 4.16: RNRA nitrogen profiles of 700 keV Xe irradiation at 80 K.

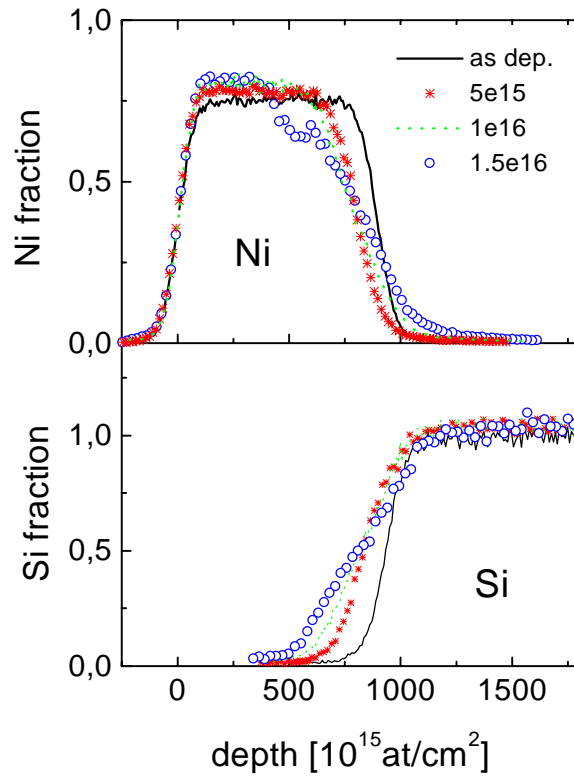


Figure 4.17: Elemental profiles of the 700 keV irradiations.

The values of the interface variance  $\Delta\sigma_{\text{int}}^2$  from the Si and Ni profiles (Figure 4.17) are plotted in Figure 4.18 as a function of the ion fluence. Again the fluence dependence of the  $\Delta\sigma_{\text{int}}^2$  was fitted by a second-order polynomial. The linear part of the fit gave the mixing rate of  $\Delta\sigma_{\text{int}}^2 / \Phi = 0.19(5) \text{ nm}^4$

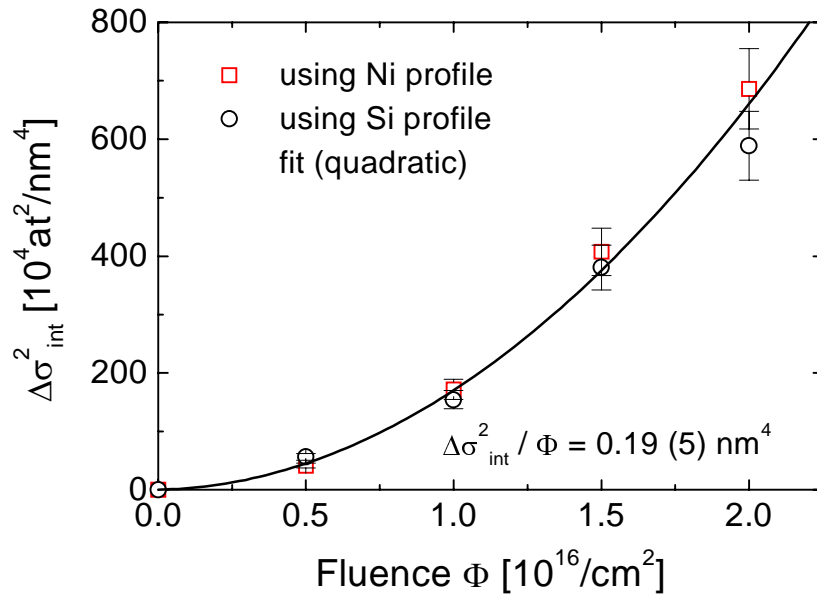


Figure 4.18: The mixing rate of the Ni<sub>3</sub>N/Si bilayers under 700 keV Xe ion irradiation vs. the ion fluence.

The value is almost 20 times smaller than the mixing rate obtained at 450 keV. Obviously the increased incident ion energy has an effect on the mixing rate. The differences will be discussed in more detail in chapter 4.5. The possible phase formation by the 700 keV Xe ions was monitored by XRD and the results are presented in Figure 4.19. At  $1 \times 10^{16}$  Xe/cm $^2$  the formation of Ni<sub>2</sub>Si is more pronounced than in the 450 keV irradiation and also the Si<sub>3</sub>N<sub>4</sub> phase starts growing at this fluence which was not observed at 450 ke. The broad silicon peak, due to sputtering and the measurement geometry, is dominant in spectra. It unfortunately overlaps with some of peaks of Ni<sub>2</sub>Si and Si<sub>3</sub>N<sub>4</sub> phases.

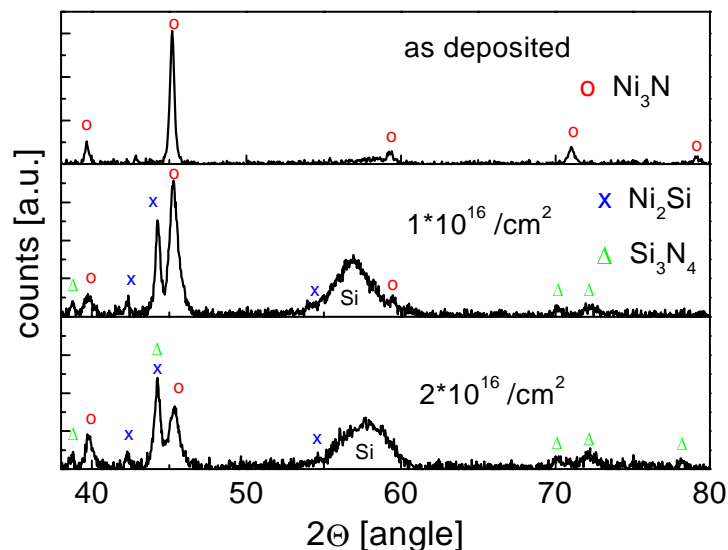


Figure 4.19: XRD patterns of Ni<sub>3</sub>N/Si bilayers irradiated with 700 keV Xe<sup>+</sup> ions at 80 K.

#### 4.4.3 450 keV irradiations at room temperature; the effect of irradiation temperature

One interest in ion beam irradiation is the effect of the sample temperature on the atomic transport processes. The 450 keV Xe irradiations were repeated at room temperature to check this. The Ni<sub>3</sub>N/Si system should not be dominated by RED during room temperature irradiation, since the critical temperature was calculated to be  $\sim 440$  K (or alternatively 344 K, estimated by pure nickel metal) and the cohesive energy  $\Delta H_{\text{coh}} = 4.595$  eV/atom. The RBS spectra of these irradiations are very similar to the ones done at 80 K (see Figure 4.10). Also the Ni- and Si-elemental profiles plotted in Figure 4.21 have similar shapes. But the mixing rate deduced from the profiles,  $\Delta\sigma_{\text{int}}^2 / \Phi = 0.58(15) \text{ nm}^4$ , is closer to the 700 keV case than the 450 keV irradiations at 80 K. The interface broadening as a function of the irradiation fluence is presented in Figure 4.22.

The shape of the nitrogen concentration profiles (Figure 4.23) is essentially the same as at 80 K, but the loss of nitrogen at low fluences is more pronounced at room temperature. At higher fluences the shape and the nitrogen content are almost being independent of the target temperature.

At the fluence of  $1 \times 10^{16} \text{ Xe/cm}^2$  the XRD spectra shown in Figure 4.24 exhibit peaks of Ni<sub>2</sub>Si and Si<sub>3</sub>N<sub>4</sub> phases, which were observed at 700 keV irradiation as well. During the 80 K irradiation at 450 keV, the formation of Si<sub>3</sub>N<sub>4</sub> took place at a higher fluence of  $3 \times 10^{16} \text{ Xe/cm}^2$ .

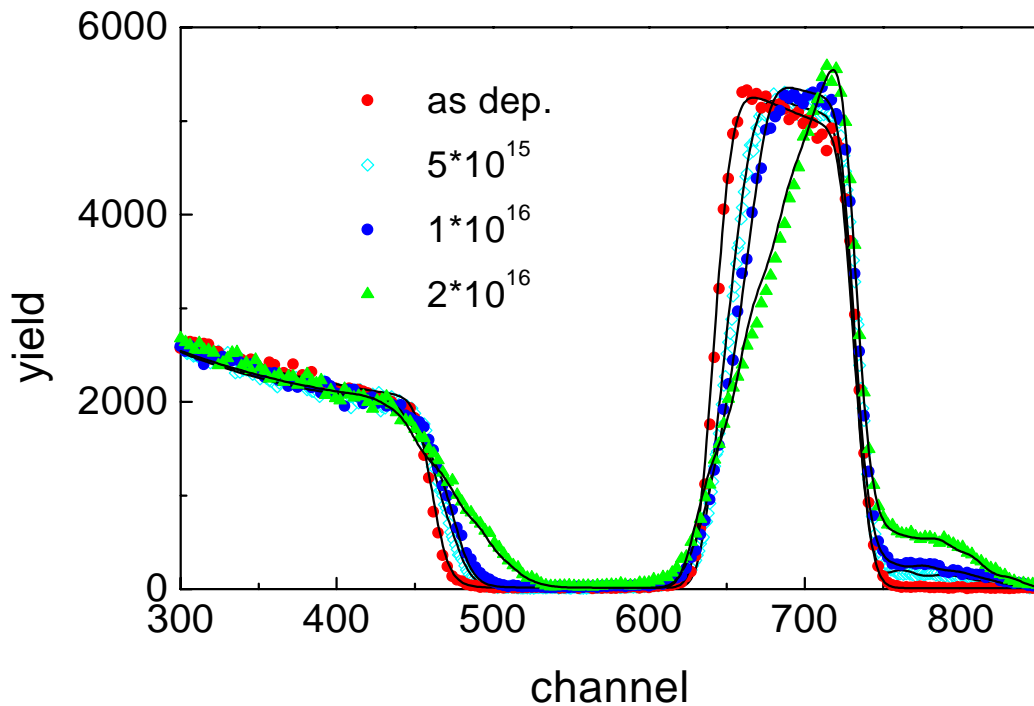


Figure 4.20: Backscattering spectra of samples irradiated with 450 keV Xe at room temperature.

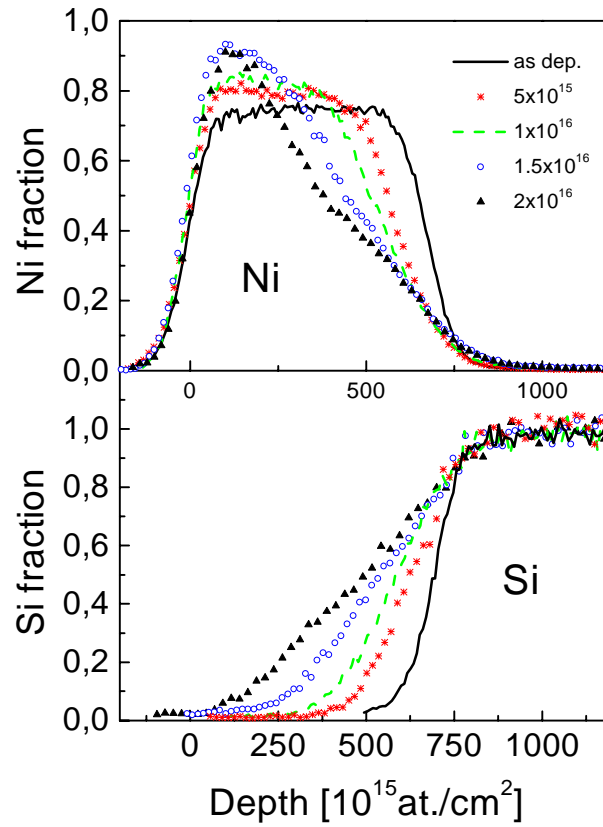


Figure 4.21: Ni- and Si-profiles derived from RBS of 450 keV irradiations at room temperature.

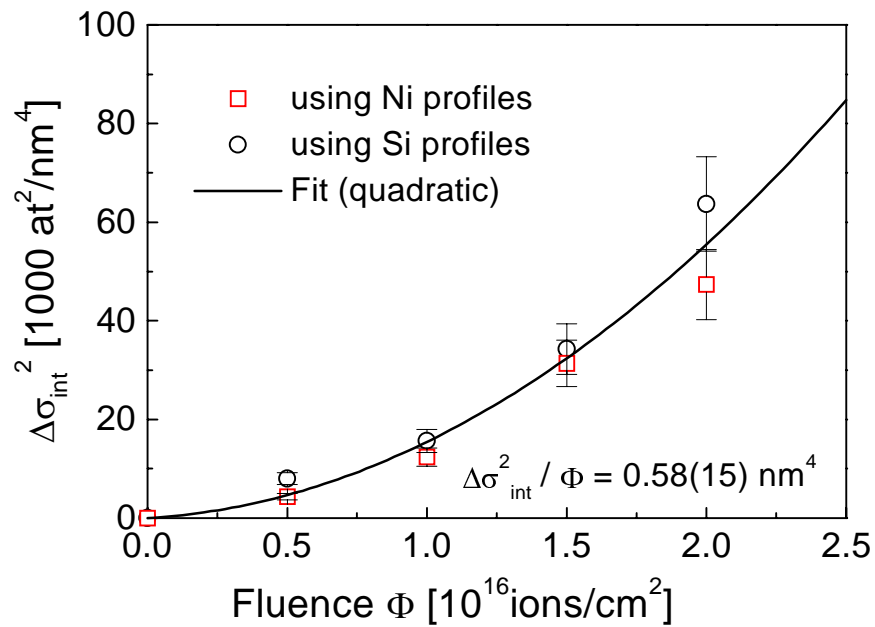


Figure 4.22: Broadening of the interface as function of the fluence for 450 keV irradiations at room temperature

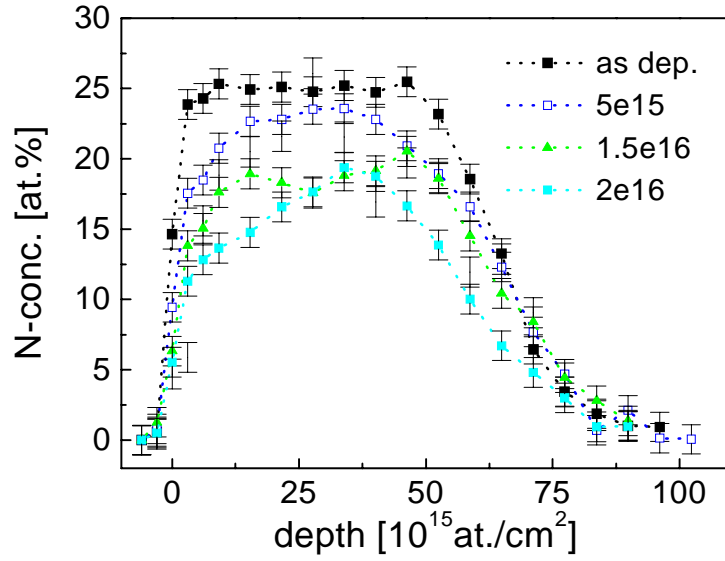


Figure 4.23: RNRA profiles of 450 keV irradiations at room temperature.

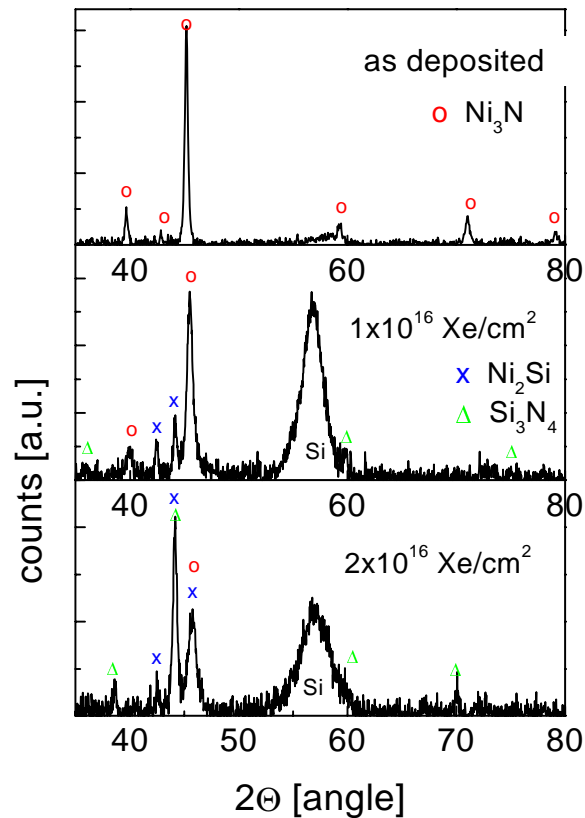


Figure 4.24: XRD patterns before and after 450 keV Xe irradiations at room temperature.

## 4.5 Discussion and interpretations

The interface broadening rates  $\Delta\sigma_{\text{int}}^2$  obtained from the three different irradiations of Ni<sub>3</sub>N/Si bilayers have all a linear and quadratic dependence on the irradiation fluence  $\Phi$ . This leads to a

mixing/reaction rate  $\Delta\sigma_{\text{int}}^2/\Phi$  rising linearly with  $\Phi$  in addition to a constant value. In comparison, the Ni/Si bilayer system only showed a linear dependence of  $\Delta\sigma_{\text{int}}^2$  with  $\Phi$  under 4 MeV Au beam irradiation [49]. The same trend was observed for lower deposited energy density values and over a wide range of target temperatures [56]. As discussed in chapter 4.2.2 Desimoni et al. developed a model for these dependencies. The linear term corresponds to a reaction controlled and the quadratic to a diffusion-controlled mixing process. But the relations to the fluence cannot be unambiguously correlated with the underlying transport mechanism. For example ballistic mixing, local spike mixing and - within certain limits - ion-induced reactions produce a linear relation. Table 4 summarizes the experimental results obtained from the mixing experiments of Ni<sub>3</sub>N/Si bilayers and gives also theoretical values using the pure and modified ballistic model taking into account the compound formation. The calculations are commented later in this chapter.

Table 4. Experimental and calculated mixing rates  $k$  and formed phases at different ion energies and irradiation temperatures.

<b>Xe ion energy</b> [keV]	<b>T<sub>irr</sub></b> [K]	<b>k<sub>exp</sub></b> [nm <sup>4</sup> ]	<b>k<sub>ball</sub> (pure ballistic)</b> [nm <sup>4</sup> ]	<b>k<sub>comp</sub> (compound)</b> [nm <sup>4</sup> ]	<b>Phase formation</b>
450	80	2.83 + 0.86 $\Phi$	0.096 - 0.26	1.3 – 3.6	Ni <sub>2</sub> Si, Si <sub>3</sub> N <sub>4</sub>
700	80	0.19 + 3.10 $\Phi$	0.15	4.1	Ni <sub>2</sub> Si, Si <sub>3</sub> N <sub>4</sub>
450	300	0.58 + 2.27 $\Phi$	0.096 - 0.26	1.3 – 3.6	Ni <sub>2</sub> Si, Si <sub>3</sub> N <sub>4</sub>

In Figure 4.25 the quantity  $\Delta\sigma_{\text{int}}^2$  is plotted as a function of the fluence for all irradiations. The differences between the mixing rates do not seem so dramatic at low fluences. For  $\Phi > 1.5 \times 10^{16}$  Xe/cm<sup>2</sup>, the experimental values start to separate from each other. Obviously both the ion energy and the target temperature have an effect on the amount of mixing. In Figure 4.26 the mixing rates  $\Delta\sigma_{\text{int}}^2/\Phi$  are represented in a way that the linear and the quadratic terms are clearly visible and better illustrate the similarities and differences between these irradiations. From the figure the similarity between the 700 keV irradiation at 80 K and the 450 keV at room temperature is striking. The elevated target temperature, RED, seems to have the same influence on the mixing process as the increasing ion energy. Actually the higher target temperature was not expected to effect the mixing since the calculated critical temperature was well above room temperature, 440 K. The connection between the critical temperature and the cohesive energy proposed by Cheng, equation(4.13), is based on ion-beam mixing experiments mostly done on metal/metal bilayers. Perhaps it does not give the correct approximation for a nitride/semiconductor system, especially for the exceptionally behaving Ni<sub>3</sub>N. The estimated critical temperature calculated using equation (4.9) and the formation energy for vacancies in nickel probably results in a more realistic value of a lower critical temperature (e.g. 344 K for Ni).

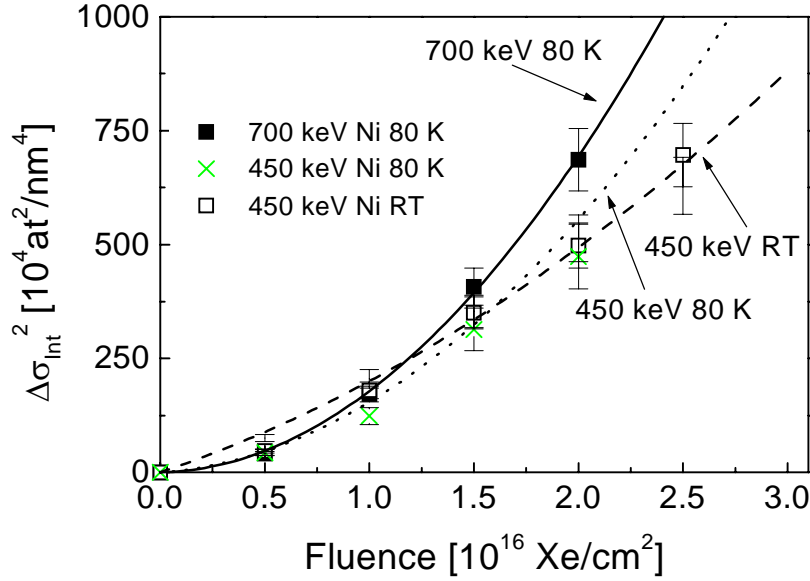


Figure 4.25: Mixing rates of all irradiations as function of the fluence.

The differences between the irradiations done at the same temperature, 80 K, but with different ion energy can partly be explained by the change in the energy density  $F_D$  deposited by elastic collisions in the interface. Figure 4.27 shows the deposition energy curves calculated by TRIM for 450 and 700 keV Xe ions in Ni<sub>3</sub>N. The dotted vertical line represents the interface between Ni<sub>3</sub>N and the silicon substrate. With the increasing irradiation fluence the top layer thickness decreases due to sputtering (Figure 4.7). In 450 keV irradiation the deposited energy, starting from the value of  $\sim 1.5$  keV/nm/ion, increases with the sputtered thickness and reaches its maximum, 4 keV/nm/ion, at the film thickness of about 50 nm. Even small changes of the nitride layer thickness lead to large uncertainties in  $F_D$ . In 700 keV irradiation the loss of the nitride layer has only little effect on the value of the deposited energy. The deviation of the experimental points from the fitted line is weaker at 700 keV than at 450 keV (independent of temperature) which is also an effect of the varying deposited energy density.

Bolse contradicted the purely ballistic nature of mixing in Ni<sub>3</sub>N and in spite of the low  $Z$  value of the nitride ( $Z_{ave}=18.4$ ), did not rule out the possibility of thermal spikes and the mixing biased by chemical potential gradient at the interface. In this work the thermal spikes are not believed to take place during ion bombardment. Rather modifications of the ballistic model, considering the thermochemical properties of the system to form compounds, should allow one to explain the experimental results. The ballistic model by Sigmund and Gras-Marti (4.4) gives the following mixing rates for 450 and 700 keV irradiations

$$\Delta\sigma_{int}^2 / \phi (450 \text{ keV})_{ball} = (0.10 - 0.26) \text{ nm}^4 \quad \text{and} \quad \Delta\sigma_{int}^2 / \phi (700 \text{ keV})_{ball} = 0.15 \text{ nm}^4$$

The kinematic factor  $\xi$  is 0.966. The deposited energy for 700 keV is 2.3 KeV/nm/ion, the separation distance of a Frenkel-pair is assumed  $R_d = 1$  nm, the separation energy 30 eV/at and the average atomic density is 73.65 at/nm<sup>3</sup>. At the lowest fluence,  $0.5 \times 10^{16}$  Xe/cm<sup>2</sup>, the deposited energy in 450 keV irradiation has approximately the value of 1.5 keV/nm/ion, corresponding to mixing rate of  $0.10 \text{ nm}^4$ , while the maximum value 4 keV/nm/ion gives the rate of  $0.26 \text{ nm}^4$ .

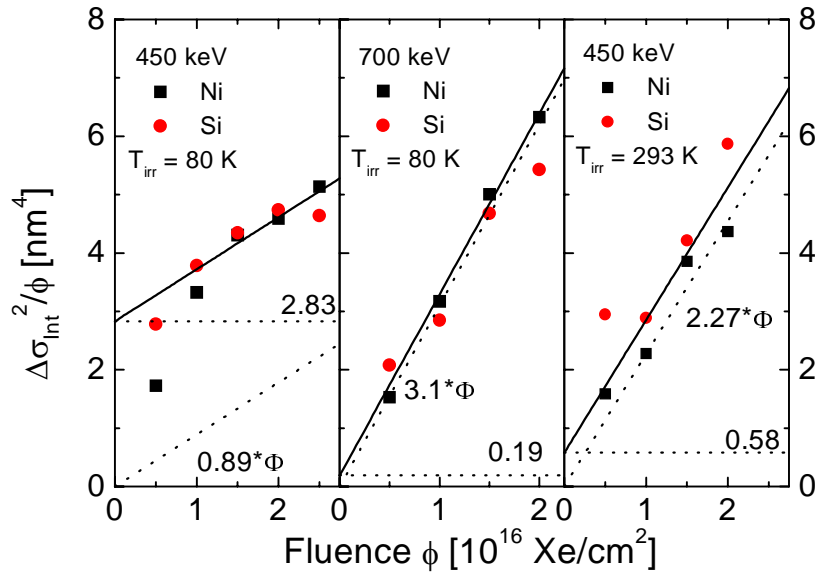


Figure 4.26: The mixing rate of the three different irradiations as function of fluence. Dotted lines are the separate linear and quadratic terms of the second polynomial fit and the solid line is a sum of the both terms.

When these values are compared with the experimental mixing rates (see Table 3), the linear part of the quadratic fit of 700 keV irradiation is very close to the calculated value. However, the XRD measurements prove compound formation of  $\text{Ni}_2\text{Si}$  and  $\text{Si}_3\text{N}_4$  phases. At both energies, 450 and 700 keV, and at the both temperatures, 80 and 300 K.

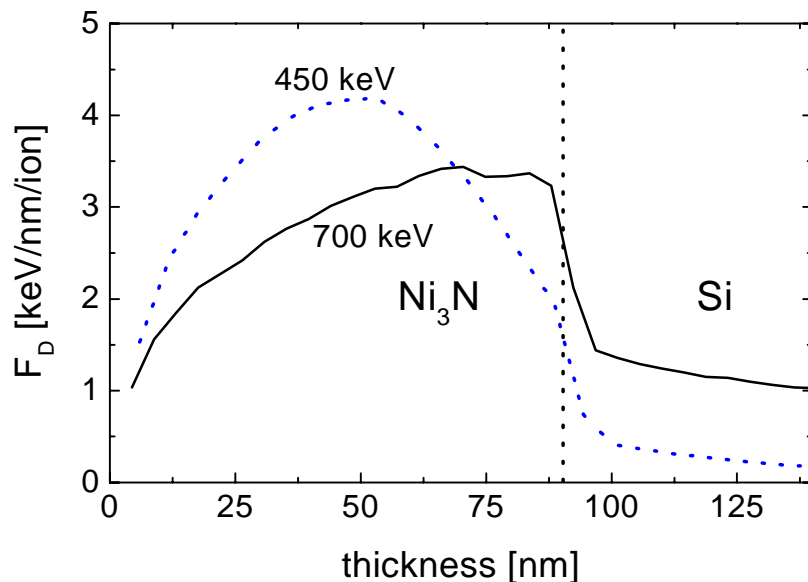
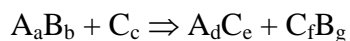
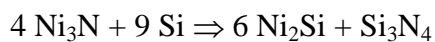


Figure 4.27: Deposited energy of 450 (dotted curve) and 700 keV (solid curve) Xe ions in  $\text{Ni}_3\text{N}/\text{Si}$  calculated by TRIM.

According to the chemical reaction of



The ballistic mixing rate formula can be modified as in equation (4.8)

$$K = K_{ball} \cdot 2 \left[ \frac{(a/(a+b))N_{A_d B_b}}{(d/(d+e))N_{A_d C_e}} + \frac{(b/(a+b))N_{A_d B_b}}{(g/(g+f))N_{C_f B_g}} + \frac{N_c}{(e/(d+e))N_{A_d C_e}} + \frac{N_c}{(f/(g+f))N_{C_f B_g}} \right] \quad (4.14)$$

The formula (4.14) derives mixing rates one order of magnitude larger than the pure ballistic calculation

$$\Delta\sigma_{int}^2 / \phi (450 \text{ keV})_{comp} = 1.3 - 3.6 \text{ nm}^4 \quad \text{and} \quad \Delta\sigma_{int}^2 / \phi (700 \text{ keV})_{comp} = 4.1 \text{ nm}^4$$

These values are close to the experimental reaction-controlled mixing rates.

The comparison of the experimental mixing rates of all the irradiations, the properties of the bilayer and the theoretical explanations and calculations results in the following conclusion. Since Ni<sub>3</sub>N/Si has a low average charge number, 18.4, the possibility of the thermal spike initiation during ion bombardment can be ruled out. Therefore, the part of the mixing rate having the linear dependence with the irradiation fluence does not originate from the diffusion controlled process (dominates during thermal spike stage) but is due to purely ballistic-type mixing. The quadratic term is a result of the reaction controlled mixing, i.e. the compound formation is enhanced by the chemical driving forces present at the interface during ballistic cascade mixing. Both the increasing Xe-ion energy and the elevated sample temperature increased the reaction controlled mixing rate.

## 4.6 Summary

In this study the influence of the incident ion energy and the target temperature on the ion beam mixing of Ni<sub>3</sub>N/Si bilayers as well as the behavior of Ni<sub>3</sub>N under ion bombardment was investigated. The irradiation of low-energy, 100 keV, ions at 80 K shows the dissociation of Ni<sub>3</sub>N and the preferential loss of nitrogen at the near-surface region. Both the increased surface roughness and sputtered layer thickness depend linearly on the irradiation fluence. Also the grain size changed with the fluence. The ion bombardment induced surface changes were comprehensively analyzed only for 100 keV irradiation and using Xe ions. Especially, the AFM analysis at higher ion energies would give some useful information. Similar investigation of the structural and topographical changes, e.g. texture, grain size, etc., using other ion species and extending the study also to other nitrides is an interesting subject for further work.

The results of interface mixing using 450 and 700 keV Xe<sup>+</sup> ions show a very high interface-broadening rate, which cannot be explained by the ballistic model. The detection of nickel silicide and silicon nitride phases in the mixed region indicated the presence of chemical driving forces in this system. Consequently, the mixing is dominated by compound formation. Both the higher irradiation energy and the elevated target temperature enhance the reaction-controlled part in the mixing process.

The results accomplished in this study have given a deeper survey into the complex Ni<sub>3</sub>N/Si system. So far, most of the ion beam mixing experiments were performed on binary alloys. Expanding the investigations to ternary systems somewhat complicates the interpretations of the results and puts the existing models to a test. The simultaneous reaction and diffusion controlled processes at the

interface were not observed in other systems before. The theory behind atomic transport process influenced by the thermochemical potential at the interface in a ballistic system, the compound formation model, works quite well for the present system. Ni<sub>3</sub>N/Si proved to be an excellent bilayer combination in observing the influence of the chemical properties in a ballistic cascade mixing process. A comprehensive irradiation study on other nitride/semiconductor or ceramic/semiconductor systems would improve the understanding of the transport mechanisms.

## 5 References

- [1] M. Kawamura, Y. Abe, H. Yanagisawa und K. Sasaki, *Thin solid films* 287 (1996) 115.
- [2] T. Maruyama und T. Morishita, *Appl. Phys. Lett.* 69 (1996) 890.
- [3] C.C. Cheng, Y.C. Chen, H.J. Wang und W.R. Chen, *J. Vac. Sci. Technol. A* 14(4) (1996) 2238.
- [4] P. Schaaf, C. Illgner, M. Niederdrenk und K.P. Lieb, *Hyp. Int.* 95 (1995) 199.
- [5] A. Anttila, J. Salo und R. Lappalainen, *Materials Letters* 24 (1995) 153.
- [6] M. Kawamura, Y. Abe, H. Yanagisawa und K. Sasaki, *Thin Solid Films* 287 (1996) 115.
- [7] E. Ettliger, U. Nienaber und H. Schimmer, *Berichte aus Technik und Wissenschaft* 78 (1999) 25.
- [8] H. Nakagawa, S. Nasu, H. Fujii, M. Takahashi und F. Kanamaru, *Hyperfine Interactions* 69 (1991) 455.
- [9] M. Niederdrenk, *Diplomarbeit (Universität Göttingen, 1994)*.
- [10] L. Rissanen, K.P. Lieb, M. Niederdrenk, O. Schulte und P. Schaaf, I. Ortalli (Ed.), *Conf. Proc. ICAME 95* 50 (1996) 595.
- [11] L. Rissanen, M. Neubauer, K.P. Lieb und P. Schaaf, *J. Alloys and Compounds* 274 (1998) 74.
- [12] W. Bolse, *Mater. Sci. Eng. R12* (1994) 53.
- [13] Y.T. Cheng, *Mat. Sci. Rep.* 5 (1990) 45.
- [14] M. Nastasi, J.W. Mayer and J.K. Hirvonen, *Ion-solid interactions: fundamentals and applications* (Cambridge university press, JAHK).
- [15] M. Neubauer, *Doktorarbeit, Universität Göttingen ed. (Cuvillier Verlag Göttingen, 1996)*.
- [16] R. Kelly, *Mat. Sci. Eng. A* 115 (1989) 11.
- [17] M. Milosavljevic, T. Cortis, K.P. Lieb und N. Bibic, *Nucl. Instr. Meth. B* 68 (1992) 426.
- [18] M. Uhrmacher, K. Pampus, F.J. Bergmeister, D. Purschke und K.P. Lieb, *Nucl. Instr. Meth. B* 9 (1985) 234.
- [19] J.F. Ziegeler, J.P. Biersack and U. Littmark, *The stopping and range of ions in solids* (Pergamon Press, New York, 1985).
- [20] J. Lindhard und M. Scharff, *Mat. Fys. Medd. Dan. Vid. Selsk.* 27 (1953) 15.
- [21] N. Bohr, *Mat. Fys. Medd. Dan. Vid. Selsk.* 18 (1948) 8.
- [22] L.R. Doolittle, *Nucl. Instr. Meth. B* 9 (1985) 344.
- [23] J.R. Tesmer, M. Nastasi, J.C. Barbour, C.J. Maggiore und J.W. Mayer, *MRS* 1 (1995) 1.
- [24] J. Jokinen, J. Keinonen, P. Tikkanen, A. Kuronen, T. Ahlgren und K. Nordlund, *Nucl. Instr.*

- and Meth. B 119 (1996) 533.
- [25] M. Borowski, Präzisionsmessungen zweier Resonanzen in den Reaktionen ..., Diplomarbeit (Universität Göttingen, 1992).
- [26] G. Vizkelethy, Nucl. Instr. Meth. B 64 (1992) 734.
- [27] F. Landry, P. Schaaf und K.P. Lieb, in preparation BAND (1999) SEITE.
- [28] U. Gonser, Mössbauer spectroscopy In Microscopic Methods in Metals (Springer Verlag, 1986).
- [29] L. May, An introduction to Mössbauer spectroscopy (Plenum Press, New York-London, 1971).
- [30] J.J. Spijkermann, Conversion electron Mössbauer spectroscopy In Mössbauer Effect Methodology Vol. 7, I.J. Gruvermann ed. (Plenum Press, New York-London, 1981).
- [31] U. Gonser, P. Schaaf und F. Aubertin, Hyp. Int. 65 (1991) 95.
- [32] P. Schaaf, T. Wenzel, K. Schemmeling und K.P. Lieb, Hyp. Int. 92 (1994) 1189.
- [33] B.K. Agarwal, X-Ray Spectroscopy, An Introduction, D.L. MacAdam ed. (Springer Verlag, Berlin-Heidelberg-New York, 1979).
- [34] G.J.W. Dorman und M. Sikkens, Thin solid films 105 (1983) 251.
- [35] J. Kunze, Akademie Verlag, (1990)
- [36] H.A. Wriedt, N.A. Gokcen und R.H. Nafziger, Bulletin of alloy phase diagrams 8 (1987) 355.
- [37] A.F. Guillermet und H. Du, Z. Metallkunde 85 (1994) 154.
- [38] T.K. Kim und M. Takahashi, Appl. Phys. Lett. 20 (1972) 492.
- [39] C. Frantz, Scripta Metallurgica 19 (1985) 1503.
- [40] M. Takahashi, H. Fujii, H. Nakagawa, S. Nasu und H. Kanamaru, In: Proc. 6th Int. Conf. of Ferrites (ICF6) BAND (1992) 508.
- [41] K. Suzuki, H. Morita, T. Kaneko, H. Yoshida und H. Fujimori, J. Alloys and Compounds 201 (1993) 232.
- [42] N. Ternao und A. Berghezan, J. Phys. Soc. Jpn. 14 (1959) 139.
- [43] D.W. Hoffman, J. Vac. Sci. Technol. A 12(4) (1994) 953.
- [44] D.K. Inia, W.M. Arnoldbik, A.M. Vredenberg und D.O. Boerma, Surf. Eng. 12 (1996) 326.
- [45] P. Wynblatt and R.C. Ku, 115, W.C. Johnson and J.M. Blakely eds. (Americal Society for Metals, 1979) 115.
- [46] P. Sigmund und A. Gras-Marti, Nucl. Instr. Meth. 182/183 (1981) 25.
- [47] Z.L. Wang, J.F.M. Westendorp und F.W. Saris, Nucl. Instr. Meth. 209/210 (1983) 115.
- [48] P. Borgesen, D.A. Lilienfeld und H.H. Johnson, Appl. Phys. Lett. 57 (1990) 1407.
- [49] J. Desimoni und A. Traverse, Phys. Rev. B 48 (1993) 266.

- 
- [50] J. Desimoni, A. Traverse und M.G. Medici, Nucl. Instr. Meth. B 72 (1992) 197.
- [51] W.Z. Li, H. Kheyrandish, Z. Al-Tamini und W. Grant, Nucl. Instr. Meth. B 19-20 (1987) 723.
- [52] R. de Reus, A.M. Vredevberg, A.C. Voorrips, H.C. Tissink und F.W. Saris, Nucl. Instr. Meth. B 53 (1991) 24.
- [53] F.R. de Boer, R. Boom, W.C.M. Mattens, A.R. Anderson, Miedema and A.K. Niessen, Cohesion in metals, F.R. de Boer and D. Pettifor eds. (North-Holland, Amsterdam, 1988).
- [54] F.R. de Boer, R. Boom, W.C.M. Mattens, A.R. Miedema and A.K. Niessen, Cohesion in metals, F.R. de Boer and D.G. Pettifor eds. (North-Holland, 1988).
- [55] A.Yu. Kuznetsov und B.G. Svensson, Appl. Phys. Lett. 66 (1995) 2229.
- [56] R.Y. Lee, C.N. Whang, H.K. Kim und R.J. Smith, Nucl. Instr. Meth. B 33 (1988) 661.